2013

Applications of Autonomous pH and pCO2 Sensors to Study Inorganic Carbon Dynamics in a Coastal Upwelling System

Katherine Elizabeth Harris

APPLICATIONS OF AUTONOMOUS pH AND pCO_2 SENSORS TO STUDY INORGANIC CARBON DYNAMICS IN A COASTAL UPWELLING SYSTEM

By

KATHERINE ELIZABETH HARRIS

B.S. Chemistry, The College of William and Mary, Williamsburg, Virginia, 2008

Dissertation

presented in partial fulfillment of the requirements
for the degree of

Doctor of Philosophy
in Chemistry

The University of Montana
Missoula, MT

December 2013

Approved by:

Sandy Ross, Dean of The Graduate School
Graduate School

Dr. Michael DeGrandpre
Department of Chemistry and Biochemistry

Dr. Christopher Palmer, Chair
Department of Chemistry and Biochemistry

Dr. Klara Briknarova
Department of Chemistry and Biochemistry

Dr. Burke Hales
College of Earth, Oceanic, and Atmospheric Sciences, Oregon State University

Dr. Garon Smith
Department of Chemistry and Biochemistry

Harris, Katherine, Ph.D., Winter 2013 Chemistry

Applications of autonomous pH and CO_2 sensors to study carbonate system dynamics in a coastal upwelling system

Chair: Dr. Michael DeGrandpre

Submersible Autonomous Moored Instruments for pH and pCO_2 (SAMI-pH and SAMI-CO_2) were deployed in a coastal upwelling zone on the Oregon Coast to collect unique multi-season, multi-year datasets of carbonate system dynamics. This is the first long-term deployment of the SAMI-pH paired with a SAMI-CO_2. The objectives of this study included (1) improving the accuracy of the SAMI-pH (2) assessing the performance of using paired SAMI-pH and SAMI-CO_2 measurements to calculate other carbonate system parameters and (3) analyzing the data to better understand the seasonal, inter-annual, and upwelling variation in the coastal marine carbonate system. SAMI-pH accuracy was improved by better characterization of the pH indicator used in these spectrophotometric measurements. Using paired SAMI-pH and SAMI-CO_2 measurements from this study to calculate calcium carbonate saturation states (Ω) occasionally induced significant offsets in the results and so should be used with caution. However, a salinity-derived alkalinity for the region was found to calculate more accurate Ω when paired with either SAMI-pH or SAMI-CO_2 measurements. This unique, long-term, high temporal resolution dataset (collected over a period of five years) was used to characterize the carbonate system dynamics in this coastal upwelling zone. Large, fast changes in Ω (>3.0) occurred over a period of a few days and aragonite saturation state (Ω_{Ar}) decreased to undersaturation (Ω_{Ar}<1.0) seven times during the periods studied. Intrusion into the region by the Columbia River plume had a dilution effect on Ω_{Ar} during spring and summer, but biological productivity also played a major role in Ω_{Ar} during these seasons. In autumn and winter air-sea gas exchange and biological productivity were the controlling mechanisms. The return of the carbonate system parameters to pre-upwelling values was mainly controlled by mixing (with shelf and riverine freshwater) with some contribution from biological productivity. Since lowered Ω_{Ar} can have a negative impact on many of the region's calcifying organisms (such as oysters, clams, sea urchins, and pteropods), this dataset was used to estimate pre-industrial Ω_{Ar}. Estimates indicate that Oregon shelf surface water Ω_{Ar} has decreased by over 0.50 since the pre-industrial period and will decrease more in the near future.

Acknowledgements

Many people have been of assistance to me throughout my time as a graduate student. Special thanks to:

My research advisor, Dr. Michael DeGrandpre, for all his support and all he has taught me during my time at U of M. When I entered the chemistry graduate program in landlocked Montana, little did I know that I would end up doing marine chemistry research! It's thanks to his first semester research presentation that I ended up where I am.

My graduate committee – Dr. Christopher Palmer, Dr. Klara Briknarova, Dr. Burke Hales, and Dr. Garon Smith, for all the time and effort they put into helping me improve my dissertation. Special thanks to Dr. Burke Hales for hosting me at Oregon State University and giving me the opportunity to take part in research cruises.

All the members of the DeGrandpre group - especially Cory Beatty, Sarah Cullison Gray, Tommy Moore, Brittany Peterson, and Emma Jaqueth - for not only helping me with research and SAMI troubleshooting, but also for the great conversations that made lab fun. Thanks to Colleen Wall at OSU for her help with SAMI deployments and for keeping me sane during my time out in Oregon.

Those at Sunburst Sensors - especially Jim, Reggie, and Jenny - for helping me with all manner of SAMI troubleshooting questions.

My high school chemistry teacher, Elizabeth Parks, for inspiring me and first getting me interested in chemistry. Also, thanks to my other science teachers and to my mentor, Dr. Dawn Wellman, at Pacific Northwest National Lab.

To all my other friends at U of M and to the PWSZ for reminding me that there is life outside of chemistry and that sometimes you need to put down work and enjoy it.

To Andrew, for encouraging me and brightening each day during the long months of dissertation writing (and afterwards too).

And, finally, thanks to all my family. I especially want to thank my parents, Del and Deb, for their love and encouragement, and my sister, Margaret, for her love and for blazing the trail in Harris doctoral achievement.

Table of Contents

List of Tables

List of Figures

Research Summary

A summary of the dissertation content is provided here to guide the reader. This is the first study that uses long-term deployments of the SAMI-pH paired with a SAMI-CO_2 to acquire unique multi-season, multi-year datasets of carbonate system dynamics in a coastal upwelling zone. These data are extremely useful, especially in light of marine carbonate system changes due to ocean acidification, as described below. There were three main objectives to this research: (1) to improve accuracy of the SAMI-pH, (2) to evaluate the performance of paired SAMI-pH and SAMI-CO_2 to calculate carbonate system parameters and (3) to use these instruments to characterize the seasonal and inter-annual variation of the marine carbonate system in a coastal upwelling zone.

Objective 1: The goals of the instrument-based studies focused on improving the accuracy of the SAMI-pH. Previously we had used molar absorptivity temperature dependences for the pH indicator mCP determined by *Seidel* [2006] but changes in instrument design made it necessary to re-evaluate these. In addition, efficacy of switching to the pH indicator thymol blue was tested. New mCP relationships between temperature and molar absorptivities were determined on different SAMI-pH instruments. Variations between SAMI-pHs were found to be comparable to variations in the mCP temperature relationships run during multiple experiments on a bench-top UV-Vis. Thus the averaged mCP temperature relationships for the SAMI-pH were applied to all SAMI-pH calculations. Solubility and impurity issues were found to make switching to thymol blue impractical.

Objective 2: One goal of the field studies was to do field tests of a tris-enabled SAMI-pH to validate the accuracy of the data collected in situ. Further exploration of the effectiveness of using the SAMI-pH and SAMI-CO_2 pair to calculate carbonate system parameters was also conducted, building off the previous work of *Gray* [2010]. Based on these studies, paired SAMI-pH and SAMI-CO_2 were expected to accurately calculate calcium carbonate saturation states (Ω). Using paired SAMI-pH and SAMI-CO_2 data to calculate Ω gives us detailed time-series of Ω dynamics, important measures of marine ecosystem health in the face of ocean acidification. Extensive field testing was completed in the Oregon coastal upwelling zone to determine if results were comparable to those obtained by *Gray et al.* [2011; 2012]. Results from these studies found that there could be considerable offsets in Ω's calculated with different parameters

and so this combination should be used with caution. My studies found that using a salinity-derived alkalinity appropriate for the location (A_{Tsalin}) along with pH or pCO_2 resulted in the most accurate Ω's.

Objective 3: Finally, the SAMI field data was analyzed to better understand the highly dynamic carbonate system in the upwelling zone off the coast of Oregon. The first goal was to characterize the natural short-term seasonal and annual variability of the carbonate system in the Oregon coastal upwelling zone using SAMI-pH and SAMI-CO_2 deployed together on the NH-10 mooring. Further goals involved analyzing these unique observations to determine the seasonal controlling mechanisms for Ω_{Ar} and specifically the processes controlling Ω_{Ar} during selected strong upwelling events. In addition these highly-detailed carbonate system observations were used to estimate changes in the chemical make-up of Oregon coastal upwelling zone waters since the industrial revolution as well as to predict what anthropogenic climate change may have in store for this highly dynamic region.

Ω's had never previously been continuously recorded during upwelling, but we collected a five-year time-series of carbonate system dynamics in the Oregon coastal upwelling zone, with observations during spring, summer, autumn, and winter. Ω_{Ar} decreased rapidly by ~3.0 over a period of a few days and reached undersaturation ($\Omega_{Ar}<1.0$) seven times during the three summers recorded. These events could have potentially detrimental consequences for the calcifying organisms (such as oysters, clams, sea urchins, and pteropods) that live on the shelf. The duration of low Ω_{Ar} conditions during upwelling was controlled by varying mechanisms. These unique multi-season carbonate system observations were also used to estimate that current mean Ω_{Ar} has decreased significantly compared to estimated pre-industrial Ω_{Ar}, with current surface and shelf break Ω_{Ar} means decreased by 0.52 and 0.20, respectively.

CHAPTER 1

Introduction

1.1. Anthropogenic Climate Change

Human-induced climate change has been a topic of study for scientists since the 19th century [*Weart*, 2008]. John Tyndall began making qualitative predictions of the effect of changes in atmospheric gas concentrations and global climate in 1864 [*Sherwood*, 2011]. In the late 1890s, Nobel Laureate Svante Arrhenius proposed a quantitative relationship between carbon dioxide (CO_2) released from coal burning and global temperature [*Sherwood,* 2011]. A consensus gradually developed amongst the scientific community that increasing CO_2 emissions would have significant effects on the global climate and in 1988 the Intergovernmental Panel on Climate Change (IPCC) was formed by the United Nations to compile and review the current scientific research pertaining to climate change. Current IPCC predictions estimate that the increase in atmospheric greenhouse gasses will lead to temperature changes of 1.8-4.0°C and a sea level rise of 0.18 to 0.59 m by the year 2099 (relative to global averages 1980-1999) [*IPCC Report*, 2007]. In addition, scientists predict that extreme weather events (such as drought, severe storms, or heat waves) will become more frequent [*IPCC Report*, 2007].

1.2. Ocean Acidification

Scientists have known for decades that the world's oceans have the capability to absorb anthropogenic CO_2. In fact, initially scientists predicted that ocean uptake would negate any changes in atmospheric CO_2 due to anthropogenic emissions. However, more sophisticated measurements and longer data sets confirmed that CO_2 emissions were increasing at a rate far outpacing the oceanic uptake of CO_2 [*Keeling*, 1960]. As knowledge of the global carbon cycle

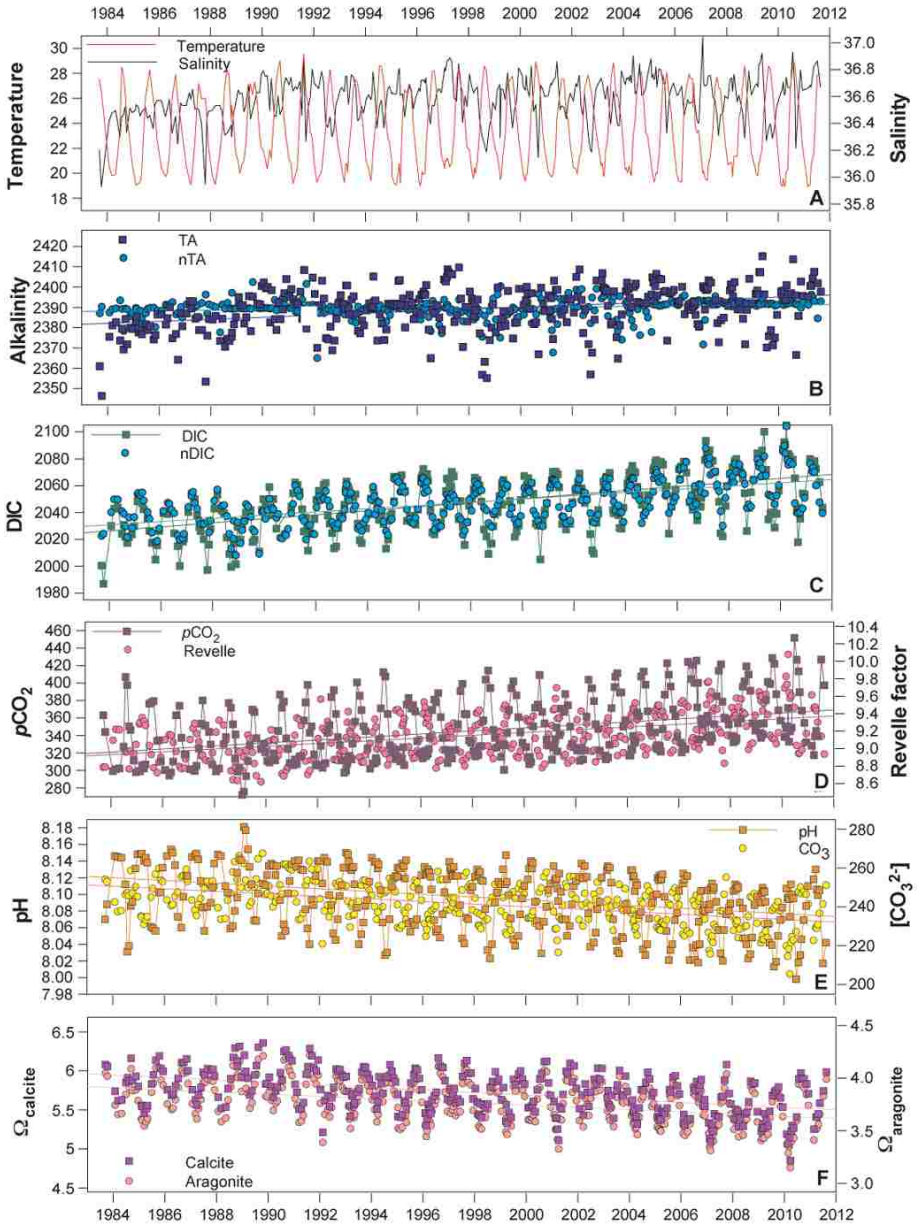

Figure 1.2.1. Trends in seawater parameters over the past 30 years from the Bermuda Atlantic Time Series (BATS) mooring near Bermuda in the western Atlantic Ocean. (A) Sea temperature (black squares) and salinity (red squares). (B) Total alkalinity (A_T, µmol kg^{-1}, blue squares) plotted with salinity normalized A_T (nA_T; µmol kg^{-1}, light blue squares). (C) Dissolved inorganic carbon (DIC, µmol kg^{-1}, green squares) and salinity normalized DIC (nDIC; µmol kg^{-1}, light blue squares). (D) Seawater pCO_2 (µatm; purple squares) and Revelle factor, the buffer factor for seawater (pink squares). (E) Seawater pH (orange squares) and [CO_3^{2-}] (µmol kg^{-1}, yellow squares). (F) Saturation state of calcite (Ω_{Ca}) (purple squares) and aragonite (Ω_{Ar}) (pink squares). All measurements were recorded at the sea surface. (Figure taken from *Bates et al*., 2012). Reprinted with permission from Copernicus publications.

and its role in ocean chemistry grew, scientists found that increases in atmospheric CO_2 were changing the ocean's chemistry. This process is known as "ocean acidification" because as the dissolved CO_2 in the ocean increases, ocean pH decreases (Figure 1.2.1). Uptake of atmospheric CO_2 since the beginning of the Industrial Revolution has decreased ocean pH by ~0.13 [*Dore et al.*, 2009]. This decrease in pH has already led to changes in the ocean carbonate system and could result in dramatic changes in many oceanic ecosystems.

1.2.1. The Marine Carbonate System

There are four measurable parameters of the carbonate system: the negative log of the hydrogen ion concentration (pH), the partial pressure of CO_2 ($p\,CO_2$), dissolved inorganic carbon (DIC), and total alkalinity (A_T). If two parameters are measured, the remaining carbonate species can be calculated using the following reactions and equilibria [i.e.*Park*, 1969; *Millero*, 1995; *Millero,* 2007]:

$$CO_2(g) \rightleftharpoons H_2CO_3^* \tag{1.1}$$

$$H_2CO_3^* \rightleftharpoons H^+ + HCO_3^- \tag{1.2}$$

$$HCO_3^- \rightleftharpoons H^+ + CO_3^{2-} \tag{1.3}$$

$$K_0 = \frac{[H_2CO_3^*]}{f(CO_2)} \tag{1.4}$$

$$K_1 = \frac{[H^+][HCO_3^-]}{[H_2CO_3^*]} \tag{1.5}$$

$$K_2 = \frac{[H^+][CO_3^-]}{HCO_3^-} \tag{1.6}$$

where $H_2CO_3^*$ in Equations 1.2, 1.4, and 1.5 is a hypothetical species combining $CO_2(aq)$ and H_2CO_3. $f(CO_2)$ is the fugacity of gas phase CO_2. DIC and A_T are defined by the following equations:

$$DIC = [H_2CO_3^*] + [HCO_3^-] + [CO_3^{2-}] \quad (1.7)$$

$$A_T = [HCO_3^-] + 2[CO_3^{2-}] + [OH^-] + [B(OH)_4{}^-] - [H^+] \quad (1.8)$$

$$K_B = \frac{[H^+][H_2BO_3^-]}{[H_3BO_3]} \quad (1.9)$$

$$K_w = [H_3O^+][OH^-] \quad (1.10)$$

Shipboard measurements of these parameters provide us with useful information about the global carbon cycle and marine ecosystems. It is estimated that the global oceans take up ~30% of anthropogenic CO_2 emissions [*Sabine et al.*, 2004; *Canadell et al.*, 2007; *Doney et al.*, 2009b]. Observations of pCO_2 and calculations of air-sea CO_2 flux into and out of the oceans have been important for determining overall oceanic CO_2 uptake [i.e. *Takahashi et al.*, 1995, 2002, 2009]. Biological productivity influences DIC and pCO_2; photosynthetic uptake of carbon draws down DIC concentrations whereas respiration increases DIC concentrations. As anthropogenic CO_2 continues to accumulate in the atmosphere and be taken up by the global oceans, changes result in the marine carbonate system. As described above, increasing atmospheric pCO_2 increases oceanic pCO_2 and DIC while decreasing ocean pH (Figure 1.2.1). A_T is generally a conservative property controlled by evaporation and precipitation (and the concurrent salinity changes) [*Millero et al.*, 1998]. However, changes in $[CO_3^{2-}]$ and $[HCO_3^-]$ in the marine environment due to decreasing pH will result in a decrease in the buffering capacity of seawater and in lesser rates of atmospheric CO_2 uptake [*Egleston et al.*, 2010].

1.2.1.1. $CaCO_3$ Saturation States

With measurement of two carbonate system parameters, another important parameter can be calculated using the thermodynamic relationships discussed above: calcium carbonate saturation states. The two main calcium carbonate minerals, calcite and aragonite, are biologically important for a variety of marine organisms including coral, bivalves, coccolithophores, and pteropods, [*Zondervan et al.*, 2001; *Doney et al.*, 2009a; *Kleypas and Yates*, 2009; *Comeau et al.*, 2012]. The saturation state (Ω) of calcite or aragonite is a measure of how likely the mineral is to form or dissolve. For calcite:

$$\Omega_{Ca} = \frac{[Ca^{2+}][CO_3^{2-}]}{K^*_{spCa}} \tag{1.11}$$

And for aragonite:

$$\Omega_{Ar} = \frac{[Ca^{2+}][CO_3^{2-}]}{K^*_{spAr}} \tag{1.12}$$

where K^*_{sp} is the apparent solubility product for either calcite (Ca) or aragonite (Ar) and is dependent on temperature, salinity, and pressure. When Ω>1, the solution is supersaturated and precipitation is thermodynamically favored; when Ω<1, dissolution is favored. Aragonite has a larger K^*_{sp} and so is more soluble than calcite at the same ion concentration product of Ca^{2+} and CO_3^{2-}. Globally-averaged values for Ω_{Ca} and Ω_{Ar} are 4.58 and 2.98, respectively, in open ocean surface waters [*Feely et al.*, 2009], but Ω varies by ocean basin and by region. Calcite and aragonite are supersaturated in surface waters because inorganic phosphate, magnesium, and some organics inhibit non-biogenic precipitation of calcium carbonate minerals [*Pytkowicz*, 1973] and thus high concentrations of free carbonate ion (CO_3^{2-}) in surface waters are sustained.

When Ω<1.0, dissolution is thermodynamically favorable. Because decreasing pH results in decreasing CO_3^{2-} concentrations (Equations 1.11, 1.12), ocean acidification results in decreasing Ω and may have detrimental effects on the health of some marine calcifiers [*Fabry et al.*, 2008; *Kroeker et al.*, 2010; *Comeau et al.*, 2012] (Figure 1.2.2). Even at values >1.0, lowered Ω can still decrease rates of calcifier growth or cause larvae mortality [*Fabry et al.*, 2008; *Kroeker et al.*, 2010; *Comeau et al.*, 2012]. Since many marine calcifiers make up the lower trophic levels in the marine ecosystem, ocean acidification could have far-reaching effects on the marine ecosystem.

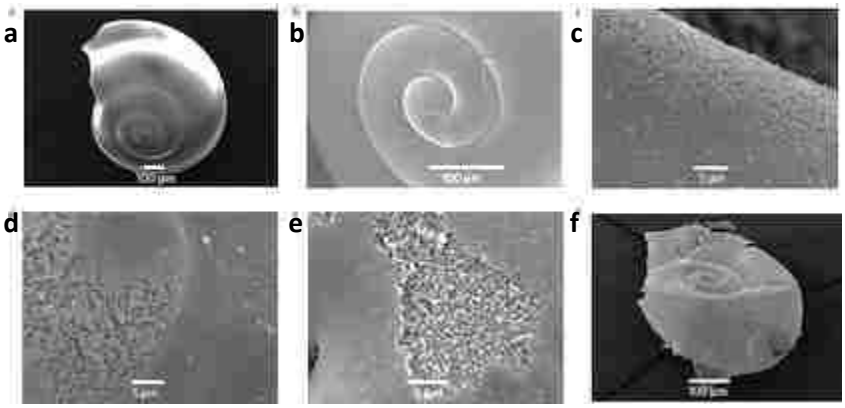

Figure 1.2.2. Different levels of *Limacina helicina Antarctica* shell dissolution caused by seawater Ω_{Ar} near 1.0 in the Southern Ocean. The images were captured using a scanning electron microscope. (a,b) Shells with no visible signs of dissolution. (c) Slight dissolution of the outer layer of a juvenile *Limacina helicina Antarctica* shell. (d) Extensive dissolution of the outer shell layer. (e) Outer shell layer dissolved and inner shell layer partially dissolved. (f) Fragmentation of the shelf due to low Ω_{Ar} conditions. (From *Bednarsek et al.,* 2012). Reprinted with permission from Macmillan Publishers Limited.

Saturation states naturally decrease with depth because of higher pCO_2 in deep ocean waters. CO_2 dissolves more readily in colder waters than warmer waters so as deep ocean waters form at the poles, they take up more CO_2 as they cool. Colder water is more dense than warmer water and so these higher CO_2 waters sink [*Raven and Falkowski*, 1999]. In addition to this marine

carbon system solubility pump, the biological carbon pump also contributes to higher deep water CO_2; it exports a fraction of carbon particulates that result from surface biological production to interior waters where it is then respired by microbes and zooplankton [*Volk and Hoffert*, 1985]. This increased CO_2 at depth lowers the pH and consequently shifts the carbonate system equilibrium away from carbonate ions, resulting in lowered Ω at depth. Over the past 150 years, ocean acidification has led to changes in the "saturation horizons" for aragonite and calcite, the depth where Ω=1.0. Since the pre-industrial period saturation state horizons across the North Pacific have shoaled between 30-100 m [*Feely et al.*, 2002] due to anthropogenic increases in CO_2 and the resultant ocean acidification.

1.3. Coastal Upwelling

Eastern Boundary Upwelling Systems (EBUS) are particularly at risk from ocean acidification. Located at the eastern edge of subtropical gyres (e.g. western North America and South America, and eastern Northern Africa), EBUS are highly productive ecosystems. Equatorward winds (most common in summer) combine with the Coriolis effect to force nutrient-depleted surface waters toward the open ocean and nutrient-rich bottom waters upwell to take their place. This upwelling-induced nutrient replenishment of the photic zone makes EBUS globally important fisheries [*Pauly and Christensen*, 1995]. However, along with bringing nutrients to the surface, upwelling also brings low-Ω water to the surface. This natural effect is exacerbated by the decreasing trend in both Ω_{Ca} and Ω_{Ar} driven by the anthropogenic increase in CO_2. Decreases in both Ω_{Ca} and Ω_{Ar} can affect both calcite and aragonite-based calcifiers. The upwelling of low aragonite saturation state waters along the coast and the potential detrimental effects of low Ω_{Ar} on marine organisms at the base of the food chain could have severe impacts on the marine ecosystem. In the California Current System (CCS) along the U.S. West Coast upwelling of low

Ω_{Ar} water has resulted in larval production losses in coastal shellfish hatcheries [*Feely et al.*, 2010; *Barton et al.*, 2012; *Harris et al.*, 2013]. Although adult oysters are primarily composed of calcite, the larvae are mainly aragonite. Because low Ω_{Ar} reduces growth and often results in mortality in the economically-important oyster larvae, our focus will be on Ω_{Ar} dynamics instead of Ω_{Ca} changes. In addition, high-magnesium calcite, biologically important for other calcifiers such as coralline algae, sea urchins, or calcifying plankton [see *Kurihara and Shirayama,* 2004; *Morse et al.,* 2006; *Ries et al.,* 2009], is even more soluble than aragonite [*Morse et al.,* 2006]. Aragonite is therefore often focused on in ocean acidification research because it is a "first offender" or a bellwether to the changes in the marine ecosystem than may be caused by ocean acidification.

Future predictions of Ω_{Ar} in the CCS look bleak. Modeling studies of Ω_{Ar} changes under the IPCC's SRES A2 emissions scenario (at the higher end of, but not the most extreme, CO_2 emissions predictions) [*Nakicenovic et al.*, 2000] predict that by 2050 average Ω_{Ar} in the CCS will have decreased from a pre-industrial estimate of Ω_{Ar}=2.58±0.19 to a predicted average Ω_{Ar} of 2.27±0.20 in 2050, with the volume of aragonite undersaturated water in the shelf euphotic zone increasing from 0% in pre-industrial times to >50% by 2050 [*Gruber et al.*, 2012] .

Coastal upwelling zones like the CCS are likely to experience ocean acidification sooner and with greater severity than other areas of the global oceans. For these reasons regions like this are key areas of research to assess the environmental and economic impacts of ocean acidification. Although significant improvements have been made over the past five years in both observations of periods of low aragonite saturation and predictive capabilities of future changes in Ω_{Ar}, these studies have largely been based on short-term "snapshots" of carbonate system variability from research cruises [e. g. *Hales et al.,* 2005b; *Feely et al.*, 2008; *Bates et al.*, 2009; *Jiang et al.*,

2010; *Cao et al.*, 2011; *Fassbender et al.,* 2011], or modeling from monthly climatologies of ocean pH [*Hauri et al.*, 2009; *Gruber et al.*, 2012]. More temporally-detailed observations of the carbonate system are needed to characterize the natural range, better understand the controlling mechanisms of Ω_{Ar} in coastal upwelling zones like the CCS, and determine how future changes due to anthropogenic climate change (i.e. increasing upwelling intensity and duration, precipitation changes, anthropogenic eutrophication of coastal waters) will impact these areas.

Autonomous instruments for measuring the carbonate system parameters make these more detailed observations possible. Commercially available sensors now exist for mooring-based measurements of pCO_2 [*DeGrandpre et al.*, 1995; *Schar et al.*, 2009] and pH [*Seidel et al.*, 2008; *Martz et al.*, 2010]. The SAMI-CO_2 has been used extensively in the field, but at the time this research began, *Gray et al.* [2011; 2012] had conducted the only extended field studies using the SAMI-pH – one a short (two month) deployment off the California coast [*Gray et al.*, 2011] and three short (two month) deployments on a coral reef [*Gray et al.*, 2012]. The SAMI-pH determines the pH of seawater spectrophotometrically using a colorimetric pH indicator. This method provides the greater accuracy and precision needed for marine carbonate system measurements compared to electrode seawater pH measurements [*Dickson*, 1993; *Martz et al.*, 2003; *Seidel et al.*, 2008]

Together, pH and pCO_2 measurements can be used to calculate the other carbonate system parameters and autonomous pH and pCO_2 sensors allow for the more detailed characterization of carbonate system dynamics in a variety of oceanic ecosystems, including the highly dynamic CCS. *Gray et al.* [2011, 2012] found that data from the Submersible Autonomous Moored Instruments for pH and pCO_2 (SAMI-pH and SAMI-CO_2) [*DeGrandpre et al.*, 1995, 1999; *Seidel et al.*, 2008] could be used in tandem or with salinity-derived alkalinity (A_{Tsalin}) to

accurately calculate aragonite saturation states in the field. Since these instruments record high-temporal resolution pH and pCO_2 datasets, they can be used to collect detailed intra-seasonal and inter-annual carbonate system data.

Several studies have found evidence of human-caused "acidified" water upwelling onto the continental shelf in the CCS. [*Feely et al.*, 2008] observed several low-pH upwelled waters during a series of hydrographic surveys along the continental shelf of the western North America in May of 2007. During an upwelling event recorded on this survey off the coast of Northern California, *Feely et al.* [2008] calculated that the saturation state horizon for aragonite shoaled all the way to the surface near the coast, conditions not predicted to occur in the open ocean until 2050 [*Orr et al.*, 2005]. *Evans et al.* [2011] found high concentrations of CO_2 in surface waters during the 2008 summer upwelling season. *Barton et al.* [2012] recorded aragonite undersaturated waters in an estuary-based oyster hatchery on the Oregon Coast during the summer of 2009. These studies all indicate that aragonite undersaturation is occurring in the Oregon coastal upwelling zone, making it an ideal location to study the extent and duration of these undersaturation events using the high temporal resolution of the SAMI-pH and SAMI-CO_2.

1.4. Research Objectives and Major Findings

As stated in the Research Summary at the beginning of this chapter, the objectives of my research focused on **(1) improving the performance of the SAMI-pH, (2) evaluating methods of field data validation and the feasibility of using the SAMI-pH/SAMI-CO_2 pair for calculation of the other carbonate system parameters, and (3) characterization and analysis of the carbonate system in the Oregon coastal upwelling zone.**

Instrument performance was improved by re-valuating he temperature dependence of the molar absorptivities for the pH indicator m-Cresol Purple using both SAMI-pH instruments and the bench-top UV-Vis. The variation in the molar absorptivity temperature dependence between SAMIs was found to be within the constraints of the variation for these relationships determined on the bench-top UV-Vis. Thus one set of molar absorptivity temperature relationships was applied to all SAMI-pH instruments. Three deployments of the SAMI-pH/SAMI-CO_2 pair during different oceanic conditions were carried out. Considerable offsets between the different parameter combinations used to calculate Ω_{Ar} were discovered and SAMI-pH or SAMI-CO_2 paired with a salinity-derived alkalinity was found to give more accurate calculations of Ω_{Ar}. These combinations were then used to calculate carbonate system dynamics for the Oregon coastal upwelling zone. This high temporal resolution dataset is one-of-a-kind and resulted in unprecedented characterization of carbonate system dynamics and examination of the mechanisms controlling these dynamics.

CHAPTER 2

Characterization of pH Indicators

2.1. m-Cresol Purple Characterization

2.1.1. Introduction

The SAMI-pH uses a pH indicator method to determine the pH of a seawater sample. The pH indicator currently used is the diprotic sulfonephthalein indicator m-Cresol Purple (mCP). mCP is mixed with the seawater sample and equilibrium is established:

$$HI^- \rightleftharpoons I^{2-} + H^+ \qquad (2.1)$$

where HI^- is the protonated (acid) form and I^{2-} is the un-protonated (base) form of the diprotic mCP.

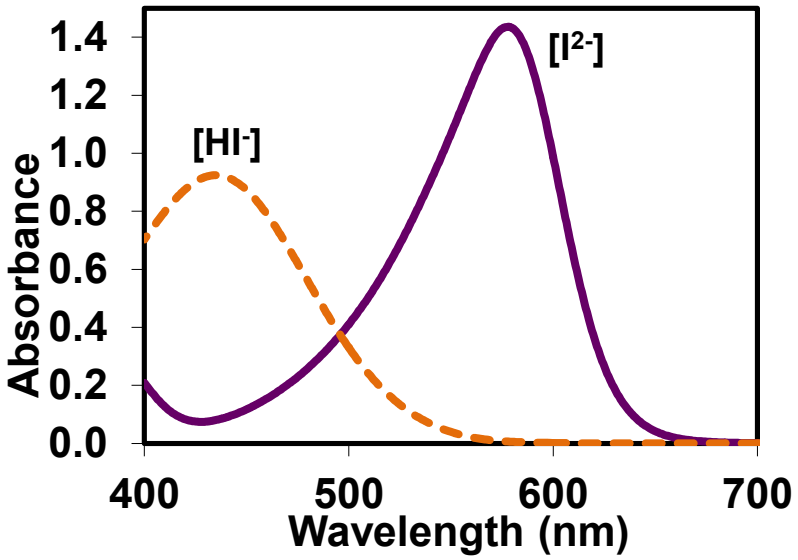

Figure 2.1.1. mCP spectra from Aldrich-211761, batch #11517KC. Concentration for the acid solution (pH~4) was 5.14 x 10^{-5} M and the base solution (pH~14) concentration was 3.65 x 10^{-5} M. Ionic strength ~0.7 mol kg-solution^{-1}. The pathlength was 1 cm.

The acid and base forms of mCP absorb at distinct wavelengths: 434 nm (acid) and 578 nm (base) (Figure 2.1.1). Since the ratio of protonated to un-protonated mCP depends upon the pH, the ratio of the absorbances at each wavelength can be used to calculate the pH of the solution. By combining Beer's law,

$$A = \varepsilon bc \tag{2.2}$$

where A is the absorbance, ε is the molar absorptivity, b is the pathlength, and c is the concentration, with the Henderson-Hasselbach equation,

$$pH = pK_a' + log\frac{[I^{2-}]}{[HI^{-}]} \tag{2.3}$$

where K_a' is the temperature and salinity-dependent acid dissociation constant for mCP, and the equilibrium equation for mCP (Equation 2.1), pH can be determined:

$$pH = pK_a' + \log\frac{R-e_1}{e_2-Re_3} \tag{2.4}$$

where R is the absorbance ratio (A_{434}/A_{578}) and e_1, e_2, and e_3 are ratios of the molar absorptivity of the base (ε_b) and acid (ε_a) forms of the indicator at 434 and 578 nm:

$$e_1 = \frac{\varepsilon_{a578}}{\varepsilon_{a434}} \tag{2.5}$$

$$e_2 = \frac{\epsilon_{b578}}{\varepsilon_{a434}} \tag{2.6}$$

$$e_3 = \frac{\varepsilon_{b434}}{\varepsilon_{a434}} \tag{2.7}$$

The molar absorptivities for mCP are temperature dependent [*Zhang and Byrne,* 1996] – a pH error of 0.006 pH units results from a 10° C temperature change if the temperature dependence is not included [*Seidel et al.,* 2008]. Temperatures in the Oregon coastal upwelling zone range from

near 8 to 18° C, depending on the season [*Huyer et al,* 2007] so correctly accounting for the mCP temperature dependence is important for maintaining the ±0.003 stated accuracy of the SAMI-pH for long-term deployments. A temperature relationship for mCP had been determined with a SAMI-pH previously [*Seidel,* 2006], but no temperature dependence had been determined since extensive changes were made to the SAMI electronics and optical cell.

2.1.2. Methods

Experiments were carried out using two SAMI-pH instruments, SAMI-59 and SAMI-68, and using a Varian Cary 300 UV-Vis bench-top spectrophotometer. Four test solutions were made to determine molar absorptivities at each of five temperatures between 5-25 °C (5, 10, 15, 20, and 25°C). The test solutions were comprised of saline solutions (ionic strength ~0.7 mol kg-solution^{-1}) in which either I^{2-} or HI^{-} was the predominant form of the indicator: two basic solutions (pH~12) – one blank and one with an mCP concentration of ~1.9 x 10^{-5} mol/kg – and two acid solutions (pH~5) – one blank and one with an mCP concentration of 5.6 x 10^{-5} mol/kg (see details mCP solutions in *Seidel* [2006] using mCP sodium salt (Aldrich-211761, batch #11517KC)). Unpurified mCP sodium salt (Aldrich-211761, batch #11517KC) was used to make the solutions in these experiments. It should be noted that these experiments took place prior to the publication by *Liu et al.,* [2011] who determined that the impurities in the mCP sodium salt solution altered the measured spectrophotometric pH. mCP was subsequently purified and the impure and pure mCP solutions were compared to determine a pH correction for pH>8.0 which could be applied to all field data obtained using that batch of mCP (#11517KC) (See more details in section 3.3.3). ε‘s were calculated at each temperature from the absorbances of the acid and base mCP solutions using Beer’s Law (Equation 2.2). Experiments on both the SAMIs and the Cary 300 were run at 5, 10, 15, 20, and 25°C. The temperature equilibration

procedure differed slightly between the two SAMI-pHs tested. Both SAMIs were placed in a test tank and temperature-equilibrated using a water bath thermostated to within ±0.04°C of the goal temperature. SAMI-59's electronics were allowed to equilibrate to the test tank temperature for one hour before measuring the ε's every 15 minutes for 8 total measurements at each temperature. This procedure was then repeated for the next temperature. Instead of waiting for one hour for the electronics to equilibrate to the water bath temperature, SAMI-68 measured the e_i's continuously for four hours after the water bath temperature was changed.

Bench-top UV-Vis experiments were thermostated to within ±0.22°C of the goal temperature. After each temperature change, the optical cell was first allowed 30 minutes to temperature equilibrate and each sample measured was allowed an additional 10 minutes to equilibrate to the experimental temperature. e_i's were measured on the UV-Vis for the same temperatures between 5-25°C as the two SAMI-pHs. A total of five separate mCP temperature dependence experiments were completed on the bench-top UV-Vis.

2.1.3. Results and Discussion

The results from the two SAMI-pH experiments are shown in Figure 2.1.2 compared with the previously-calculated bench-top UV-VIS e_i's [*Seidel*, 2006].

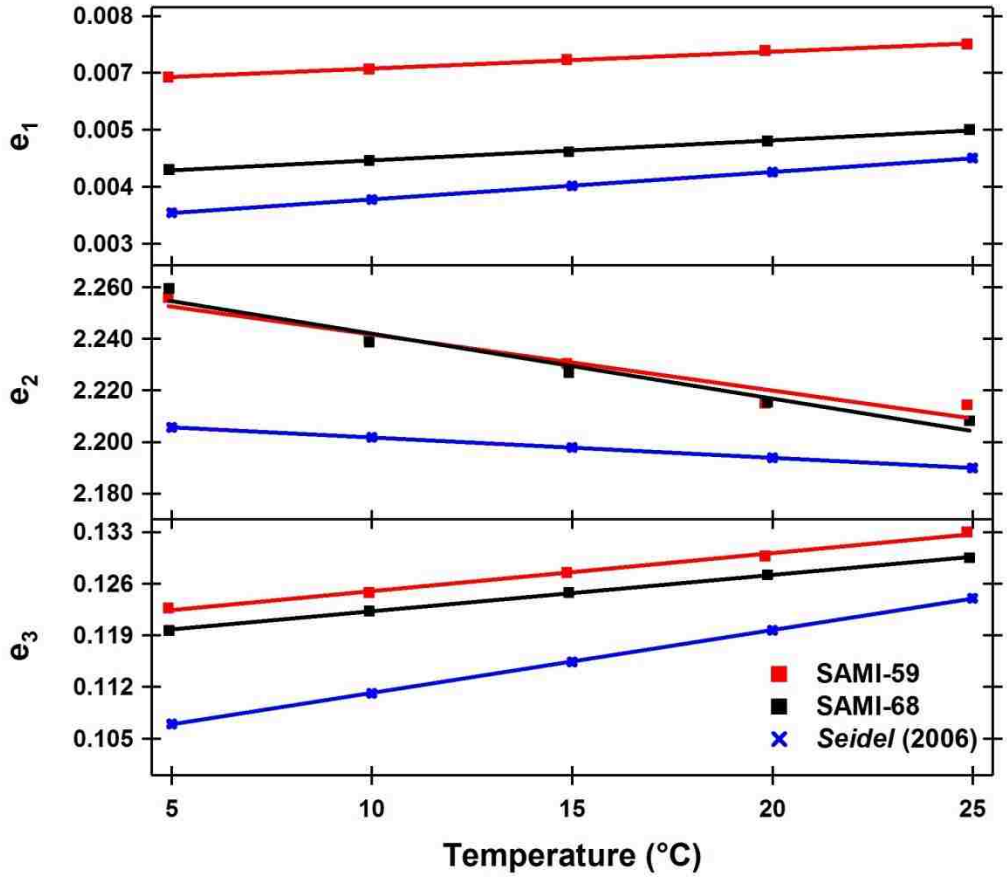

Figure 2.1.2. SAMI e_i temperature dependence compared to the temperature dependence previously determined on the bench-top UV-Vis by *Seidel* [2006]. Linear fit equations are found in Table 2.1.1.

e_1 and e_3 both increase with temperature and e_2 decreases with temperature (Figure 2.1.2). This is due to both a slight spectral shift to longer wavelengths in the mCP base peaks and to shorter wavelengths for the acid peaks and changes in the absorbance maxima. The absorbances at the peak wavelengths for both acid (434 nm) and base (578 nm) decrease as temperature increases and at the same time the non-peak absorbance (578 nm for acid and 434 nm for base) increase from their minima. The effect of temperature on the mCP absorbance peaks can be found in Figure 2.1.3. The 434 nm peak in the spectra of the acidic form of mCP is wider than the 578 nm

peak of the basic form, resulting in smaller changes in the measured intensities of both acid and base at 434 nm as the spectra shift with increasing temperature.

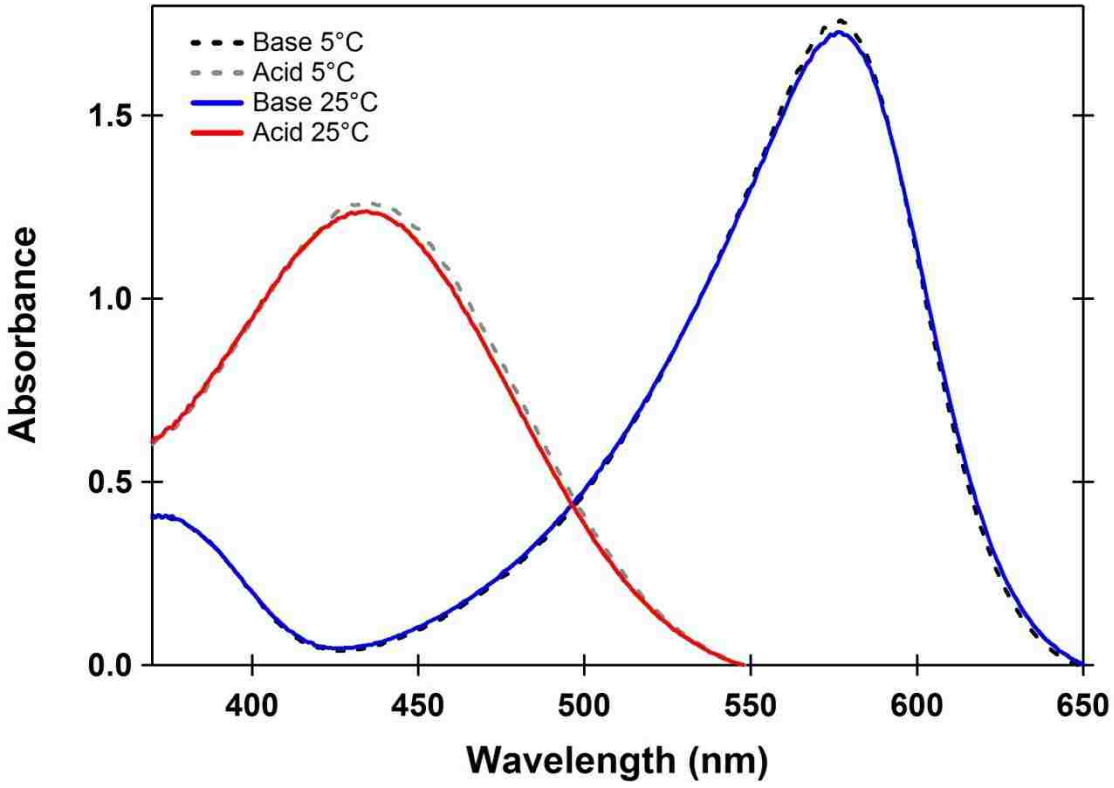

Figure 2.1.3. mCP (Aldrich-211761, batch #11517KC) spectra for acid (434 nm) and base (578 nm) at 5°C (black and gray dashed lines) and at 25°C (blue and red lines). Ionic strength = 0.7 mol kg-solution^{-1}.

A small difference in bandpass exists between the instruments. With the slight shift in spectra due to temperatures, the bandpass will cover a different section of the absorbance peaks at each wavelength. Because the acidic 434 nm peak is much wider than the basic 578 nm peak, this results in a much smaller change in absorbance at 434 nm with increasing temperature than at 578 nm. Thus the molar absorptivity temperature dependences for ε_{a578} and ε_{b578} differ more between the two SAMIs.

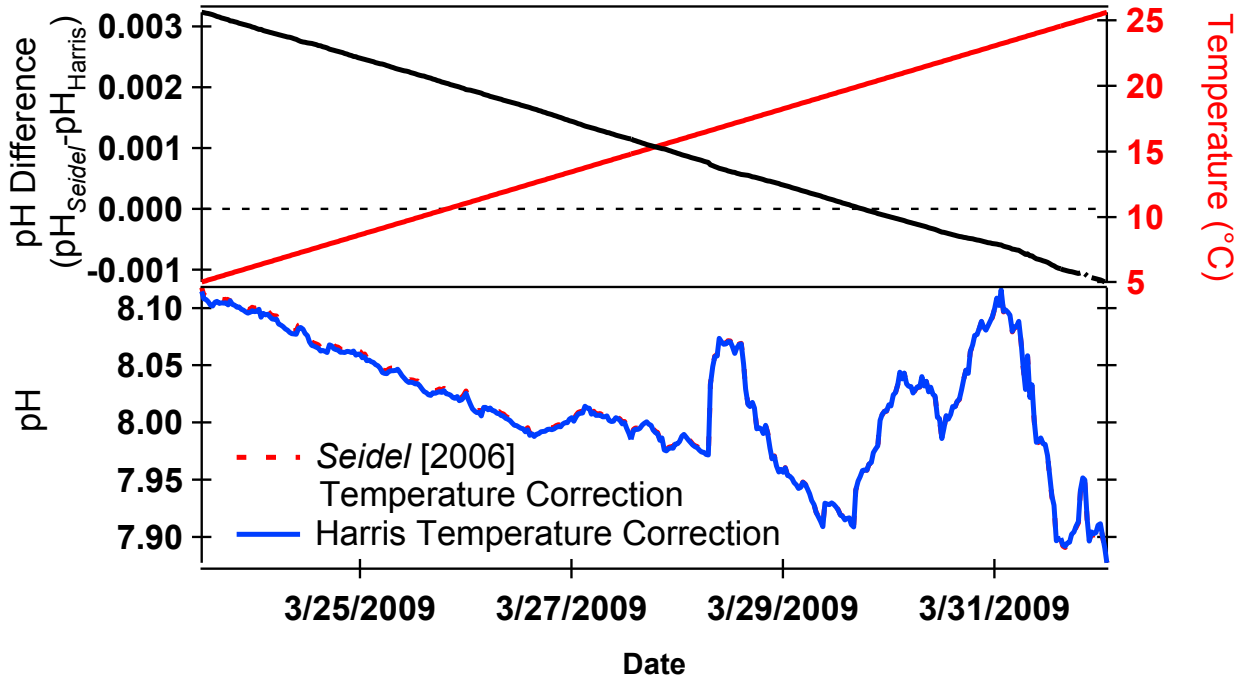

Figure 2.1.4. (Bottom) In situ pH calculated using the ε temperature dependences determined by *Seidel* [2006] and by K. Harris. Because the in situ temperature change during this period was small, a temperature range (5 to 25°C) was applied to the data (top, red). Since the difference between pH_{Seidel} and pH_{Harris} is small compared to the in situ pH changes, the difference between the two pH calculations is plotted at top (black line).

The averaged SAMI-pH ε temperature relationships (Table 2.1.1) were used to calculate pH from a field deployment using SAMI-68 (Figure 2.1.4). This calculated pH was compared to pH calculated from the same data using the previously determined mCP temperature relationships [*Seidel*, 2006]. Because the temperature range of the field data was relatively small (< 1°C) a temperature range of increments of 0.1°C (from 5 to 25°C) was used instead for pH calculation (see Figure 2.1.4). Figure 2.1.4 shows that at low temperatures, the difference between pH calculated using the old [*Seidel,* 2006] and Harris temperature relationships is > 0.003 pH units. The difference between the separate temperature relationships derived for SAMI-59 and SAMI-68 was < 0.0005 pH units at 5°C. This difference between Harris and *Seidel* [2006] pH calculations was attributed to changes in the SAMI-pH electronics. Because the two temperature

relationships result in a difference greater than the accuracy of the SAMI (±0.003), the Harris temperature relationship is now used for the SAMI-pH.

Table 2.1.1. Slopes (m $°C^{-1}$), intercepts (b), average (Avg.), and standard deviation (σ) for SAMI e_i linear temperature relationships and the relationships determine by *Seidel* [2006]. Ionic strength in all mCP solutions tested was 0.7 mol kg-solution^{-1} (See Figure 2.1.2).

	e1		**e2**		**e3**	
	m	**b**	**m**	**b**	**m**	**b**
SAMI-59	0.0000384	0.00622	-0.00216	2.26	0.000516	0.120
SAMI-68	0.0000458	0.00404	-0.00252	2.27	0.000493	0.117
Avg.	0.0000421	0.00513	-0.00234	2.27	0.000504	0.119
σ	0.0000052	0.00154	0.00025	0.00	0.000016	0.002
Seidel	*0.0000626*	*0.00299*	*-0.00079*	*2.21*	*0.000852*	*0.103*

By comparing differences in the calculated molar absorptivity temperature dependencies from different trials on the bench-top UV-Vis to those between different SAMIs, the variation between SAMI molar absorptivity temperature dependencies was determined to be within the standard deviation of the bench-top experimental values for slope and intercept for ε_{b434} and ε_{b578} and close to the same standard deviation for ε_{a434} and ε_{a578}. This meant that one set of linear temperature dependences can be applied to all SAMI-pH's (see Equations 2.8-2.11). Figure 2.1.5 shows the e-value temperature dependencies for all Cary trials compared to those for the two SAMIs tested. The slopes and intercepts for the ε temperature dependences for the bench-top UV-Vis (Cary) and SAMI trials can be found in Table 2.1.1 and Table 2.1.2.

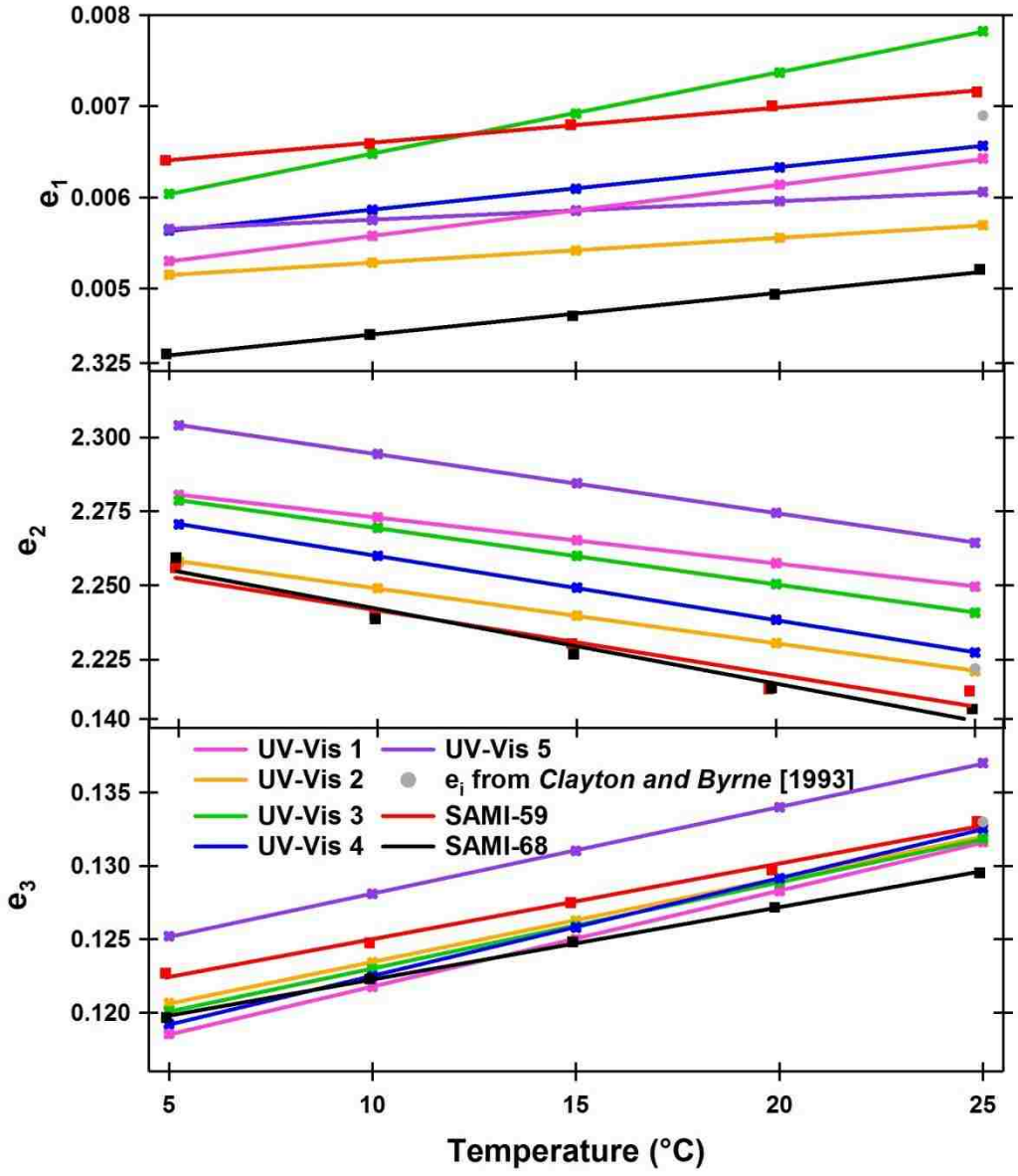

Figure 2.1.5. SAMI-pH and bench-top UV-Vis e_i temperature dependence for mCP (Aldrich, batch #11517KC). Ionic strength was 0.7 mol kg-solution^{-1}. The UV-Vis number refers to the different experiments run on the bench-top UV-Vis (on different dates, see Table 2.1.2). The equations for the linear fit can be found in Table 2.1.2. These are compared to the literature value for e_i from *Clayton and Byrne* [1993].

Table 2.1.2. Slopes (m, kg mol^{-1} cm^{-1} $°C^{-1}$), intercepts (b, kg mol^{-1} cm^{-1}), average (Avg.), and standard deviation (σ) for the bench-top UV-Vis (Cary) ε linear temperature relationships for mCP.

	e_1		e_2		e_3	
	m	**b**	**m**	**b**	**m**	**b**
UV-Vis 1 (7/28/09)	0.0000561	0.00502	-0.00155	2.288	0.000654	0.115
UV-Vis 2 (10/19/09)	0.0000272	0.00502	-0.00185	2.268	0.000568	0.118
UV-Vis 3 (11/24/09)	0.0000892	0.00559	-0.00190	2.288	0.000587	0.117
UV-Vis 4 (1/12/10)	0.0000465	0.00540	-0.00217	2.282	0.000666	0.116
UV-Vis 5 (1/27/10)	0.0000203	0.00555	-0.00198	2.314	0.000589	0.122
Avg.	0.0000479	0.00532	-0.00189	2.288	0.000613	0.118
σ	0.0000272	0.00028	0.00023	0.017	0.000044	0.003

The following ε temperature dependence equations were determined by averaging the SAMI-pH equations (where T is the temperature in °C):

$$\varepsilon_{a434} = -24.45*T + 19064 \quad (2.8)$$

$$\varepsilon_{a578} = 0.6442*T + 98.13 \quad (2.9)$$

$$\varepsilon_{b434} = 6.334*T + 2263 \quad (2.10)$$

$$\varepsilon_{b578} = -98.33*T + 43175 \quad (2.11)$$

where the units for ε are mol kg^{-1} cm^{-1}. This temperature dependence applies over a temperature range 5-25°C at ionic strength of 0.7 mol kg-$solution^{-1}$ for Aldrich mCP batch #11517KC. These equations were used to calculate the e_i's (see Equations 2.5-2.7) and then pH (Equation 2.4) from SAMI-pH field data.

2.2. Thymol Blue Characterization

2.2.1. Overview

Thymol blue is another pH indicator that has an appropriate pK_a for determining the pH of seawater [*Zhang and Byrne*, 1996]. However, thymol blue offers the advantage that, at the time of this study, its pK_a' was known over a greater temperature and salinity range than for mCP (*Lefevre et al.,* 1993; *Mosley et al.,* 2004). In addition, literature review suggested that the thymol blue indicator contained fewer impurities than mCP [*Yao et al.,* 2007]. For these reasons, switching from mCP to thymol blue as the indicator for the SAMI-pH was considered.

2.2.1. Methods

Thymol blue studies were first done on the bench-top UV-Vis over a range of temperatures using the same general method discussed in section 3.1.2. Thymol blue sodium salt (Alfra Aesar, batch #H31WO32) solutions had the same concentration as the mCP solutions listed in section 3.1.2 and the ionic strength of these solutions was 0.7 mol kg-solution^{-1}. Because the temperature dependence of the spectral properties of thymol blue was only reported in terms of the e-values by [*Zhang and Byrne*, 1996] the e-value temperature dependences from the Cary trials were calculated from the experimentally-observed molar absorptivities (see Equations 2.5-2.7) and compared.

2.2.3. Results and Discussion

The experimentally-determined relationships between temperature and thymol blue e_i's are reported in Figure 2.2.1 and Table 2.2.1. The change in e_i's with temperature follow the same trends as those for mCP, suggesting a similar spectra shift to higher wavelength with higher

temperature. The different ε temperature relationships from the different bench-top UV-Vis experiments for thymol blue showed larger standard deviations in

Table 2.2.1. Slopes (m, $°C^{-1}$), intercepts (b, unitless), average (Avg.), and standard deviation (σ) for the bench-top UV-Vis e_i linear temperature relationships for thymol blue (Alfra Aesar, batch #H31W032) in a solution with an ionic strength of 0.7 mol kg-solution^{-1}. (See Figure 2.2.1).

Trial	e_1		e_2		e_3	
	m	b	m	b	m	b
UV-Vis 1 (1/20/11)	0.0000319	0.00515	-0.00297	2.235	0.000409	0.134
UV-Vis 2 (1/28/11)	0.000063	0.0038	-0.004	2.266	0.000265	0.136
UV-Vis 3 (2/1/11)	0.0000238	0.00469	-0.00472	2.487	0.000245	0.151
Avg.	*0.0000396*	*0.00455*	*-0.0039*	*2.329*	*0.000306*	*0.14*
σ	*0.0000207*	*0.00069*	*0.00088*	*0.137*	*0.00009*	*0.009*

both the slopes and intercepts than mCP. The lower solubility of thymol blue (a solubility of 41 mg/L compared to 730 mg/L for mCP [*SciFinder*]) may have resulted in impartially dissolved solutions, resulting in different absorbances between experiments. Different thymol blue stock solutions were used during the different bench-top UV-Vis experiments.

At this point, thymol blue studies were terminated. New literature [*Liu et al.*, 2011] referenced experiments that determined that thymol blue impurities were likely to be significant between different reagent batches and different suppliers, leading to pH errors as large as 0.01 [*Liu et al.*, 2011], comparable to the pH differences between different batches of mCP. *Liu et al.* [2011] suggested that the best way to deal with impurities in pH reagent batches is to use high-performance liquid chromatography (HPLC) to purify the reagent.

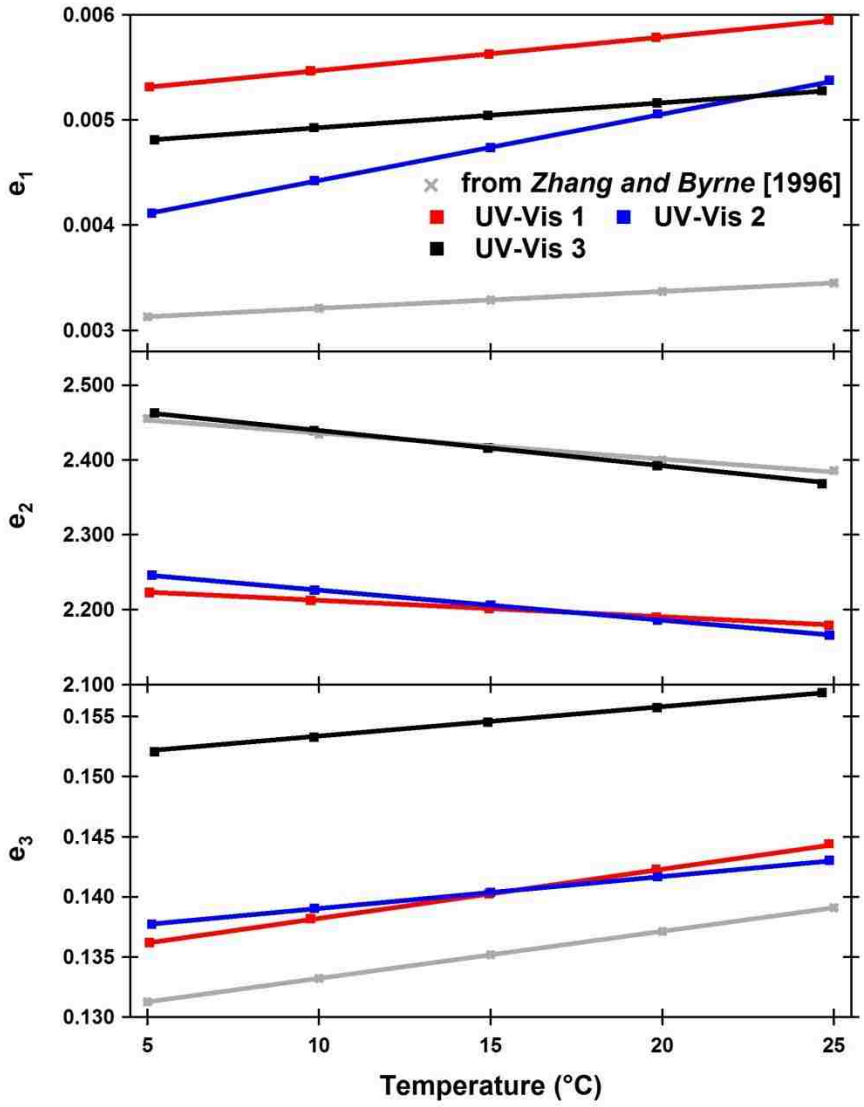

Figure 2.2.1. Bench-top UV-Vis e_i temperature dependence for thymol blue. The UV-Vis number refers to the different experiments run on the bench-top UV-Vis (on different dates, see Table 2.2.1). The equations for the linear fits can be found in Table 2.2.1.

CHAPTER 3

Field Studies Using Combined pH and pCO_2 Sensors

3.1. Field Site Overview

The waters above the Oregon continental shelf are part of the California Current System (CCS), an Eastern Boundary Current that runs from the southern part of British Columbia to Southern Baja California [*Lynn et al.,* 1987], as described in the Introduction. This site was chosen as part of a collaboration with Burke Hales from Oregon State University's College of Earth, Ocean, and Atmospheric Sciences (CEOAS). Oregon State University operates a mooring west of Newport, Oregon, (Figure 3.1.1) as part of the Oregon Coastal Ocean Observing System (ORCOOS) with semi-regular shipboard access. The mooring is in a coastal upwelling zone and thus the marine carbonate system was expected to be highly variable. In addition to inorganic carbon variability driven by upwelling, the Columbia River plume also occasionally influences carbonate system parameters (see Figure 3.1.2).

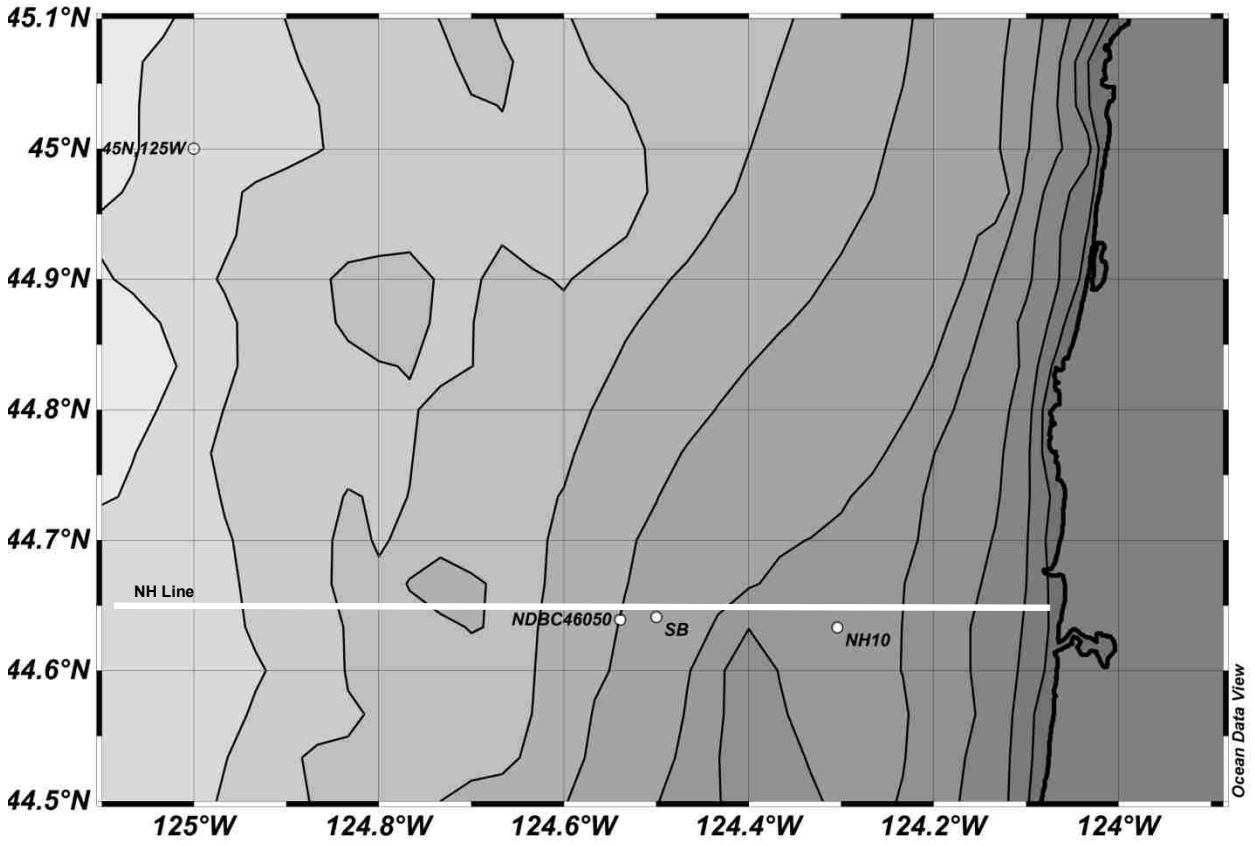

Figure 3.1.1. Location of the Newport Hydrographic (NH) line (white line) and the NH-10 and Shelf break moorings. The locations of the National Data Buoy Center NDBC meteorological buoy 46050 and the Pacific Fisheries Environmental Laboratory (PFEL)-derived upwelling indices (45°N, 125°W) are also noted. The bathymetry contour lines are for every 20 m of depth, i.e. NH-10 is located at the 80 m bathymetry contour.

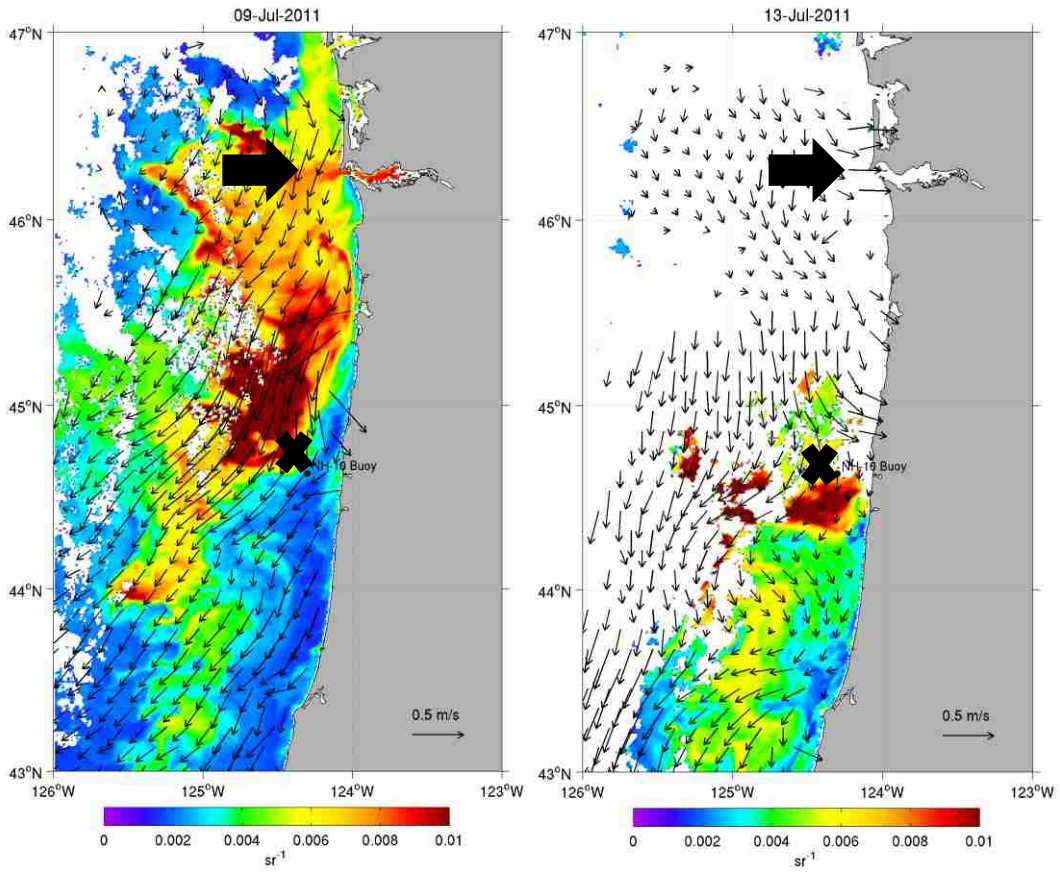

Figure 3.1.2. Evidence of the Columbia River plume on the Oregon shelf. Daily-averaged Moderate Resolution Imaging Spectroradiometer (MODIS) light scattering measurements of particulate organic matter in the water column on July 9, 2011 (left) and July 11, 2011 (right). High values (red) designate high concentrations of particulate organic matter indicating the presence of plume waters. The small arrows are the daily averaged surface current velocities. The location of the Columbia River mouth is marked by the large black arrow and the approximate location of NH-10 is marked by a black "x". White areas were covered by clouds and so no satellite measurements were taken for those areas. (Figure taken from *Risien et al.* [2012]). Reprinted with permission from Craig Risien, Oregon State University.

3.1.1. Newport Hydrographic (NH) line

The Newport Hydrographic (NH) sampling line runs west from the Oregon coast along latitude 44.65°N (Figure 3.1.1). This refers to a line of common shipboard sampling locations that stretch out into the Pacific Ocean west of the Oregon coast. The NH-10 mooring is located at the surface ~18 km (10 nautical miles) from the coast (124.304°W, 44.633°N) (see Figure 3.1.1). At

this location the water is ~80 m deep. The underwater contours (the bathymetry) along the NH-line is relatively uncomplicated - the seafloor gradually slopes away from shore to a well-defined shelf break and is unmarred by canyons [*Kundu and Allen*, 1976; *Kirincich and Barth*, 2009]. NH-10's location at the mid-point of the shelf [*Oke et al.*, 2002] and the uncomplicated underwater contouring of the NH Line make it an ideal location to study coastal upwelling dynamics. Submerged canyons and ridges can cause eddies as water upwells onto the shelf, complicating the overarching onshelf/offshelf direction of upwelling/downwelling.

3.1.2. Shelf Break Mooring

The shelf break mooring is also located along the NH Line where the water depth is 120 m, ~35 km from shore (124.500°W, 44.641°N) (see Figure 3.1.1). This is the location of the shelf break, which marks the edge of the continental shelf as it transitions from the gradual slope gradients of the continental shelf to the much steeper slope gradient of the continental slope. The shelf break mooring is located on the ocean floor below the National Data Buoy Center's meteorological buoy 46050 (see Figure 3.1.1). The location at the shelf break was chosen to capture the high CO_2, low pH California Undercurrent water as it first upwells onto the Oregon shelf.

3.2. Methods

3.2.1. SAMI-pH

The SAMI-pH (as described in much more detail by *Seidel* [2006] and *Seidel et al.* [2008]), and shown in Figure 3.2.1 uses the spectrophotometric method described in section 2.1 to determine the pH of a seawater sample. The SAMI-pH operates by first pumping in a seawater sample via a solenoid pump (Figure 3.2.2). After that a slug of pH indicator (~1.0×10^{-3} mol kg-solution^{-1} mCP (Aldrich-211761, batch #11517KC) at an ionic strength of 0.7 mol kg-solution^{-1}) is added

to the sample and mixed within a static mixer. Before the slug arrives at the optical cell, an absorbance blank is measured. As the slug of indicator passes through the cell, the absorbance is measured at three wavelengths: 434 nm (the HI^- absorbance peak), 578 nm (the I^{2-} absorbance peak), and 780 nm (a region of the spectrum where mCP does not absorb). Salinity and temperature-dependent pK_a is determined using temperature from the SAMI-pH, salinity from sensors attached to the mooring (discussed below), and the pK_a equation from *Clayton and Byrne* [1993]:

$$pK_a' = \frac{1245.69}{T} + 3.8275 + (0.00211)(35 - S) \quad (3.1)$$

Figure 3.2.1. The SAMI. (A) The SAMI-CO_2 and the SAMI-pH attached to the spar of the NH-10 buoy, pre-deployment. (B) NH-10 buoy during deployment. The SAMIs are ~2 m below the water's surface.

The pH can then be determined using Equation 2. 4 and is specified on the total pH scale, which includes both free hydrogen ions and takes into account the hydrogen ions from the reaction: $HSO_4^- \rightleftharpoons H^+ + SO_4^{2-}$. Because addition of pH indicator to the seawater sample introduces a small pH perturbation, absorbance measurements are taken over a range of indicator

concentrations. The pH at an indicator concentration of zero can be determined by extrapolation from the measured pH of decreasing indicator concentrations. Two versions of the SAMI-pH were deployed, the SAMI-pH and the SAMI^2-pH. The SAMI^2-pH has an updated housing, electronics and optical design. A schematic including the updated optical set-up and the inclusion of a second valve (explained below) can be found in Figure 3.2.3.

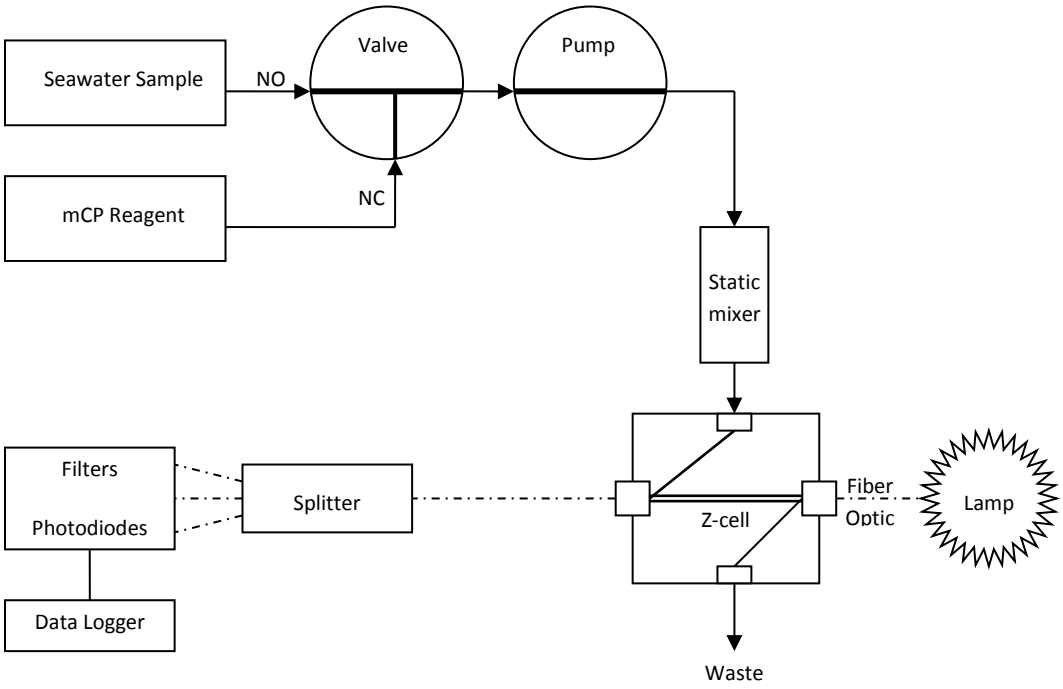

Figure 3.2.2. SAMI-pH schematic [from *Seidel,* 2006].

Prior to deployment, all SAMI-pH instrument accuracy is verified using certified tris(hydroxymethyl)aminomethane (tris) buffer solutions in artificial seawater [*Delvalls and Dickson*, 1998] at 20°C. A SAMI redesign adds an additional valve to the internal plumbing of the SAMI^2-pH (Figure 3.2.3) that allows the SAMI to run the certified tris buffer at a specified interval during deployment for in situ data validation.

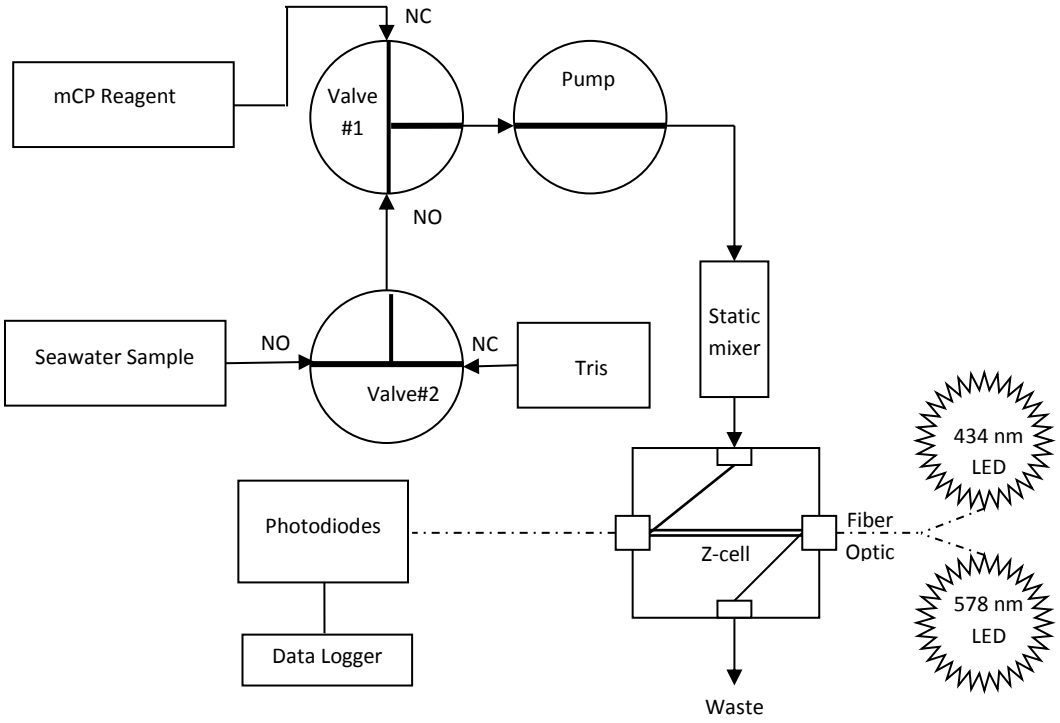

Figure 3.2.3. SAMI^2-pH schematic with tris valve set-up for in situ data validation.

3.2.2. SAMI-CO_2

Fundamentally, the SAMI-CO_2 operates in a similar manner to the SAMI-pH – the pCO_2 is measured by determining the absorbance ratios of the acid and base forms of a diprotic sulfonephthalein indicator (bromothymol blue, or BTB). BTB solutions of 5.6×10^{-5} mol kg-solution^{-1} were made from Sigma-Aldrich bromothymol blue sodium salt, # 114421-25G, in 8.48 mol kg-solution^{-1} NaOH. Instead of mixing pH indicator with a seawater sample as in the SAMI-pH, a solution of the indicator is pumped through a gas-permeable membrane where it is allowed to equilibrate with the seawater pCO_2 before being pumped through the optical flow cell to measure absorbances. The peaks for BTB correspond to 434 nm for the protonated (acidic) form and 620 nm for the un-protonated (basic) form.

pCO_2 is determined using the ratio RCO_2:

$$RCO_2 = -log\frac{R-e_1}{e_2-Re_3} \quad (3.2)$$

where R is (A_{434}/A_{620}) and e_i's are:

$$e_1 = \frac{\varepsilon_{a620}}{\varepsilon_{a434}} \quad (3.3)$$

$$e_2 = \frac{\varepsilon_{b620}}{\varepsilon_{a434}} \quad (3.4)$$

$$e_3 = \frac{\varepsilon_{b434}}{\varepsilon_{a434}} \quad (3.5)$$

pCO_2 is then calculated from RCO_2 (Equation 3.2) and the SAMI-CO_2 calibration coefficients [*DeGrandpre et al.*, 1995]. The SAMI-CO_2 is calibrated before deployment in a temperature-controlled water bath (10°C) over a range of pCO_2 values by comparing SAMI-CO_2 values to those measured by an infrared CO_2 analyzer (LI-COR LI-840).The SAMI-CO_2 calibration coefficients are fitted from this comparison [*DeGrandpre et al.*, 1995].

3.2.3. Other Measurements

In addition to the SAMI-pH and SAMI-CO_2 deployed at NH-10, the mooring itself was equipped with salinity (S) sensors (Sea-bird MicroCAT SBE37) at four depths (2 m, 10 m, 20 m, and 60 m) and temperature (T) sensors (Sea-bird SBE39) at 10 depths (4 m, 6 m, 8 m, 10 m, 15 m, 25 m, 30 m, 40 m, 50 m, 70 m). There was also a pyranometer (LI-COR LI-200) for measuring solar radiation. During two deployments (autumn 2009 and spring 2011) an oxygen (O_2) sensor (Aanderaa oxygen optode 4175) was deployed at the same depth (~2 m) as the SAMIs. At the shelf break, a conductivity-temperature-depth (CTD) sensor was deployed at a depth of 116 m alongside the SAMI-CO_2 and SAMI-pH to measure salinity, temperature, and pressure (P).

Discrete samples were collected during 2011 at a depth of ~5 m near the NH-10 mooring and later analyzed for pCO_2 and DIC using a modification of the method developed by *Bandstra et al.* [2006] to measure pCO_2 and DIC on the same sample. Discrete samples were not collected during other years due to logistical issues, i.e. difficulty in accessing the NH-10 and shelf break vicinities to take samples.

Wind speed and wind direction data were collected from the anemometer at NDBC station 46050 (Figure 3.1.1), shown to be representative of cross-shelf winds at NH-10 by *Hales et al.* [2006]. The 10-day running average of the north-south wind component was calculated in order to discern the strength and direction (i.e. upwelling or downwelling-favorable) of the winds. Six-hourly upwelling indices (UI) were obtained from the Pacific Fisheries Environmental Laboratory (PFEL) as an additional measurement of upwelling or downwelling intensities. Daily average river discharge for the Columbia River (CR) was obtained from the Columbia River Fisheries (CRF) for the farthest downstream station available (Bonneville, WA).

Satellite chlorophyll-a (chl-a) was retrieved from the European Space Agency's GlobColour database (http://hermes.acri.fr). Level-3 products were averaged [*Antoine,* 2004; *Lee,* 2006] from MODIS, SeaWiFS, and MERIS chl-a products. The Chl-a level-3 products used in this study were retrieved at a 1 km resolution for the 10 km x 10 km bin centered on NH-10 and averaged.

3.2.4. Inorganic Carbon Calculations

Inorganic carbon system calculations were made in CO2SYS [*Pierrot et al.,* 2006] using K_1 and K_2 calculated by *Mehrbach et al.* [1973] refit by *Dickson and Millero* [1987] and $KHSO_4$ from *Dickson* [1990] on the total pH scale. In addition to two carbonate system parameters (pH, pCO_2,

A_T, or DIC), in situ T, S, P were the inputs to calculate the remaining carbonate system parameters. Ω_{Ca} and Ω_{Ar} were also calculated in CO2SYS using K^*_{spAr} from *Mucci* [1983].

3.3. Data Quality Assessment

3.3.1. Introduction

The long-term deployment of SAMI-pH and SAMI-CO_2 pairs is a novel approach to characterizing inorganic carbon system dynamics. *Gray et al.* [2011; 2012] previously determined that high-temporal resolution [CO_3^{2-}] and Ω could be accurately calculated using pH and pCO_2 dataset inputs during several short-term (~2 month) deployments, as discussed previously. However, further methods of in situ data validation are required to verify the accuracy of the long-term pH and pCO_2 datasets and the inorganic carbonate parameters calculated from them.

In order to further study the usefulness of using paired SAMI-pH and SAMI-CO_2 measurements to calculate parameters of marine carbonate system, SAMI pairs were deployed together on the NH-10 mooring and at the shelf break (see locations in Figure 3.1.1). This data was also used to study carbonate system dynamics (see sections 3.4 and 3.5 below). The marine environment can be tough on instruments. As a result, SAMI failures were not uncommon. The hatched regions in Table 3.3.1 show where data was not recorded due to failure of the instrument, where biofouling made the collected data unusable, or when the moorings themselves were lost. Access to instrumentation on the NH-10 mooring is limited to deployment cruises approximately every six months so if an instrument failed during deployment it remained on the mooring until the NH-10 mooring was recovered.

Table 3.3.1. Timeline of NH-10 and shelf break deployments showing when data were successfully collected. The pCO_2 measurements in 2007-2009 were collected jointly with and have also analyzed by *Evans et al.,* [2011].

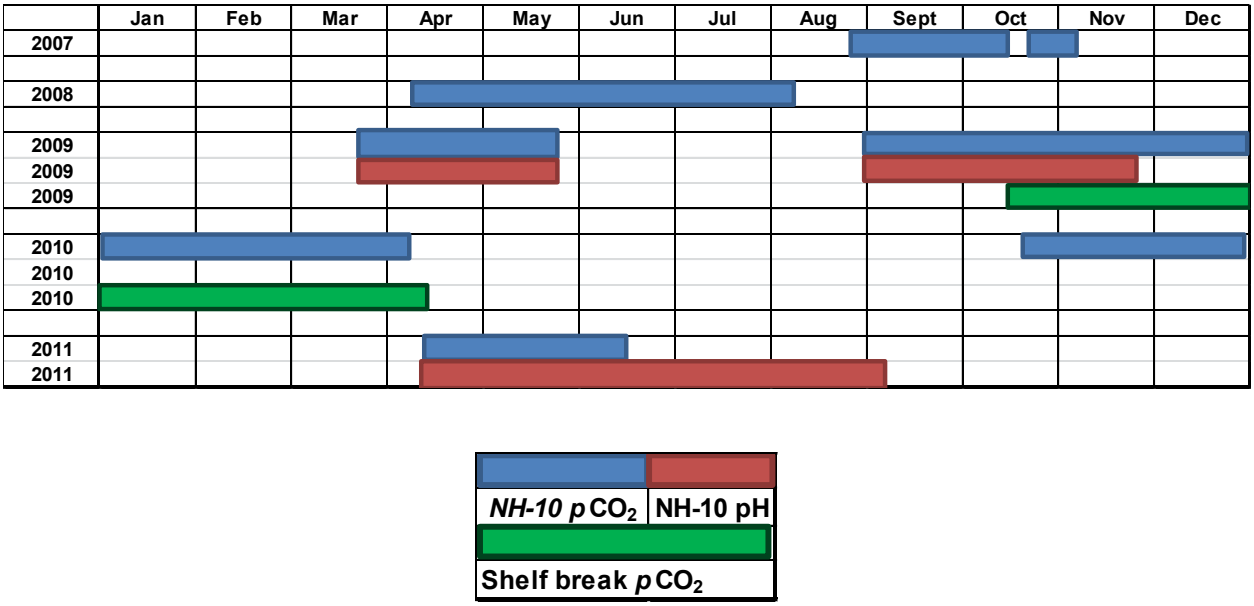

Several SAMI failures occurred during the five-year NH-10 time-line. Despite extensive battery testing [*Cullison,* 2010] battery failures occurred in two of the SAMI-pH instruments deployed. If the battery voltage dropped below 10 V, the SAMI was unable to pump in a seawater sample. Macroalgae biofouling also affected data collection, especially in instruments that were deployed over the highly productive summer upwelling season. In an effort to combat biofouling, copper tubing was placed around the inlet tube of the SAMI-pH. However, during one deployment the copper corroded to the point that the pump was no longer able to draw seawater samples through the inlet tubing. During another deployment, particulate matter got trapped early on in deployment in the SAMI-pH valve, resulting in it getting stuck in the "seawater sample" position. No pH reagent was added to the sample and so no accurate pH measurements were recorded. On another occasion, the reagent bag on a SAMI-CO_2 tore open towards the end of deployment. At one point during a winter storm in late 2010, the NH-10 mooring broke free of its anchor and ended up beached at Cape Disappointment, Washington. The SAMI-pH on this

deployment was found with its housing breached and its electronics flooded; no data was retrieved.

SAMI-pH and SAMI-CO_2 instruments at the shelf break mooring (Figure 3.1.1) also experienced failures (Table 3.3.2). Although the depth of the shelf break mooring meant that biofouling was not an issue as it was in surface waters, the depth had its own impact on the SAMIs. During two deployments, the SAMI pump became air-locked and was unable to pump either seawater sample or reagent. On another deployment, pressure built up within the SAMI-pH from gases released by the battery causing it to strip the screws holding the top bulkhead when it reached the surface during recovery. As a result, the electronics were flooded and no data were recovered. On the last shelf break deployment (in 2011), the acoustic release did not release during recovery and so the instruments remain on the shelf floor and no data were recovered. Nonetheless, the data that were collected resulted in a completely novel dataset with unprecedented temporal resolution spanning five years and all four seasons.

There are a number of approaches for validating the in situ SAMI-pH and SAMI-CO_2 measurements. We chose to analyze three methods available given the location and deployment timelines of the SAMIs. Discrete samples taken at the NH-10 buoy during deployments were analyzed and compared to SAMI data points from the same time. The SAMI-pH deployed during the spring and summer of 2011 was equipped with the seawater certified reference material (CRM) tris buffer as an in situ validation method. *Gray et al.* [2011] determined that a conservative salinity-derived alkalinity (A_{Tsalin}) could be used together with the SAMI data to quantitatively compare datasets measured by SAMI-pH and SAMI-CO_2. This inter-comparison allows us to verify the A_{Tsalin} relationship used to calculate inorganic carbonate parameters when both SAMI-pH and SAMI-CO_2 data are not available.

3.3.2. Discrete Samples

Discrete samples from the approximate location of NH-10 were collected and analyzed for pCO_2 and DIC in the Burke Hales laboratory at Oregon State University using a method modified from that described by *Bandstra et al.* [2006]. From pCO_2 and DIC, the other carbonate system parameters could be calculated in CO2SYS. These values from the sample could then be compared to pH and pCO_2 data recorded by the SAMIs at NH-10 during the same time periods the discrete samples were collected. If discrete samples were taken at the same time and from the same water mass located at NH-10, then the SAMI and discrete sample carbonate system parameter values should match.

The discrete sample carbonate system parameters are reported in Table 3.3.2. SAMI-CO_2 values were within 1-13 µatm (n = 4) from discrete sample values and SAMI-pH measurements were within 0.003-0.04 (n = 4) from pH values calculated in CO2SYS for the discrete sample values (Table 3.3.2). DIC and A_T differences ranged between 5 to 142 µmol kg^{-1} and between 15 to 110 µmol kg^{-1}(Table 3.3.2), respectively. Ω_{Ca} and Ω_{Ar} calculated in CO2SYS from SAMI data differed by0.15 to 0.52 and 0.14 to 0.52 (n = 4), respectively, from those calculated from sample data (Table 3.3.2). The largest differences in DIC, A_T, Ω_{Ca}, and Ω_{Ar} correspond to the sample with a large pH difference of 0.04 and large pCO_2 difference of 13 µatm, suggesting that this sample was retrieved from a water mass not representative of the one being sampled by the SAMIs at that specific time.

Table 3.3.2. Discrete samples from NH-10 compared to SAMI data. Temperature (T) is in °C, pCO_2 is in µatm, A_T and DIC are in µmol kg^{-1}. Salinity (S), pH, and Ω are unitless. *Indicates CO2SYS-calculated values.

Discrete Samples								
Date	**T**	**S**	**pH***	**pCO_2**	**A_T***	**DIC**	**Ω_{Ca}***	**Ω_{Ar}***
5/4/11 21:00	11.86	29.37	8.163	277.5	2096	1923	3.58	2.25
5/4/11 21:00	11.84	29.36	8.172	270.0	2089	1912	3.63	2.28
6/9/11 20:57	13.37	29.60	8.189	281.0	2275	2030	4.32	2.73
7/13/11 23:00	14.20	30.16	8.186	292.8	2362	2102	4.62	2.93
SAMI								
Date	**T**	**S**	**pH**	**pCO_2**	**A_T***	**DIC***	**Ω_{Ca}***	**Ω_{Ar}***
5/4/11 21:00	10.68	29.70	8.169	270.3	2085	1886	3.48	2.19
5/4/11 21:00	10.68	29.70	8.169	270.3	2085	1886	3.48	2.19
6/9/11 21:00	13.94	28.94	8.151	293.7	2132	1920	3.79	2.39
7/13/11 23:00	16.50	28.18	8.194	295.8	2384	2118	4.96	3.21
Difference (Discrete - SAMI)								
Date	**T**	**S**	**pH**	**pCO_2**	**A_T***	**DIC***	**Ω_{Ca}***	**Ω_{Ar}***
5/4/11 21:00	1.18	-0.33	-0.006	7.2	11	37	0.10	0.06
5/4/11 21:00	1.16	-0.34	0.003	-0.3	5	26	0.15	0.09
6/9/11 21:00	-0.57	0.66	0.038	-12.7	142	110	0.52	0.33
7/13/11 23:00	-2.30	1.98	-0.008	-3.0	-22	-15	-0.34	-0.28
Average	**-0.13**	**0.49**	**0.007**	**-2.2**	**34**	**39**	**0.11**	**0.05**

3.3.3. Tris Comparison

During the spring and summer of 2011, a SAMI^2-pH with a tris CRM (salinity = 35) was deployed at NH-10. The SAMI measured seawater pH every three hours and a tris CRM sample once every five days. The tris pH is compared to the calculated tris value (using the temperature and salinity-dependent equation for tris buffer found by *DelValls and Dickson* [1998]) in Figure 3.3.1. In addition, a pH correction was applied to the SAMI-pH data to correct for impurities in

the SAMI-pH indicator, mCP (discussed below).

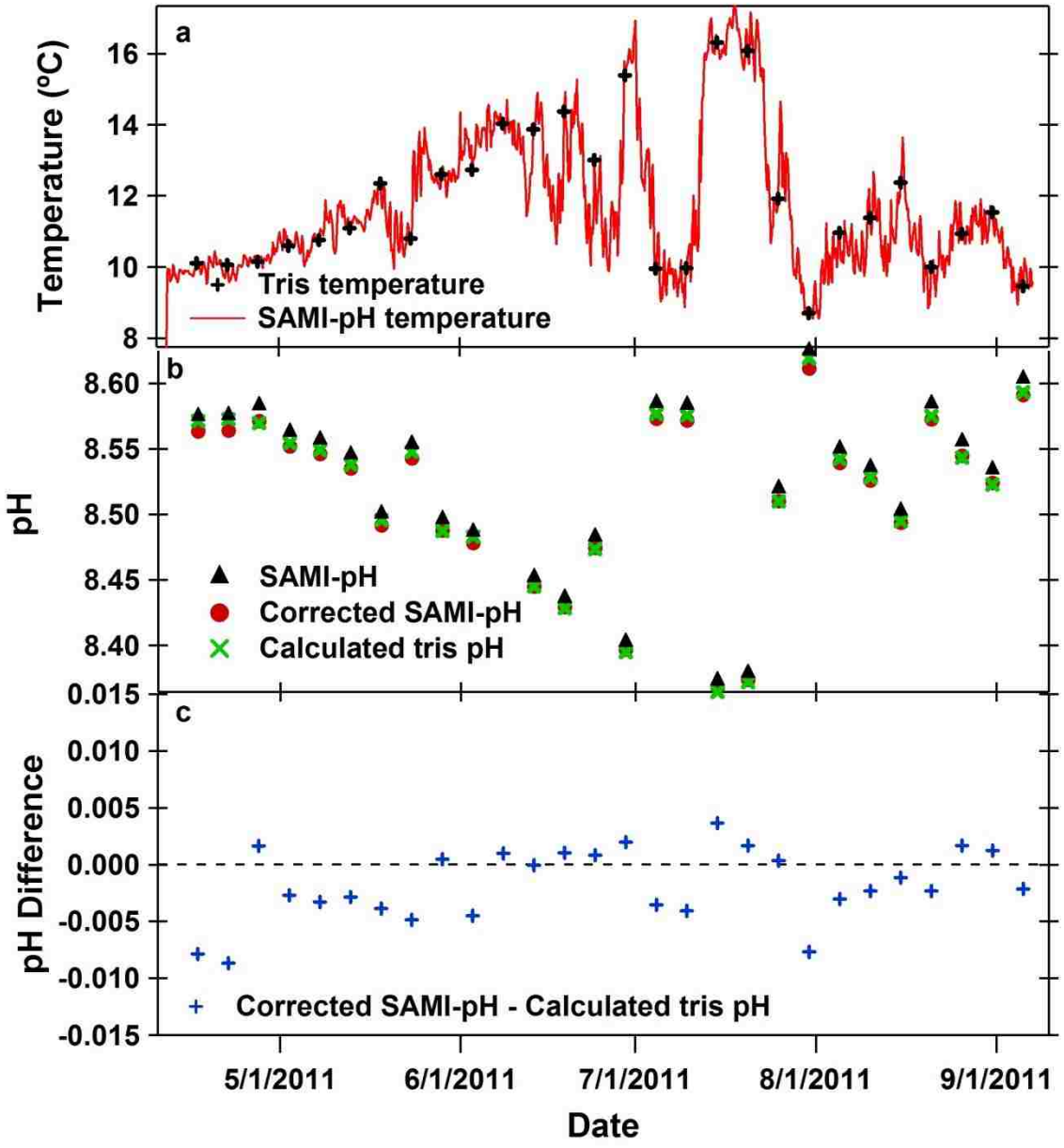

Figure 3.3.1. Comparisons between SAMI tris pH and calculated tris pH during the spring/summer 2011 deployment. (a) Temperature of the tris measurement and sea surface temperature as measured by the SAMI-pH. (b) Tris pH as measured by the SAMI-pH (black triangles), the SAMI-pH with the mCP correction applied (red circles), and as calculated using temperature values (green x's). (c) The difference between SAMI-pH measured tris (with the mCP correction) and calculated tris.

The calculated tris pH (green crosses, Figure 3.3.1) was always closer to the corrected SAMI measurement of tris pH (red circles, Figure 3.3.1) than the uncorrected SAMI measurements of tris pH (black triangles, Figure 3.3.1). The error between the corrected measured tris pH and calculated tris pH is small, with an average error of 0.0017 pH units; this is less than the commercially-stated accuracy of the instrument (±0.003). The plot of the error between calculated and corrected measured tris (Figure 3.3.1c) showed no identifiable drift over time. In addition, the pH error showed little correlation with temperature and the previously measured pH (R^2=0.15, p-value>0.01, n=28), indicating that errors between the measured tris pH and calculated tris pH are random.

In their research into the impurities between different batches of mCP [*Liu et al.*, 2011] determined that previous pH measurements using unpurified mCP pH indicator could be corrected by applying a pH offset to the data. The pH offset was determined in our lab using an unpurified mCP indicator solution to measure pH values of a seawater certified reference material (tris in synthetic seawater, [*DelValls and Dickson,* 1998]) on the Cary 300 and comparing them to the calculated value based on salinity and temperature [*Delvalls and Dickson*, 1998] (Figure 3.3.2). Using this method, Emma Jaqueth (undergraduate researcher in the DeGrandpre Lab) determined the indicator impurity correction for mCP batch #11517KC (mCP sodium salt from Sigma-Aldrich) to be:

$$pH_{corr} = pH_{meas} - (0.022228 \cdot pH_{meas}^2 - 0.034575 \cdot pH_{meas} + 1.322984) \quad (3.6)$$

where pH_{corr} is the pH>8.0 corrected for mCP impurities and pH_{meas} is the SAMI-pH. This correction was applied to all SAMI-pH field data (see Table 3.3.1). The average difference between pH_{corr} and pH_{meas} for field data on the Oregon Coast was ±0.0036.

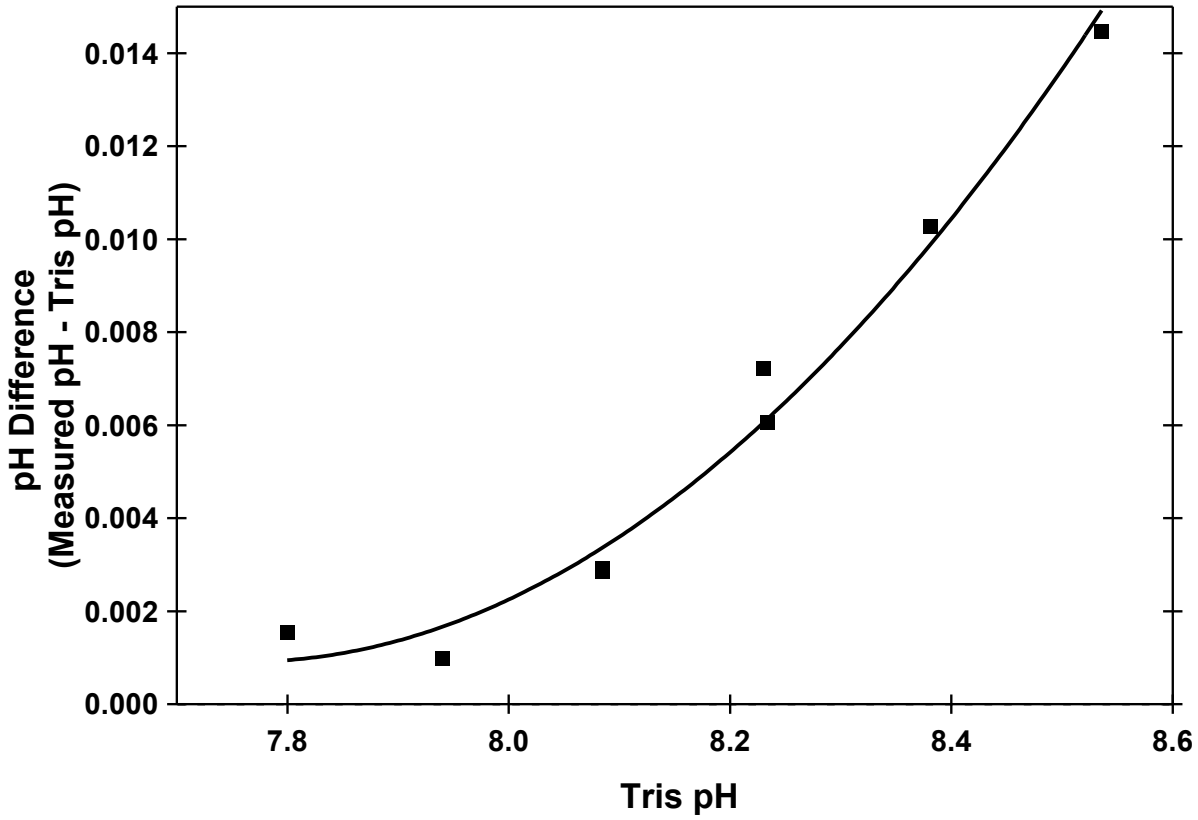

Figure 3.3.2. The pH difference between calculated tris pH [*Delvalls and Dickson*, 1998] and the tris pH determined by E. Jaqueth on the Cary 300 using reagent made from Sigma-Aldrich mCP batch #11517KC. Two bottles of standardized tris buffer were tested (prepared by Andrew Dickson at Scripps Institute of Oceanography).

Figure 3.3.3 shows the pH correction for mCP impurities applied to SAMI-pH field data for spring and summer 2011. Higher measured pH values required a larger correction for the impurities. The pH corrections at measured pH-values above 8.3 approached 0.008 (Figure 3.3.3b), more than two times the stated accuracy of the instrument. This large difference due to dye impurities at high pH indicates that pH correction for dye impurities is especially important for seawater measurements in locations that experience large changes in pH over time.

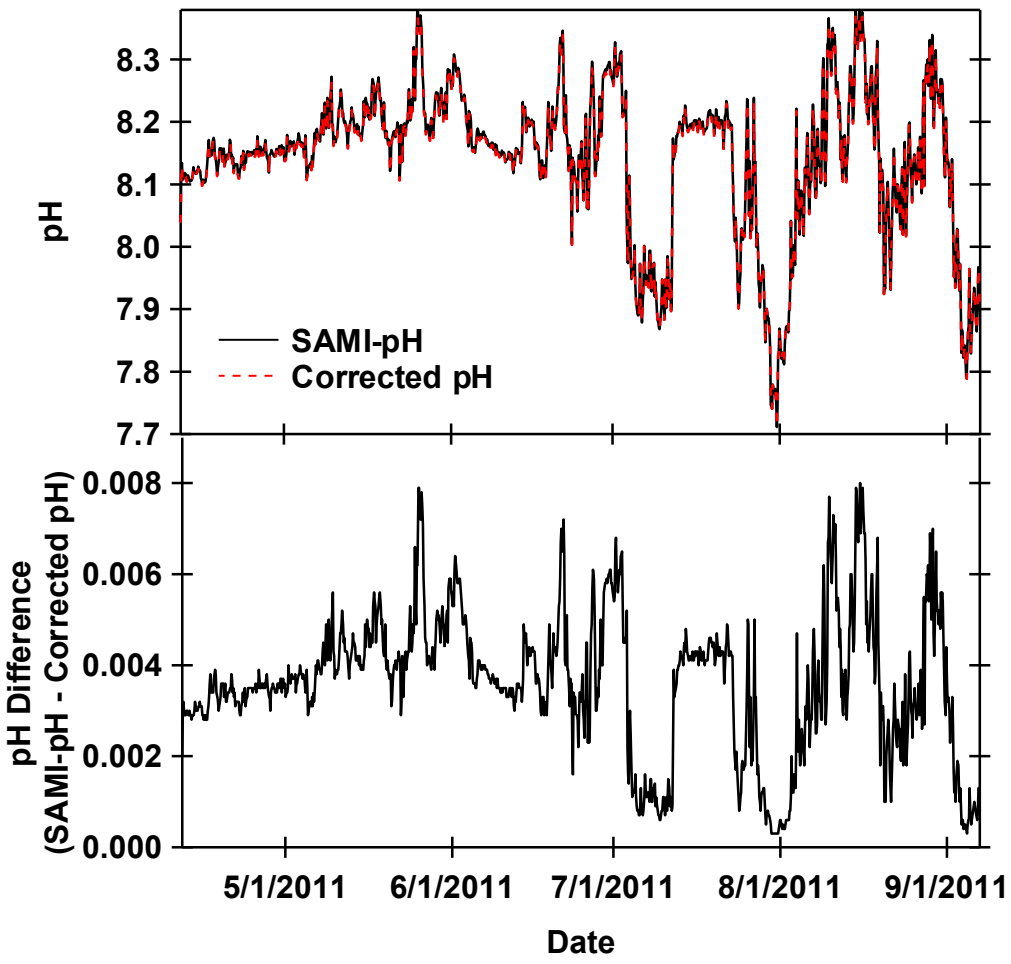

Figure 3.3.3. (a) SAMI-pH correction applied to SAMI-pH field data from 2011 measured at the NH-10 mooring. (b) Difference between measured pH and corrected pH (measured minus corrected).

3.3.4. Paired SAMI-CO_2 and SAMI-pH Calculations

As described by *Gray et al.* [2011], deploying SAMI-pH and SAMI-CO_2 instruments at the same location allows for in situ quality control. Because any two carbonate parameters can be used to calculate the rest of the parameters in the carbonate system, SAMI-pH and SAMI-CO_2 data can be used together as inputs with T, S, and P data to calculate the other carbonate system parameters in CO2SYS or separately with alkalinity derived from a conservative salinity-alkalinity relationship (A_{Tsalin}) for that location. *Millero* [1995] and *Gray et al.* [2011] discuss

the accuracy errors in calculated carbonate system parameters using the six possible combinations of input parameters (pH-A_T, pH-DIC, pH-pCO_2, pCO_2-DIC, pCO_2-A_T, and A_T-DIC). Of these combinations, the pH-pCO_2 combination gives significantly larger imprecision due to the proportional relationship between pH and pCO_2. The pH-A_T and pCO_2-A_T combinations result in smaller errors [*Millero*, 1995]. Although the pH-pCO_2 combination resulted in very large DIC errors, *Gray et al.* [2011] found that this combination could be used to accurately calculate $[CO_3^{2-}]$ and Ω. The parameters calculated by these three pairs (pH-pCO_2, pCO_2-A_T, and pH-A_T) can be compared to validate the SAMI datasets. First, however, the appropriate A_{Tsalin} relationship for the field site had to be determined.

3.3.4.1. Salinity-Alkalinity Relationships

The relationship between S and A_T changes based on location, due to differences the extent of deep waters outcropping at the surface [*Millero et al.*, 1998] and freshwater end-members in coastal areas . We compared three salinity-alkalinity relationships– the salinity-alkalinity relationship for the Pacific derived by [*Millero et al.*, 1998]:

$$A_{Tsalin} = 520.1 + 51.24 * S \quad (3.7)$$

one derived from alkalinity and salinity data from the 2007 NACP West Coast Cruise (Carbon Dioxide Information Analysis Center (CDIAC, cdiac.ornl.gov)):

$$A_{Tsalin} = 461.5 + 52.86 * S \quad (3.8)$$

and one derived for California coastal waters [*Gray et al.*, 2011]:

$$A_{Tsalin} = 543.5 + 50.8 * S \quad (3.9)$$

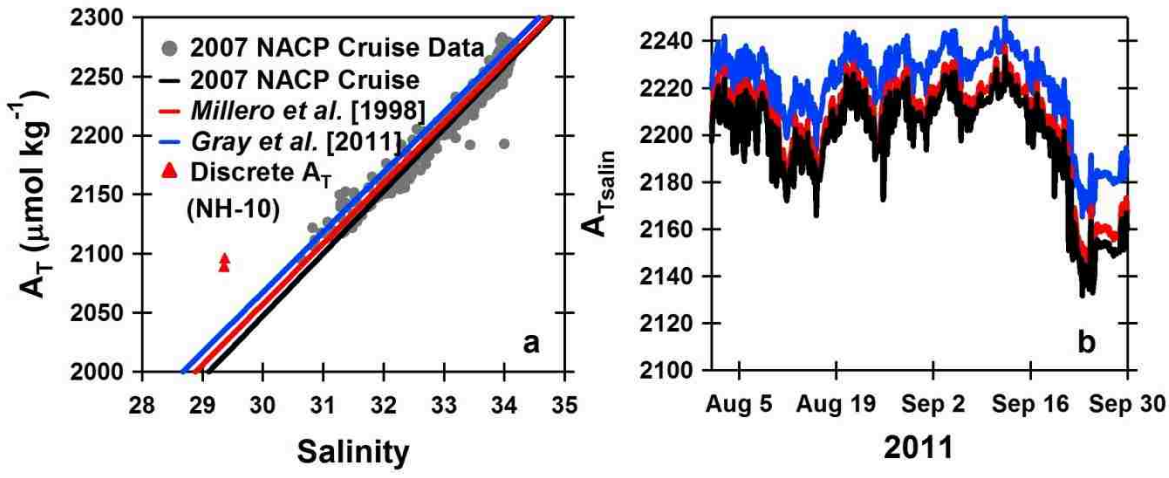

Figure 3.3.4. Comparison between alkalinity-salinity relationships for the North Pacific and discrete sample A_T from NH-10 (a). Each alkalinity-salinity relationship applied to salinity field data from NH-10 during summer 2011 (b). Note the scale change between the two figures.

The three relationships are shown in Figure 3.3.4. The three relationships produce alkalinities within 25 µmol kg^{-1} seawater at low salinity (~27) and within 13 µmol kg^{-1} seawater at high salinity (34) of each other. This corresponds to aragonite saturation state calculations within 0.07 at low salinity and 0.01 at high salinity. The A_T calculated for the discrete water samples from NH-10 in 2011 best matched the relationship derived by *Gray et al.* [2011], with the A_{Tsalin} calculated from this relationship differing between 3-11% from the discrete A_T (the other relationships differed between 4-13%). In addition, when SAMI-pH and SAMI-CO_2 data were both available, A_T could be calculated in CO2SYS using pH and pCO_2 as input parameters. These A_T values were noisy due to the propagation of errors when using those two input parameters (see *Millero* [2007]; *Cullison* [2010]; *Gray et al.* [2011]), but the baseline of these values was closest to the *Gray et al.* [2011] A_{Tsalin} relationship (Equation 3.9). The average A_{Tsalin} from the *Gray et al.* [2011] relationship was on average 20% closer to A_T from pH/pCO_2 than the A_{Tsalin} from the *Millero et al.* [1998] relationship and 33% closer than the A_{Tsalin} from the NACP (2007) relationship. Thus the *Gray et al.* [2011] relationship was used.

3.3.4.2. Data Validation Using Paired SAMI-pH and SAMI-CO_2

Out of five years of SAMI deployments at NH-10, there were three SAMI deployments during which both SAMI-pH and SAMI-CO_2 instruments successfully recorded data, one in the spring of 2009, one in the autumn of 2009, and one during the spring/summer of 2011 (see Table 3.3.1). For each deployment when both pH and pCO_2 were collected data comparisons between SAMI-collected data and CO2SYS-calculations (i.e. pCO_2 from pH-A_{Tsalin} or pH from pCO_2-A_{Tsalin}) were made (Figures 3.3.5-3.3.7). Ω_{Ar} was also calculated in CO2SYS using three different pairs of carbonate parameters: pCO_2-A_{Tsalin}, pH-A_{Tsalin}, and pH-CO_2 for each of these three deployments.

The pCO_2-A_{Tsalin} and pH-A_{Tsalin} calculations follow the SAMI data remarkably well considering the A_{Tsalin} relationship used was determined for California coastal waters. The differences between SAMI data and A_{Tsalin}-calculated data are reported in Table 3.3.3. Differences for pH (0.01-0.02) and pCO_2 (2-11 µatm) are remarkably small, especially for the length of time the instruments were measuring (>2 months). The changes in the inorganic carbonate system measured by each instrument track well, even during rapid (<2 days) pH changes of up to 0.2 and pCO_2 changes up to 200 µatm.

Table 3.3.3. The differences between calculated and measured pH and pCO_2 and the three methods of calculating Ω_{Ar}.

Deployment	n	pH[b]	pCO_2[c] (µatm)	Ω_{Ar}[d]	Ω_{Ar}[e]	Ω_{Ar}[f]
Spring 09[a]	1464	0.01±0.01	7±8	-0.06±0.08	-0.09±0.13	0.04±0.05
Autumn 09[a]	1151	0.01±0.03	2±18	-0.07±0.23	-0.10±0.36	0.03±0.13
Summer 11[a]	1698	0.02±0.01	11±10	-0.10±0.09	-0.16±0.14	0.09±0.06

[a]Average difference ± standard deviation

[b]$pH_{ATsalin\text{-}pCO2}$ minus measured pH [c]$pCO2_{ATsalin\text{-}pH}$ minus measured pCO_2 [d]$\Omega_{pH\text{-}ATsalin}$ minus $\Omega_{pH\text{-}pCO2}$ [e]$\Omega_{pCO2\text{-}ATsalin}$ minus $\Omega_{pH\text{-}pCO2}$ [f]$\Omega_{pH\text{-}ATsalin}$ minus $\Omega_{pCO2\text{-}ATsalin}$

The large differences between SAMI-pH or pCO_2 data and their calculated values at the end of the deployments in spring of 2009 and summer of 2011 are likely due to biofouling of one or both of the SAMIs. The effect of biofouling is most evident in the large diel changes in the SAMI-CO_2 data starting in mid-June of 2011 (Figure 3.3.7) that are not matched in intensity in the SAMI-pH data. For this reason, SAMI-CO_2 data after June 12, 2011, was discarded. At the end of autumn 2009, a battery issue in the SAMI-pH led to reagent pumping issues which caused an offset and drops in the pH data (see Figure 3.3.6). Due to these inaccuracies, pH data was discarded after November 17, 2009 for that deployment. There is another large offset between the SAMI-pH and SAMI-CO_2 data during September, 2009 (Figure 3.3.6).

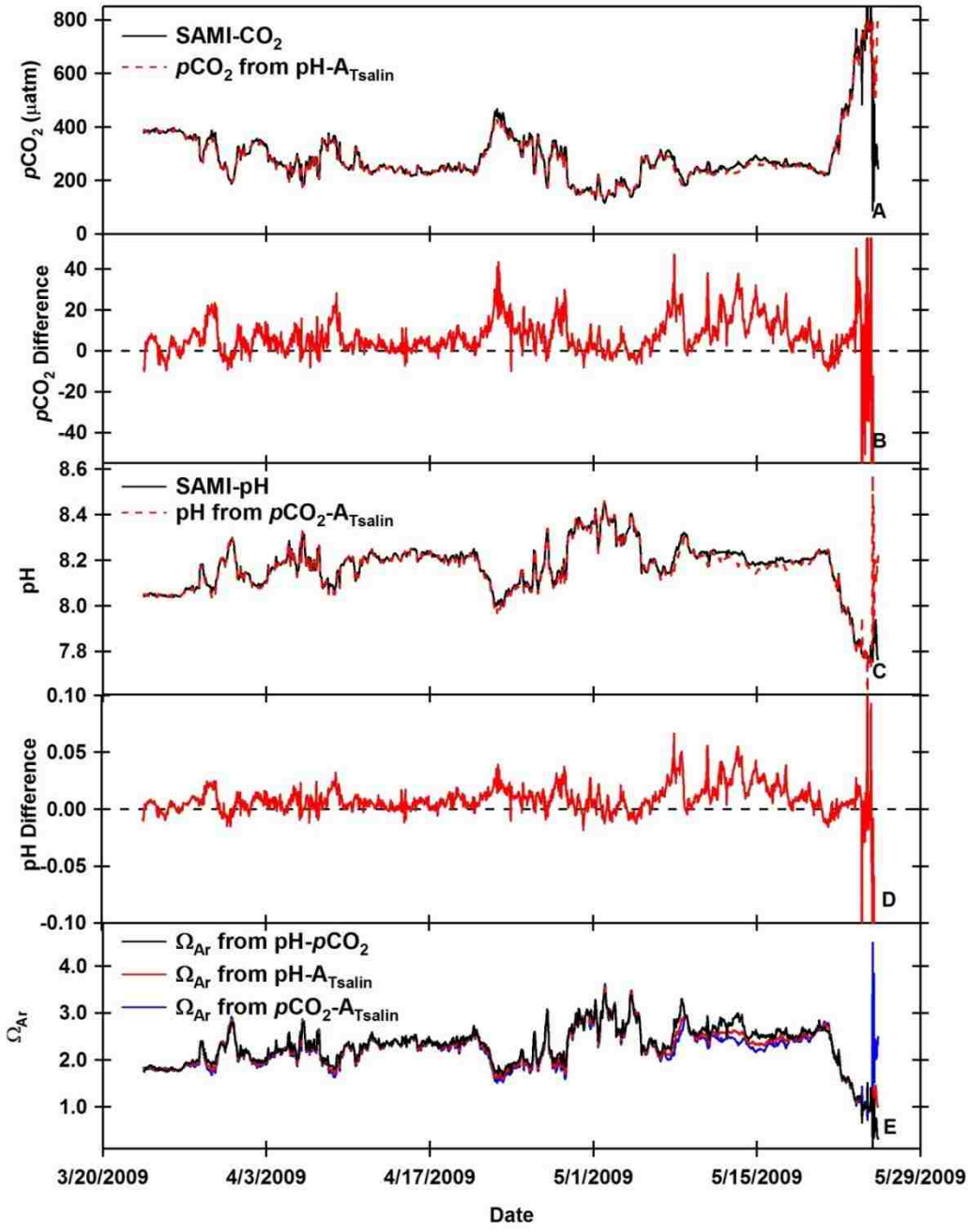

Figure 3.3.5. Quality assurance for the spring 2009 NH-10 deployment. (a)SAMI-CO_2 and pCO_2 from pH-A_{Tsalin}. (b) Measured pCO_2 minus pCO_2 from pH-A_{Tsalin}. (c) SAMI-pH and pH from pCO_2-A_{Tsalin}. (d) Measured pH minus pH from pCO_2-A_{Tsalin}. Ω_{Ar} from each calculation combination (pH-pCO_2, pH-A_{Tsalin}, and pCO_2-A_{Tsalin}). Differences between Ω_{Ar} calculations can be found in Figure 3.3.12. The average differences are reported in Table 3.3.4).

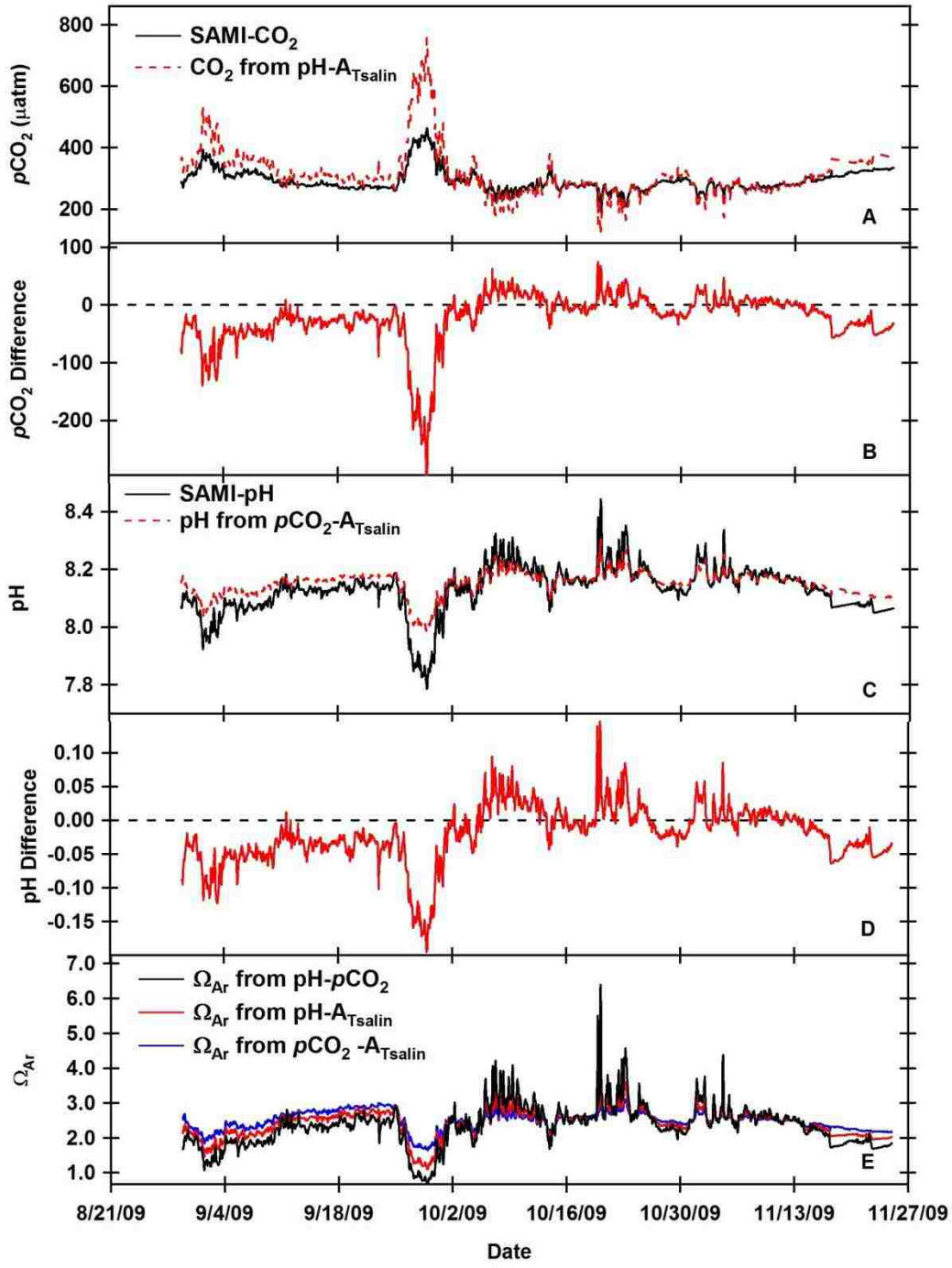

Figure 3.3.6. Quality assurance for the autumn 2009 NH-10 deployment. (a)SAMI-CO_2 and pCO_2 from pH-A_{Tsalin}. (b) Measured pCO_2 minus pCO_2 from pH-A_{Tsalin}. (c) SAMI-pH and pH from pCO_2-A_{Tsalin}. (d) Measured pH minus pH from pCO_2-A_{Tsalin}. Ω_{Ar} from each calculation combination (pH-pCO_2, pH-A_{Tsalin}, and pCO_2-A_{Tsalin}). Differences between Ω_{Ar} calculations can be found in Figure 3.3.12. The average differences are reported in Table 3.3.4).

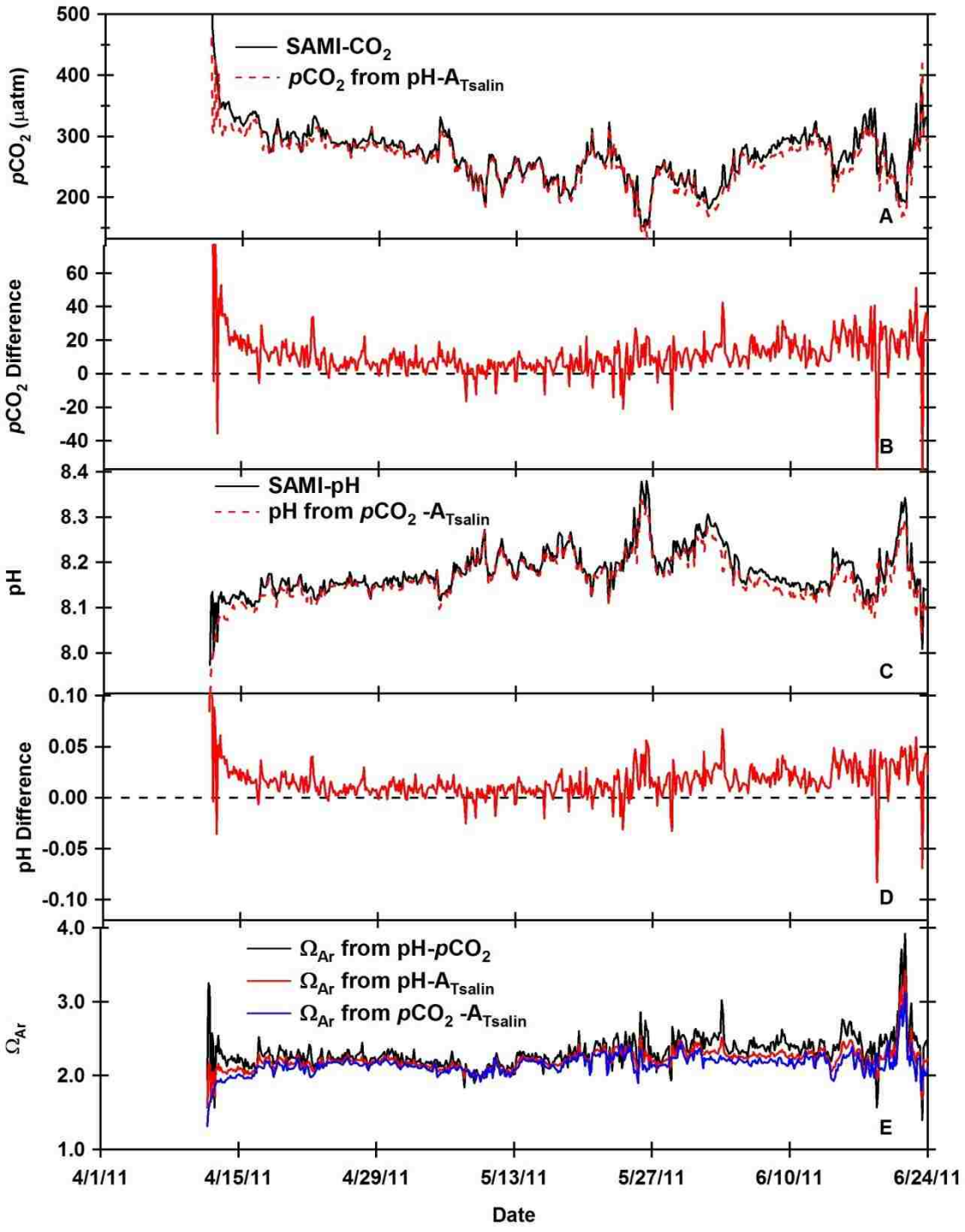

Figure 3.3.7. Quality assurance for the spring 2011 NH-10 deployment. (a)SAMI-CO_2 and pCO_2 from pH-A_{Tsalin}. (b) Measured pCO_2 minus pCO_2 from pH-A_{Tsalin}. (c) SAMI-pH and pH from pCO_2-A_{Tsalin}. (d) Measured pH minus pH from pCO_2-A_{Tsalin}. Ω_{Ar} from each calculation combination (pH-pCO_2, pH-A_{Tsalin}, and pCO_2-A_{Tsalin}). Differences between Ω_{Ar} calculations can be found in Figure 3.3.12. The average differences are reported in Table 3.3.3).

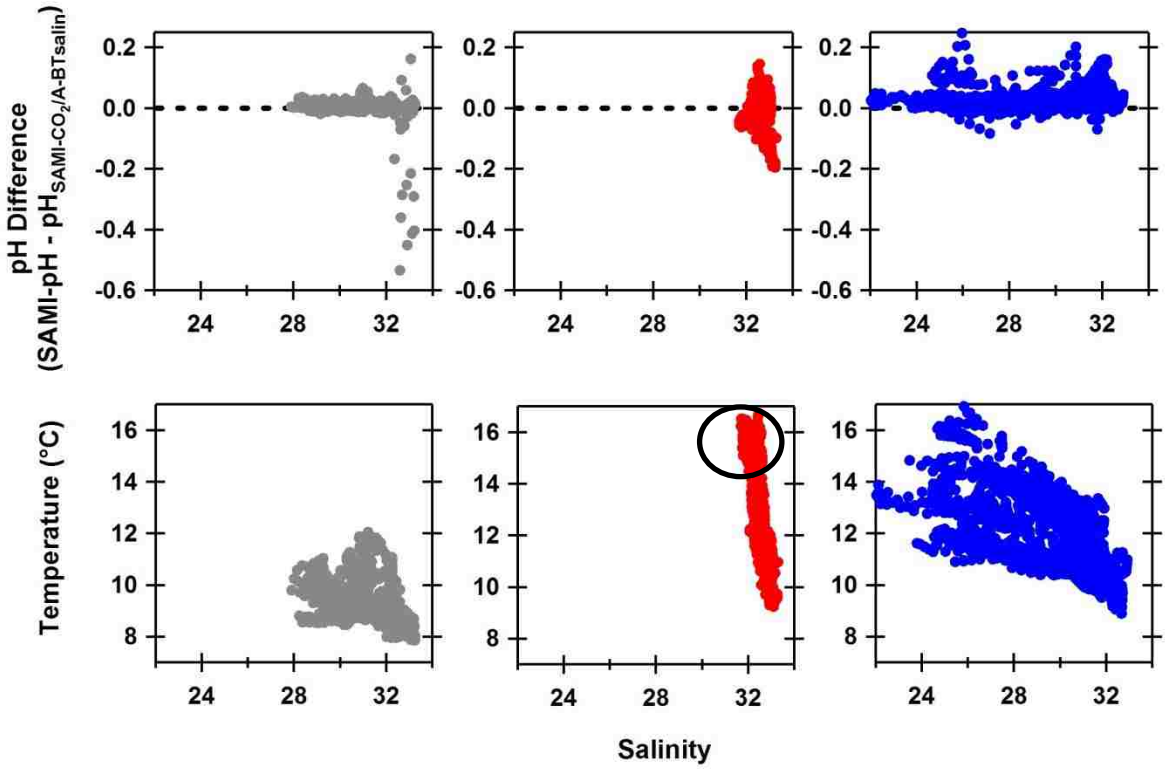

Figure 3.3.8. (a-c) Difference in SAMI and calculated pH compared to salinity for (a) spring 2009 (see Figure 3.3.5), (b) autumn 2009 (see Figure 3.3.6), and (c) spring 2011(see Figure 3.3.7) deployments at NH-10. (d-f) Temperature-salinity relationships for Oregon shelf water during the three deployments. The circle in (e) highlights the unusually high T and S water mass. The cause of this is uncertain, especially since it appears to go away starting October 1, 2009. It is possible that the NH-10 site was host to a water mass with a different salinity-alkalinity – relationships, resulting in inaccurate CO2SYS calculations of both pCO_2 and pH.

Figure 3.3.8 shows the difference between observed and calculated pH for each of the three paired-SAMI deployments as well as the T-S relationships during each time. The T-S relationship is a good proxy for the water mass since different water masses will have a different T-S relationship based on where they were formed [i.e. *Mamayev,* 1975]. The water present at NH-10 during September 2009 was unusually high in both T and S compared to the water present during spring 2009 and 2011 or later in the autumn of 2009 (see circle, Figure 3.3.8e)

and is open ocean North Pacific water [*Venegas et al.*, 2008]. A different salinity-alkalinity relationship for this water mass would explain the mis-match between the measured and calculated pH and pCO_2 data during this time. Replacement by a lower T, higher S water mass in October with a salinity-alkalinity relationship closer to that used by [*Gray et al.*, 2011] results in the closer match between measured and calculated parameters during this time. For these reasons, the data during September 2009 was discarded.

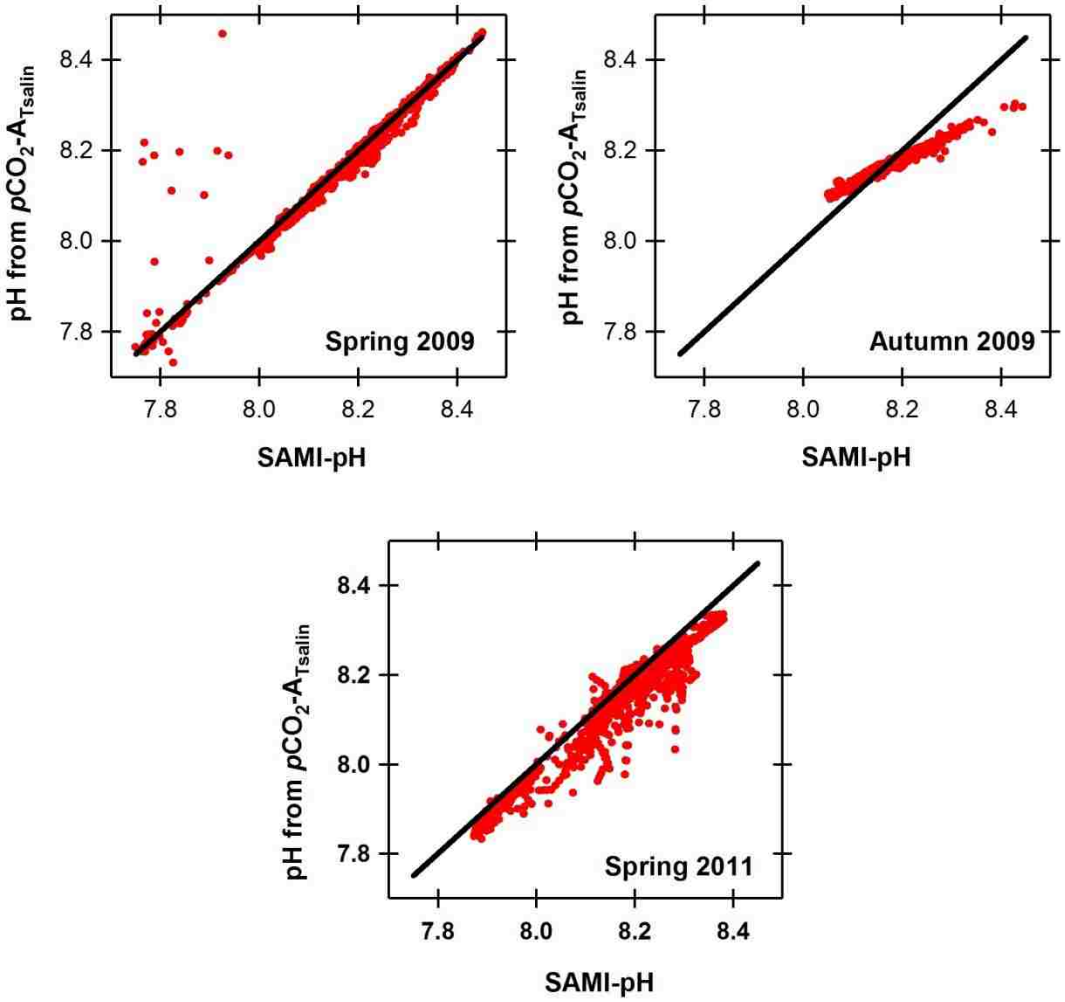

Figure 3.3.9. pH calculated from pCO_2-A_{Tsalin} vs. SAMI-pH for deployments during spring 2009 (see Figure 3.3.5), autumn 2009 (see Figure 3.3.6), and spring 2011 (see Figure 3.3.7). The black line is a 1-to-1 line.

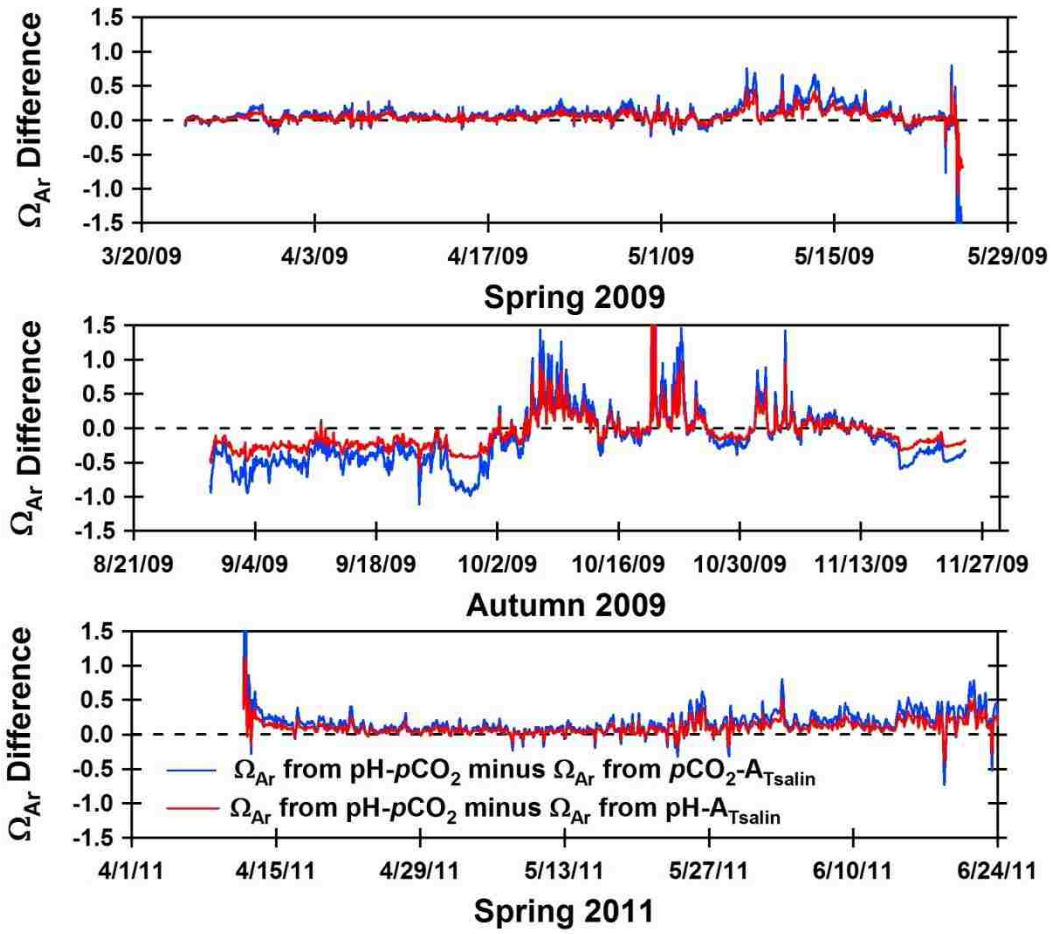

Figure 3.3.10. Differences (Ω_{Ar} from pH-pCO_2 minus Ω_{Ar} from A_{Tsalin}) between the combinations of parameters used to calculate Ω_{Ar}. The average differences can be found in Table 3.3.3.

The average SAMI reproducibility (i.e., the differences between the SAMI-measured and CO2SYS-calculated parameters) was calculated for each of the three paired-SAMI deployments after discarding the above data. These values can be found in Table 3.3.3. Summer 2011 had the largest differences for all parameters. *Gray et al.* [2011] reported that rapid changes in pH and pCO_2 result in large spikes in the calculated parameters. These breakdowns in correlation between SAMI-pH and SAMI-CO_2 data can result from spatial and sample timing mis-matches between the two instruments. Figures 3.3.5-3.3.7 show that the largest differences between the

measured and calculated parameters frequently occur during rapid changes in the carbonate system. The paired-SAMI deployment during 2011 was the only paired-deployment that took place fully during the summer upwelling season when large changes in the carbonate system over short periods of time are expected. This variability likely resulted in the larger differences for 2011 reported in Table 3.3.3.

In order to determine whether there were systematic offsets between the SAMI-pH and the SAMI-CO_2, measured pH was plotted against calculated pH (Figure 3.3.9), measured pCO_2 was plotted against calculated pCO_2 (figure not shown), and Ω_{Ar} from pH-pCO_2 was plotted against Ω_{Ar} from pH-A_{Tsalin} (Figures 3.3.10 and 3.3.11). Figure 3.3.9 shows the results from comparing SAMI-pH to pH from pCO_2-A_{Tsalin}. Spring 2009 follows the 1 to 1 line pretty closely. During the autumn of 2009, there are significant differences between the SAMI data and the calculated pH. At lower pH values, the calculated pH is higher than the measured pH data while at higher values the calculated pH is significantly lower than the measured pH. SAMI-pH data was plotted against SAMI-CO_2 data for each of the three deployments (Figure 3.3.13). The data from autumn 2009 (Figure 3.3.9b) result in an almost linear relationship, deviating from the expected non-linear relationship observed during spring 2009 and spring 2011, suggesting that measurements from one or both sensors were inaccurate. Spring 2011 (Figure 3.3.9c) also shows significant deviations from the 1 to 1 line. Figure 3.3.9c shows that the SAMI-CO_2 and A_{Tsalin} combination consistently calculates a lower pH than that measured by the SAMI-pH, again suggesting that one or both sensors may be inaccurate or the salinity-alkalinity relationship deviates from the one in Equation 3.9. It is not possible to determine which sensor was inaccurate and so the data from this period were not used. The relationships between calculated and measured pCO_2 during the

three deployments are very similar to those shown for pH (Figure 3.3.9) and thus are not shown here.

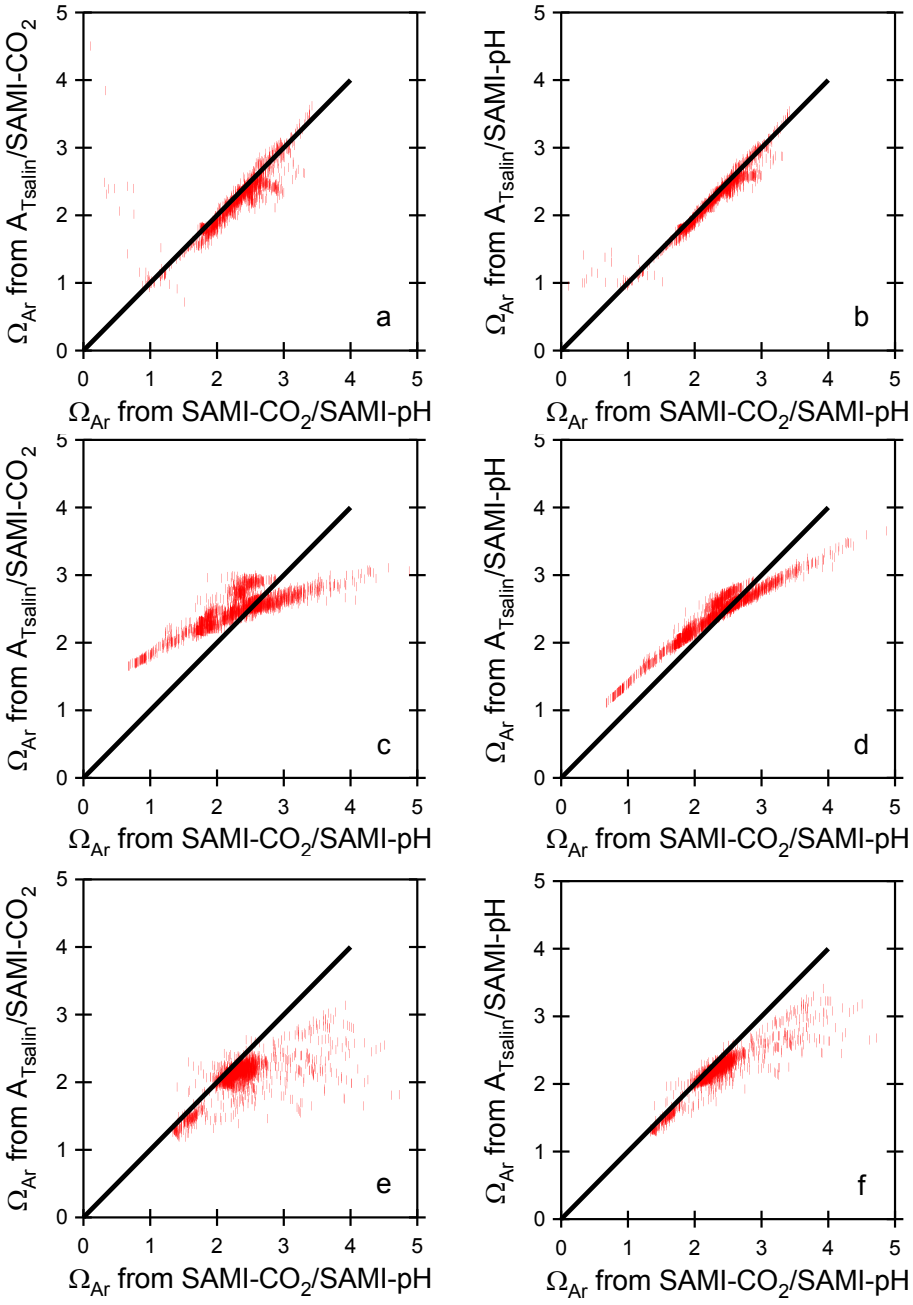

Figure 3.3.11. Ω_{Ar} calculated from each of the three deployments when both pH and pCO_2 data were collected. Ω_{ar} from A_{Tsalin}/SAMI-CO_2 vs. Ω_{ar} from SAMI-CO_2/SAMI-pH for (a) spring 2009, (c) autumn 2009, (d) spring/summer 2011. Ω_{ar} from A_{Tsalin}/SAMI-pH vs. Ω_{ar} from SAMI-CO_2/SAMI-pH for (b) spring 2009, (d) autumn 2009, and (f) spring/summer 2011.

As explained in the Introduction (section 1.1), Ω_{Ar} is mechanistically lower than Ω_{Ca}. For this reason and because of the importance of Ω_{Ar} for the larval stages of *Crassostrea gigas* (an economically-important calcifying organism on the coast) characterization of Ω_{Ar} dynamics was the focus of this field study. In addition, Ω_{Ar} is often the main focus in ocean acidification research because it is as a bellwether of the potential impacts of ocean acidification. Ω_{Ca} was assumed to have similar dynamic but a higher saturation state. The two different methods of calculating Ω_{Ar} from A_{Tsalin} are compared to Ω_{Ar} calculated from pH-pCO_2 in Figures 3.3.10 and 3.3.11. The SAMI-pH and SAMI-CO_2 combination results in lower calculated Ω_{Ar} values than either of the A_{Tsalin} combinations. These greater offsets are also evident in Table 3.3.3, with the differences for Ω_{Ar} calculated from SAMI-pH and SAMI-CO_2 relatively greater than those calculated using A_{Tsalin}.

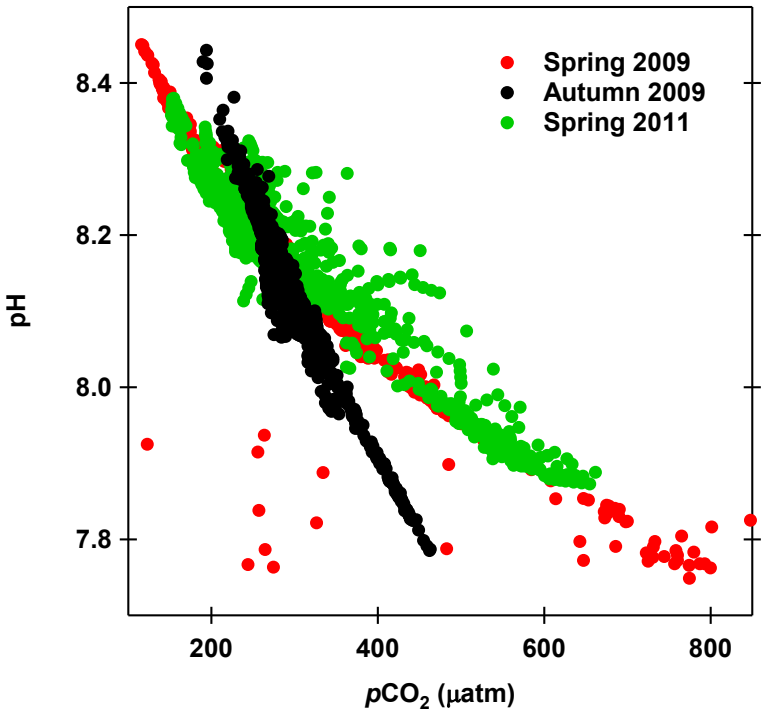

Figure 3.3.12. SAMI-pH vs. SAMI-CO_2 for deployments during spring 2009 (red), autumn 2009 (black) and spring 2011 (green).

Although *Gray et al.* [2011] had determined that the pH-pCO_2 combination could be used to accurately calculate Ω_{Ar}, these datasets show that combination can result in large offsets in Ω_{Ar}. Thus this combination for calculating Ω_{Ar} should be used with caution. The comparisons in Figures 3.3.4-3.3.7 show that (with the exception of September 2009) the salinity-alkalinity relationship from Equation 3.9 holds for the field site and the Ω_{Ar} derived from A_{Tsalin} and either pH or pCO_2 were always somewhat closer than Ω_{Ar} derived from SAMI-pH and SAMI-CO_2 (Table 3.3.3). Therefore, the Ω_{Ar} values (and the other calculated-carbonate parameters) reported here were obtained by averaging the values at each measurement time derived from pCO_2- A_{Tsalin} and pH-A_{Tsalin}. Table 3.3.4 gives a detailed description of which input parameters were used at each time during all deployments.

Table 3.3.4. Deployment Dates and Ω_{Ar} Calculation Methods

Date	**SAMI data available**	**Ω_{Ar} Calculation Method**
8/16/07-10/12/07	pCO_2	A_{Tsalin} and pCO_2
10/19/07-11/6/07	pCO_2	A_{Tsalin} and pCO_2
4/10/08-9/7/08	pCO_2	A_{Tsalin} and pCO_2
3/23/09-5/25/09	pH and pCO_2	Average[a]
10/1/09-11/17/09	pH and pCO_2	Average[a]
11/18/09-4/15/10	pCO_2	A_{Tsalin} and pCO_2
10/19/10-11/29/10	pCO_2	A_{Tsalin} and pCO_2
4/11/11-6/21/11	pH and pCO_2	Average[a]
6/22/11-9/6/11	pH	A_{Tsalin} and pH

[a]Average of Ω_{Ar} calculated from pH-A_{Tsalin} and Ω_{Ar} calculated from pCO_2-A_{Tsalin} at each sample time.

3.4. Aragonite saturation state Dynamics in the Oregon Coastal Upwelling Zone

What follows is a paper adapted from the one published by K. Harris in Geophysical Research Letters in 2013 [Harris et al., 2013*].*

3.4.1. Introduction

The oceanic uptake of anthropogenic CO_2 and the resultant ocean acidification have been well-documented [*Haugan and Drange*, 1996; *Caldeira and Wickett*, 2003; *Feely et al.*, 2008; *Dore et al.*, 2009; *Midorikawa et al.*, 2012] Moorings such as the Bermuda Atlantic Time-series (BATs) and the Hawaii Ocean Time-series, the Hawaii Ocean Time-series (HOT) and Station Papa in the North Pacific have resulted in datasets describing long-term trends in the carbonate system, but their low sampling frequency (~once a month) miss short-term dynamics. Coastal margins, especially coastal upwelling regions, are harder to study on these lower sampling frequencies due to their high short-term carbonate system variability.

Coastal upwelling zones are highly productive regions [*Friederich et al.*, 2008; *Chavez and Messié*, 2009] [*Boehme et al,* 1998] due to the influx of nutrients that accompanies the low-pH, low-Ω, and high-pCO_2 of upwelled waters. To better understand how changes in the carbonate system due to ocean acidification will affect these regions, a better characterization of the current variation in the coastal upwelling carbonate system is necessary. As stated earlier, autonomous sensors with higher sampling frequencies such as the SAMI-pH and SAMI-CO_2 make possible the calculation and characterization of the daily, seasonal, and annual variation of highly dynamic regions like the Oregon shelf.

The Oregon coastal upwelling zone is particularly susceptible to changes in the ocean carbonate system due to ocean acidification due to the influx of naturally low-Ω_{Ar} waters due to upwelling. Ocean acidification lowers Ω_{Ar} in upwelled waters even further, sometimes to below saturation.

Previous studies of the region recorded several events in which nearby surface waters reached aragonite undersaturation for short periods of time [*Feely et al.*, 2008; *Barton et al.*, 2012]. However, the frequency and duration of these events has not been well-characterized.

As a follow-up to the air-sea CO_2 flux time-series study by *Evans et al.* [2011], we present long-term time-series of Ω_{Ar} values in the Oregon coastal upwelling zone. Additionally, we use high temporal resolution data to examine the processes controlling short-term changes in Ω_{Ar} and compare the current Ω_{Ar} range to the estimated pre-industrial Ω_{Ar} range.

3.4.2. Calculations

Three mechanisms were assumed to control Ω_{Ar} changes on the Oregon shelf. Phytoplankton productivity in the photic zone will result in a change in Ω_{Ar} by decreasing pCO_2 as the phytoplankton take up CO_2 during photosynthesis. Air-sea CO_2 gas exchange will lead to a seawater pCO_2 increase or decrease and result in DIC and Ω_{Ar} changes. Mixing with the Columbia River (CR) plume or upwelled water will also change Ω_{Ar} in surface water. Intrusion into surface NH-10 water of the low S, high T, and low DIC CR plume will decrease S and DIC and result in a decrease in Ω_{Ar} as plume water dilutes shelf water Ω_{Ar}. Upwelled water is high in S and in DIC. In order to figure out the seasonal controlling mechanisms of Ω_{Ar}, relationships between Ω_{Ar} and DIC were determined for net community production (NCP, the total biological production in the system (that takes up CO_2 from the water) minus the total community respiration (that releases CO_2 into the water), air-sea gas exchange, and the CR plume. In addition, a relationship between Ω_{Ar} and S was determined for the CR plume. The NH-10 and shelf break Ω_{Ar} were plotted against DIC and S and how closely they fell along these relationships was used to determine the controlling mechanisms during each season. In addition,

pre-industrial Ω_{Ar} was estimated to determine how the NH-10 and shelf break Ω_{Ar} range has changed since the industrial revolution.

3.4.2.1. Controlling Mechanism Relationships

The relative influence of various processes on Ω_{Ar} was evaluated by using property:property plots of Ω_{Ar} versus DIC and S to compare reaction pathways NCP, air-sea gas exchange, mixing of water masses, dilution by CR run-off, and T and S effects on K^*_{spAr} with the observed data. The effects of NCP were estimated by varying DIC over the DIC range recorded for the shelf, 1600-2300 µmol kg^{-1}, and correspondingly varying A_T by the Redfield ratio 106:18 (resulting in A_T from 2100-2220 µmol kg^{-1}) at the mean T and S for the observations (T=11.1°C, S=31.96) and calculating Ω_{Ar} in CO2SYS based on these values.

Contributions from the CR plume were represented by a simple two end-member mixing model by diluting the Oregon shelf end-member (mean NH-10 surface values of DIC=1980 µmol kg^{-1}, A_T=2180 µmol kg^{-1}, T=11.1°C, S=31.96) proportionally to salinity to the CR end-member (average CR values of DIC ~1000 µmol kg^{-1}, A_T ~980 µmol kg^{-1}, T ~11.0°C, S ~1.00 (USGS National Stream Quality Accounting Network, http://water.usgs.gov/nasqan/)).

Changes in mixed layer DIC due to gas exchange were calculated using the *Ho et al.* [2011] relationship for gas transfer velocity and an averaged atmospheric pCO_2 for the shelf (392 µatm, [*Evans et al.*, 2011]) divided by the mixed layer depth. The multi-depth temperature data from NH-10 were used to calculate MLD using the approach of *Kara et al.* [2000]. The mean NH-10 DIC was then adjusted over the range of fluxes seen during this period and those DIC values, along with NH-10 mean values for A_T, T, and S, were the inputs for CO2SYS to calculate the gas exchange-Ω_{Ar} relationship. The T and S dependence of K^*_{spAr} were calculated in CO2SYS

using in situ T and S. However, the effects of T and S on K^*_{spAr} resulted in only a small effect on Ω_{Ar} relative to the observed changes and thus will not be considered further.

The California Undercurrent (CU) was assumed to be the upwelling source water for the shelf [*Thomson and Krassovski*, 2010]. CU water typically has T=6.9°C, S=33.9 [*MacFadyen et al.,* 2008], DIC=2150-2290 µmol kg^{-1}, and A_T=2250-2300 µmol kg^{-1} [*van Geen et al.,* 2000; *Hales et al.,* 2005b] to give an estimated Ω_{Ar} of 0.9±0.3 at the average depth of the CU, 225 m [*Thomson and Krassovski*, 2010].

3.4.2.2. Pre-Industrial Ω_{Ar}

The extent to which present day Ω_{Ar} has changed from pre-industrial times was determined using a modified version of the method used by [*Feely et al.*, 2008]. DIC in surface waters was assumed to rise at a rate such that pCO_2 in surface waters maintained a constant offset from atmospheric pCO_2. A_T was assumed to encompass the same range observed in this study, without any transient behavior. The difference between pre-industrial and current annual mean DIC was calculated in CO2SYS using mean surface A_T, T, and S for each season (see Table 3.4.1) and the pre-industrial atmospheric CO_2 estimate for the year 1800 (~280 ppm) [*Sabine et al.*, 2004] or the mean CO_2 values for the years 2007-2011 (~390 ppm, NOAA Earth System Research Laboratory, http://www.esrl.noaa.gov/gmd/ccgg/, see *Conway et al.*[1994]), respectively. The anthropogenic contribution to DIC (ΔDIC) in surface waters is estimated using this method to be ~50, ~53, ~56, and ~56 µmol kg^{-1} in spring, summer, autumn, and winter, respectively.

The ΔDIC was then subtracted from CO2SYS-derived DIC values for 2007-2011 and these adjusted DIC values were used with in situ A_{Tsalin}, T, and S to calculate the pre-industrial Ω_{Ar}. The pre-industrial shelf break Ω_{Ar} was estimated using the same method, calculated using

average in situ pressure for the shelf break (121 dbar). Shelf break source water DIC was estimated to have last been at the surface (and thus in contact with atmospheric CO_2) 50 years previously [*Feely et al.*, 2008] so the mean atmospheric CO_2 value for 1967-1971 (~325 ppm) was used. The estimated ΔDIC for the shelf break is ~25 μmol kg^{-1}.

As a constraint on the above calculations, ΔDIC was also calculated assuming oceanic pCO_2 undersaturation and oversaturation of 50 ppm with respect to historic atmospheric values. This resulted in ΔDIC between ~44 to ~67 μmol kg^{-1} for surface waters which added little uncertainty (±0.1) to the $\Delta\Omega_{Ar}$ estimates. The shift in Ω_{Ar} is thus significant regardless of this level of disequilibrium with atmospheric pCO_2. This method for calculating pre-industrial Ω_{Ar} includes a number of caveats – including the assumptions that seasonal means for A_T, T, and S have not changed since pre-industrial times and that seasonal dynamics are similar each year going back to pre-industrial times. Observations do not exist to allow us to quantitatively assess the uncertainties related to these assumptions, but we cannot think of a scenario where changes in ecosystem functioning are likely to correlate with and mitigate the expected influence of rising atmospheric CO_2.

3.4.3. Results

3.4.3.1. NH10 Field Data

The multi-year time-series data for carbonate parameters and physical parameters can be found in Figures 3.4.1-3.4.5. Discrete data points for 2011 (see Table 3.3.2) are plotted along with time-series data in Figure 3.4.1. pCO_2 data were collected during all four seasons (seasons as designated by *Smith et al,* 2001): spring (April-May), summer (June-August), autumn (September-October), and winter (November-March) across five different years (Figure 3.4.1a).

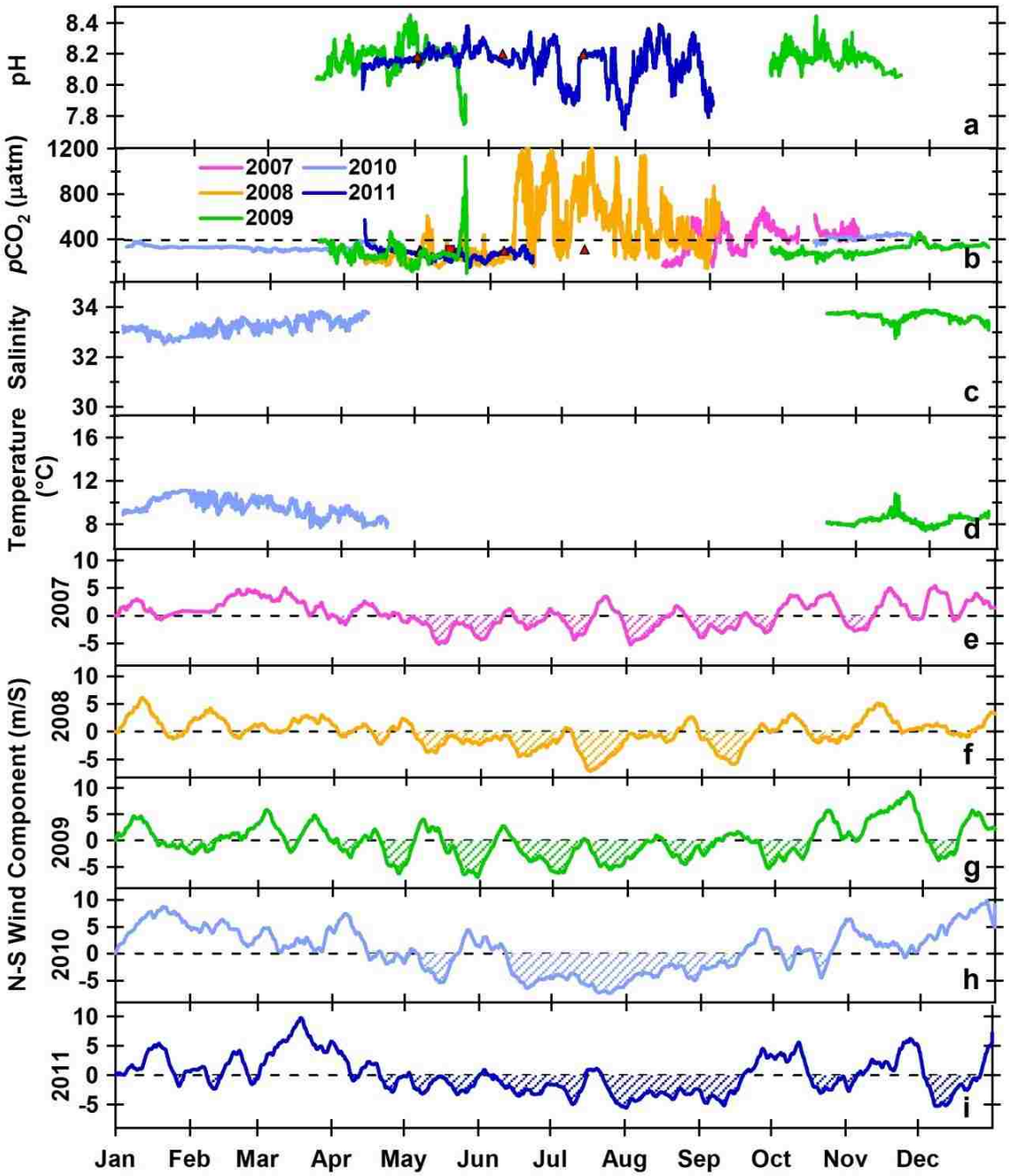

Figure 3.4.1. NH-10 time-series for (a) SAMI-pH, (b) SAMI-CO_2, (c) salinity, (d) temperature, (e-i) N-S wind component for the years 2007-2011. The red triangles show the values of the discrete samples (see Table 3.3.2).

pH data were collected during spring, summer, autumn, but only during the beginning of winter (Figure 3.4.1b). pCO_2 ranged from near 100 µatm to over 1100 µatm and remained undersaturated with respect to the atmosphere for large portions of spring, autumn, and winter (Figure 3.4.1a). Annual mean pCO_2 was 380±172 µatm. Surface pH ranged from 7.716 to 8.443, with the lowest values occurring during the summer upwelling season and the highest values in the autumn (Figure 3.4.1b). The annual mean was 8.139±0.111, slightly higher than the ocean-wide mean of ~8.094±0.0002 [*Dore et al.*, 2009]. T and S had a wide range as well, with temperatures ranging from 7.7°C to 18.2°C and salinity ranged from 22.2 to 33.4 (Figure 3.4.1c-d).

Table 3.4.1. NH-10 Measured parameters (Average ± standard deviation)

	n	pCO_2 (µatm)	pH	T (°C)	S	MLD (m)	Winds (m s^{-1})
Spring	4088	271±80	8.181±0.090	10.3±1.2	30.4±1.8	27±24	2±4
Summer	3788	509±283	8.127±0.130	11.3±1.8	31.6±2.1	10±11	-3±2
Autumn	2317	381±98	8.120±0.130	11.5±1.0	32.6±0.4	11±9	5±6
Winter	3223	358±62	8.129±0.06	10.9±1.1	32.4±0.3	51±22	8±4

Wind direction exhibited a distinct seasonality as expected in this EBUS, with winter winds predominantly and strongly northward and summer winds predominantly and strongly southward (Figure 3.4.1e-i). Wind speed was weaker and wind direction generally more variable during spring and autumn as winds transitioned from predominantly downwelling-favorable to upwelling-favorable in spring and vice versa in autumn (the spring and autumn "transitions", see [*Hickey et al.*, 2006]) (Figure 3.4.1e-i). pCO_2, pH, T, and S also varied seasonally. The seasonal means can be found in Table 3.4.1. Mean pCO_2 was lowest during the spring and highest during the summer upwelling season. Except for the summer, mean pCO_2 values remained below atmospheric values (mean of 392 µatm for the Oregon shelf [*Evans et al.*, 2011]). Conversely,

mean pH was highest during the spring, with the lowest means during summer and into autumn (Table 3.4.1).

Mean surface T was lowest in the spring during the onset of upwelling and highest in the autumn after heating during the summer. Salinity means were lowest during spring and summer. Summer experienced the greatest variability in all parameters except for the N-S wind component (Table 3.4.1).

There was also inter-annual variability in winds, with periods of upwelling-favorable winds occurring as late as December (Figure 3.4.1g and Figure 3.4.1i) and brief periods of downwelling-favorable winds outcropping during the middle of summer (Figure 3.4.1e and Figure 3.4.1g). There was significant inter-annual variability in pCO_2 (Figure 3.4.1a) between autumn 2007, 2009, and 2010, with average values ranging between 274±19 µatm in 2009 to 462±1 µatm in 2010. Mean T and S did not vary as significantly with a mean T of 12.2±0.8°C and mean S of 32.5±0.3 in autumn 2009 and means of 12.4±0.3°C and 32.4±0.1 in 2010.

3.4.3.2. Calculated Carbonate Parameters

A_{Tsalin} and the CO2SYS-calculated carbonate parameters are displayed in Figure 3.4.2. As with the measured parameters, A_{Tsalin}, DIC, and Ω varied significantly more during all seasons except winter. The greatest temporal variability in amplitude occurred during the summer upwelling season (Figure 3.4.2, June through August) as periods of strong upwelling-favorable winds alternated with relaxation events (Figure 3.4.1e-i). The mean surface values can be found in Table 3.4.2. Surface Ω_{Ca} ranged from 2.77 to 6.0 while surface Ω_{Ar} had a range from 0.66 to 3.9 (Figure 3.4.2d and Figure 3.4.2e). The mean Ω_{Ca} was 3.3 ± 0.8 and Ω_{Ar} was 2.2 ± 0.5, both

significantly below the estimated averages for the North Pacific Ocean (Ω_{Ca}=5.0±0.9 and Ω_{Ar}=3.3 ± 0.7) [*Feely et al.,* 2009] (Figure 3.42d-e).

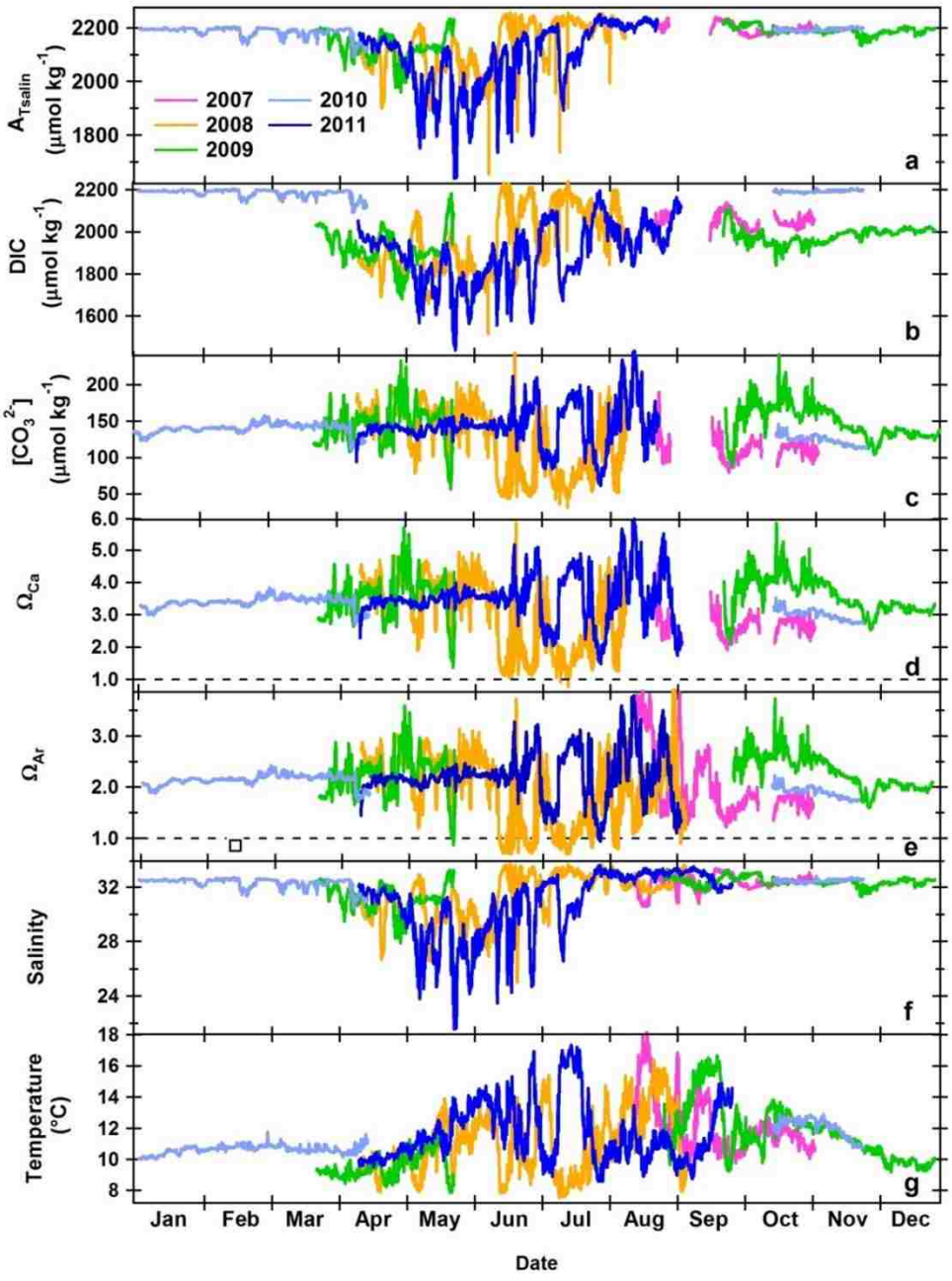

Figure 3.4.2. NH-10 Carbonate Parameters. (a) A_{Tsalin}, (b) DIC, (c) carbonate ion concentration, (d), Ω_{Ca}, (e) Ω_{Ar}, (f) salinity, and (g) temperature.

Table 3.4.2. Calculated carbonate system parameters. (Average ± standard deviation).

	DIC ($\mu mol\ kg^{-1}$)	A_{Tsalin} ($\mu mol\ kg^{-1}$)	Ω_{Ca}	Ω_{Ar}	$[CO_3^{2-}]$ ($\mu mol\ kg^{-1}$)
Spring	1880±103	2087±91	3.6±0.5	2.3±0.4	146±22
Summer	1980±248	2148±106	3.1±1.1	2.0±0.7	126±44
Autumn	2017±57	2198±18	3.2±0.7	2.1±0.6	134±30
Winter	2003±34	2187±14	3.2±0.4	2.1±0.3	134±18

As stated earlier, our focus is on Ω_{Ar}. In one event, surface water Ω_{Ar} changed by ~3 over a diel period (mid-June 2008, Figure 3.4.3, point A). There were eight intervals of $\Omega_{Ar}<1$ (Figure 3.4.3, black numerals) on the surface at NH-10 that persisted from 6 hours to 3 days, although the frequency and duration of upwelling events differed inter-annually.

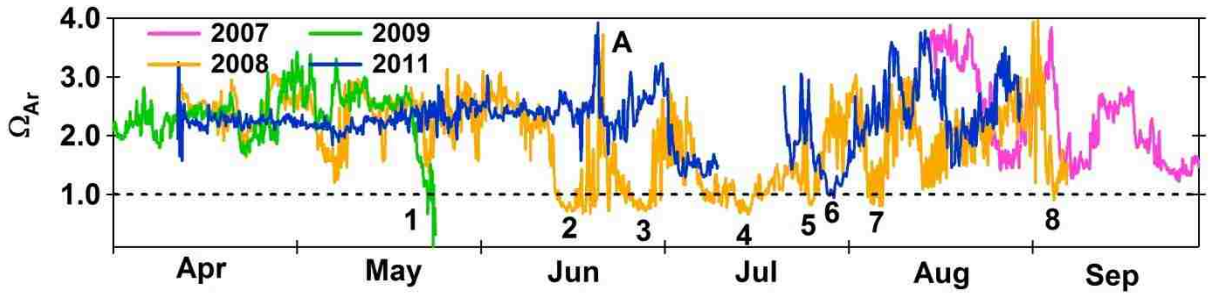

Figure 3.4.3. Summer Ω_{Ar}. "A" refers to a period of rapid and large decrease during 2008. The numbers refer to periods where Ω_{Ar} decreased below 1.0.

In their study of Netarts Bay (2 m average depth) on the Oregon coast, *Barton et al*. [2012] found frequent periods of undersaturation during summer 2009, a result of the stronger influence of upwelling near shore, as well as contributions from nighttime net respiration in shallow sediments of the bay.

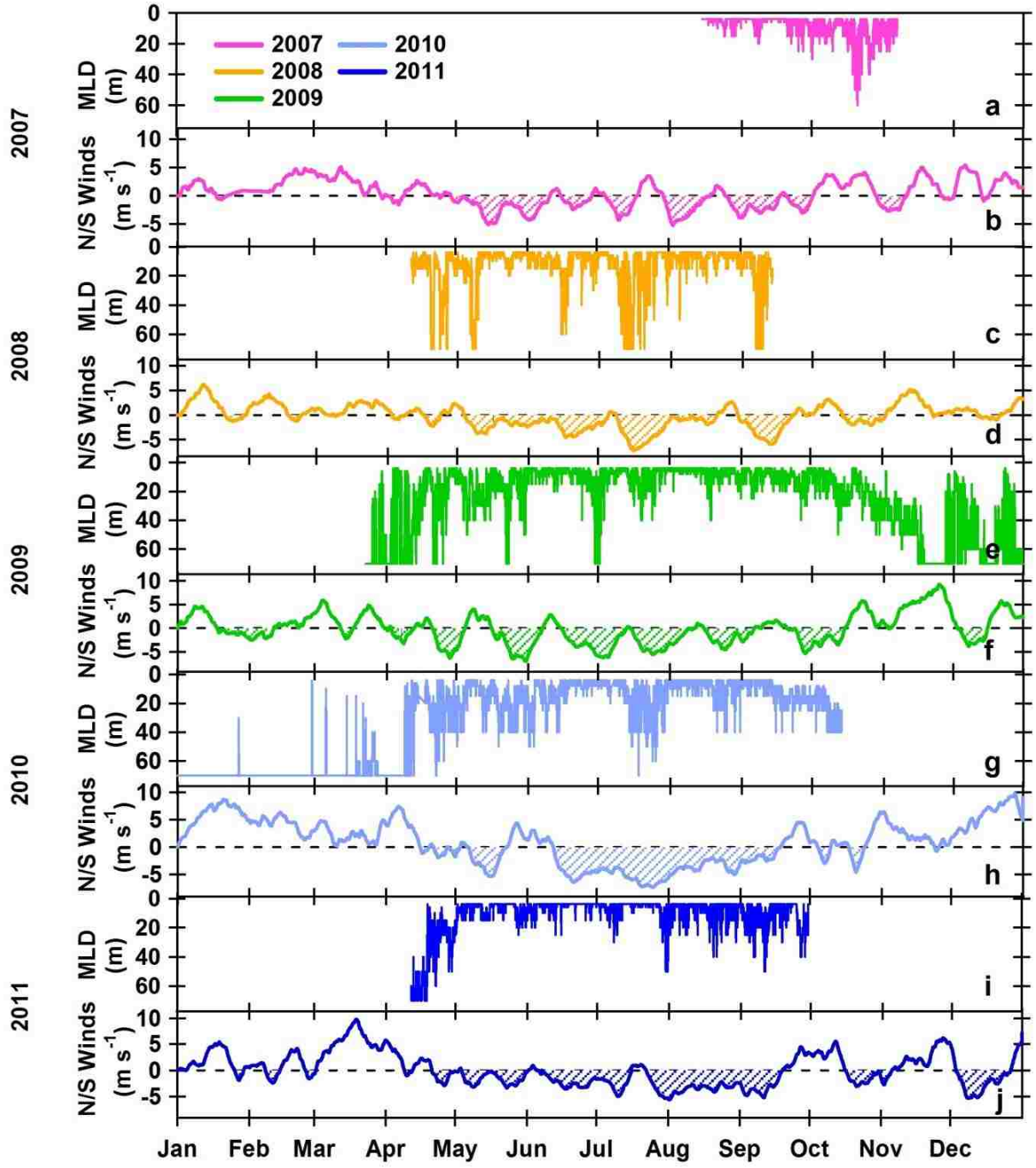

Figure 3.4.4. Mixed layer depth for (a) 2007, (c) 2008, (e) 2009, (g) 2010, and (i) 2011 plotted with the N-S wind component for (f) 2007, (g) 2008, (h) 2009, (h) 2010, and (j) 2011.

Mixed layer depth is compared to the N-S wind component in Figure 3.4.4. The MLD deepened during periods of stronger winds, both during strong upwelling and strong downwelling-favorable winds. The seasonal means for MLD and N-S wind component are found in Table 3.4.3. Mean MLD was greatest in the winter, as was the magnitude of the mean N-S wind component. The mean MLD decreased significantly during the summer and autumn as surface heating stratified the water column in between periods of upwelling-favorable winds.

Table 3.4.3. Average seasonal mixed layer depth and average seasonal N-S wind component strength (Average ± standard deviation).

	MLD (m)	Winds ($m\ s^{-1}$)
Spring	27±24	2±4
Summer	10±11	-3±2
Autumn	11±9	5±6
Winter	51±22	8±4

Oxygen data was only collected during parts of three years: in the late summer of 2008 (Figure 3.4.5), in late autumn and winter of 2009 (Figure 3.4.6), and spring and early summer of 2011 (Figure 3.4.7). Oxygen concentrations correlated negatively with the pCO_2 moderately well in 2009 (R^2=0.673, p<0.0005, n=2838) but less so in 2008 (R^2=0.324 p<0.0005, n=1708) and 2011 (R^2=0.266, p<0.0005, n=1708). In April 2008, concentrations were moderately high (~300 μM) but were depleted during high-CO_2 upwelling events and by early September were down near 250 μM, near saturation. Concentrations were high at the beginning of autumn 2009 (>350 μM) but declined to around 250 μM during the winter. Oxygen concentrations were near 350 μM at the beginning of spring in 2011 but displayed a downward trend until the start of summer.

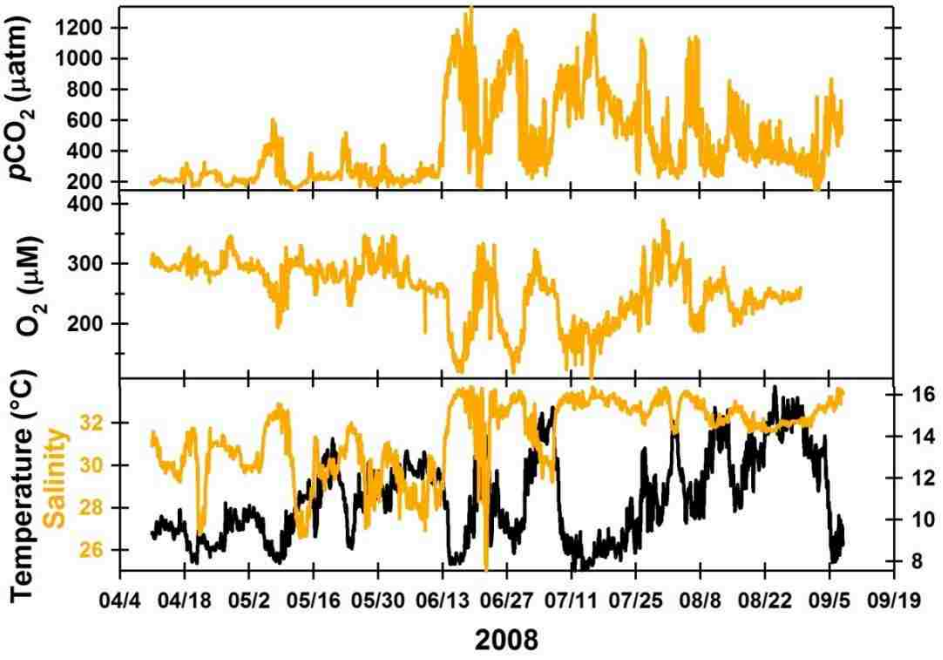

Figure 3.4.5. (a) SAMI-CO_2, (b) O_2, and (c) temperature and salinity data for April-September 2008.

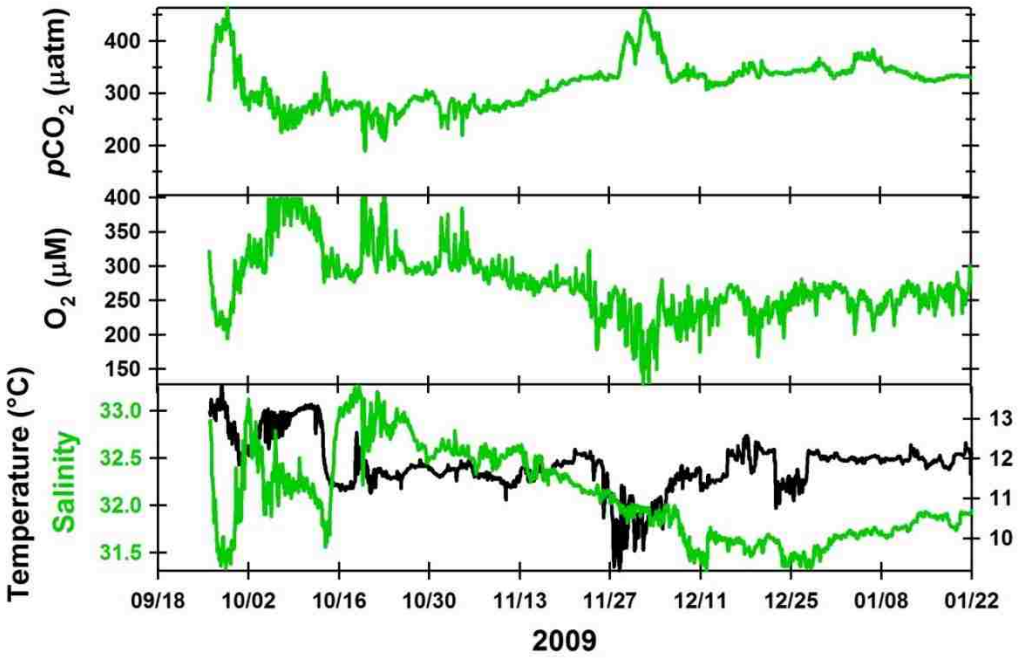

Figure 3.4.6. (a) SAMI-CO_2, (b) O_2, and (c) temperature and salinity data for October 2009-January 2010.

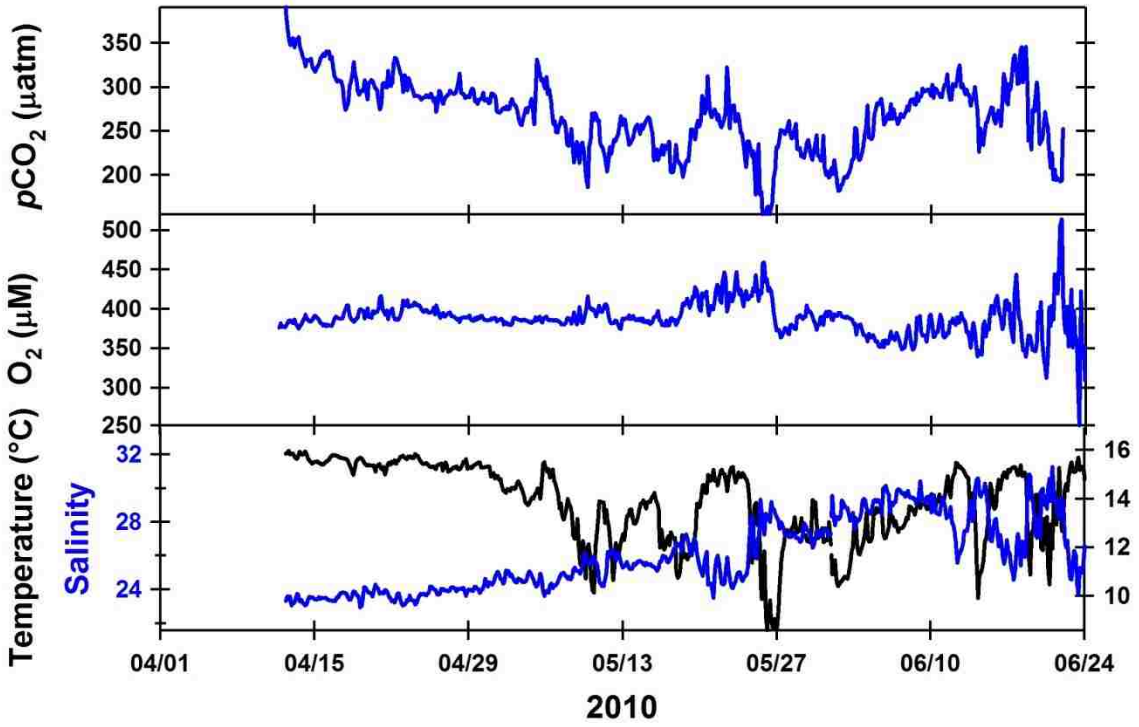

Figure 3.4.7 (a) SAMI-CO_2, (b) O_2, and (c) temperature and salinity data for April-June 2011.

3.4.3.3. Shelf Break Mooring

As expected, average winter shelf break bottom water was colder and saltier than surface (NH-10) water (see Table 3.4.4 for mean shelf break parameters). Mean pCO_2, DIC, and A_{Tsalin} were significantly higher than at the surface for the beginning of this record while average Ω_{Ca}, Ω_{Ar}, and $[CO_3^{2-}]$ values in shelf break bottom boundary layer waters were lower (Tables 3.4.2 and 3.4.4). The mean winter values for DIC and A_{Tsalin} were near the lower bounds for values predicted for the CU (DIC=2150-2290 µmol kg^{-1}, and A_T=2250-2300 µmol kg^{-1} [*van Geen et al.*, 2000; *Hales et al.*, 2005b]) Due to remote wind forcing [e.g. *Hickey et al.*, 2006], low Ω_{Ar} waters (Figure 3.4.8f, point A) appeared long before local winds indicated upwelling- favorable conditions. The periods of low saturation support the seasonal dynamics of Ω_{Ar} predicted for

shelf break waters by *Juranek et al.* [2009]. During early winter 2009, there was a large spike in shelf break physical and carbonate parameters (Figure 3.4.8, point B and Figure 3.4.9b).

Table 3.4.4. Measured and calculated parameters for the shelf break. (Average ± standard deviation).

n	pCO_2 (µatm)	T (°C)	S	A_{Tsalin} (µmol kg^{-1})
2060	636±230	9.2±1.0	33.4±0.3	2243±14
n	**DIC (µmol kg^{-1})**	**Ω_{Ca}**	**Ω_{Ar}**	**$[CO_3^{2-}]$ (µmol kg^{-1})**
2060	2135±70	1.8±0.6	1.4±0.5	89±29

When compared with surface values for Ω_{Ar} (Figure 3.4.9a), it appears that the water column is mixed by downwelling all the way to the shelf break. Comparison with MLD data (Figure 3.4.9c) confirms that this is possible, with a MLD>70 m at that time. Unlike the near-Gaussian distribution seen in surface Ω_{Ar} (Figure 3.4.10), the deep shelf break water was constrained by the lower Ω_{Ar} of the California Undercurrent end-member (Figure 3.4.9b); estimated to be 0.9±0.3 from mean California Undercurrent T, S, DIC, and alkalinity (A_T) (see section 3.4.2.1).

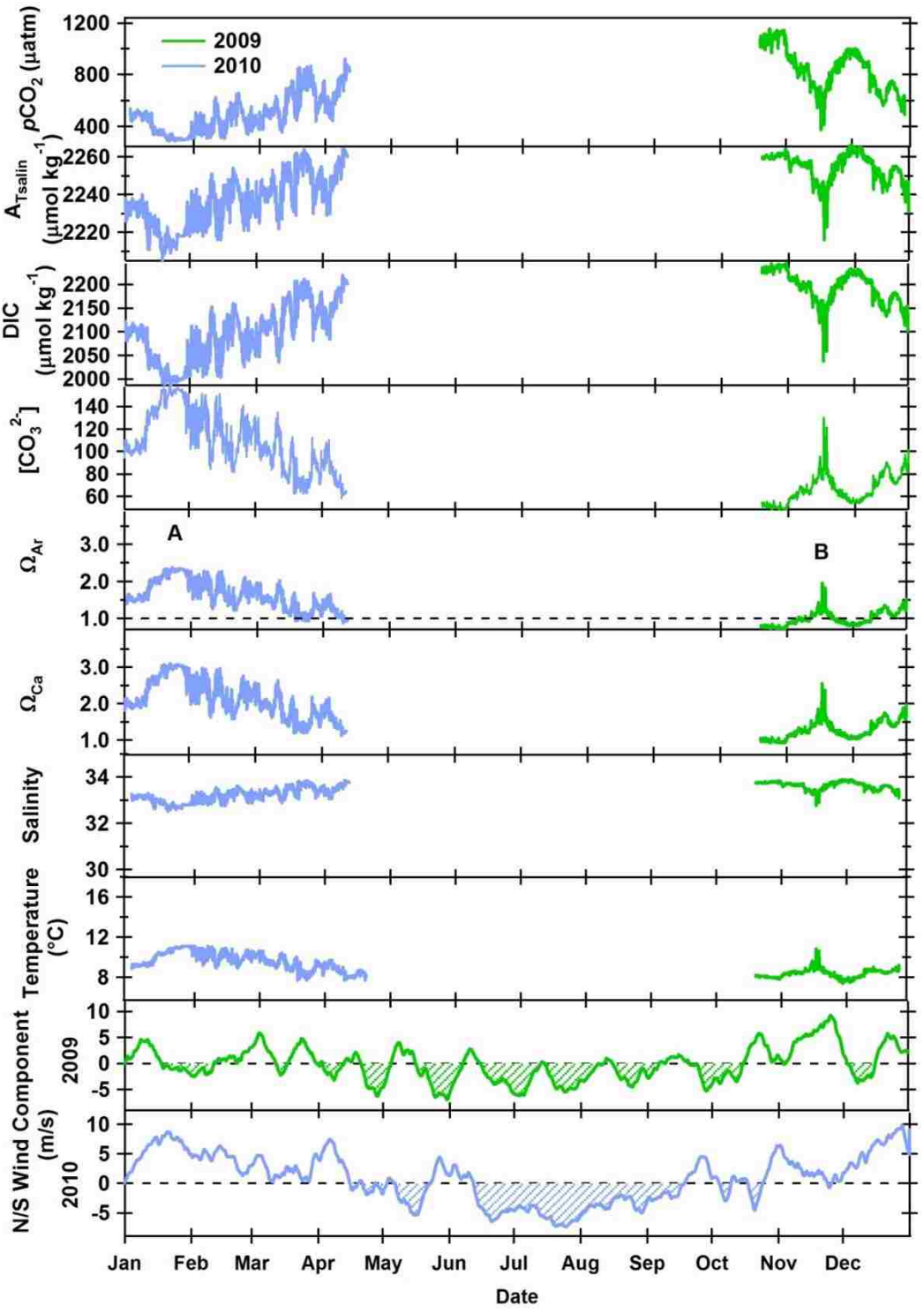

Figure 3.4.8. Shelf break (a) SAMI-CO_2, (b) A_{Tsalin}, (c) DIC, (d) Ω_{Ar}, (e) Ω_{Ca}, (f) salinity, (g) temperature, and N-S wind component for 2009 (h) and 2010 (i).

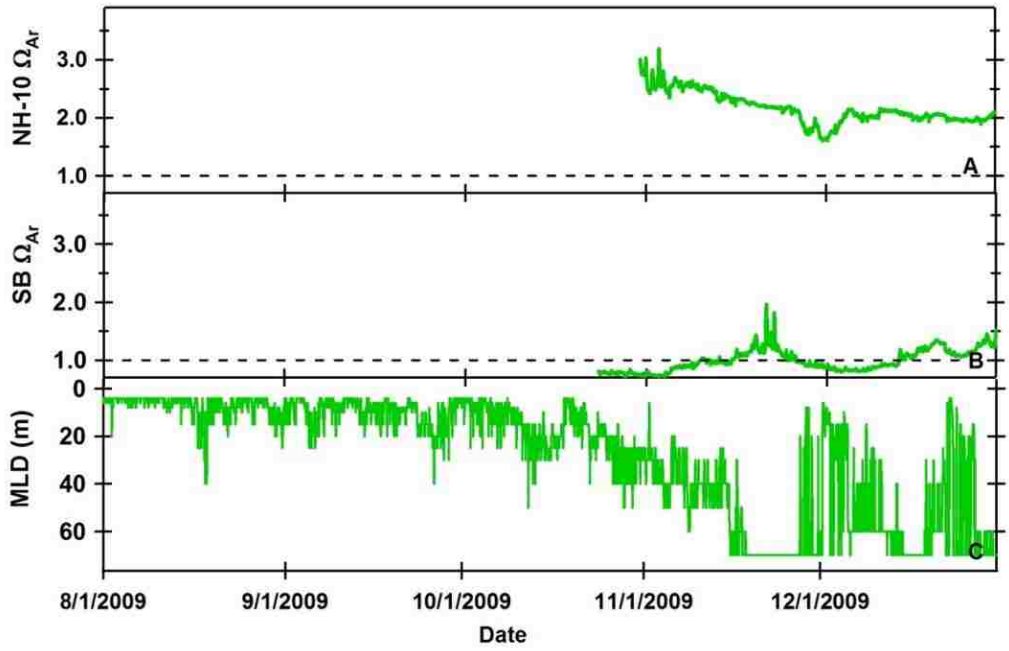

Figure 3.4.9. (A) NH-10 and (B) shelf break (SB) Ω_{Ar} during autumn 2009 plotted with (C) MLD.

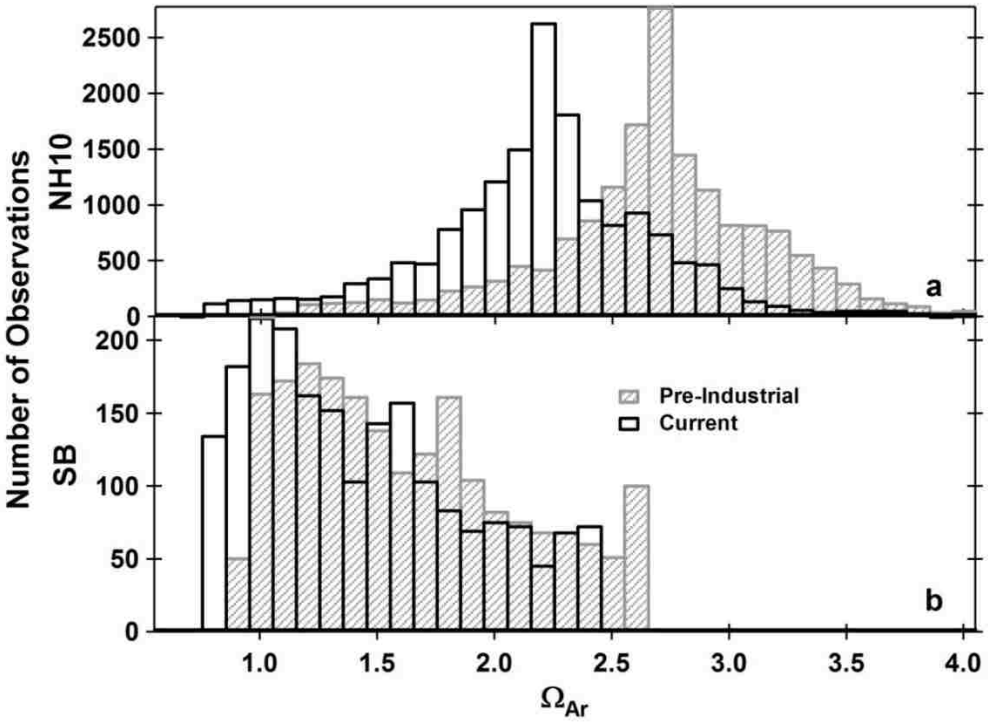

Figure 3.4.10. Frequency distribution of Ω_{Ar} at (a) NH-10 and (b) the shelf break (SB).

3.4.4. Discussion

Several processes contribute to Ω_{Ar} variability on the shelf including upwelling and other water mass changes (e.g. riverine inputs), NCP, and air-sea gas exchange. Variability from $CaCO_3$ formation and dissolution is expected to be minimal in this area [*Fassbender et al.,* 2011]. We plotted Ω_{Ar} versus DIC and S (Figure 3.4.11) to discern relative contributions from each mechanism, calculated as described in (section 3.4.2.1). Several of these processes were important but varied widely between seasons and from year to year (Figure 3.4.11). Spring data are discussed first with inter-annual variability discussed when applicable.

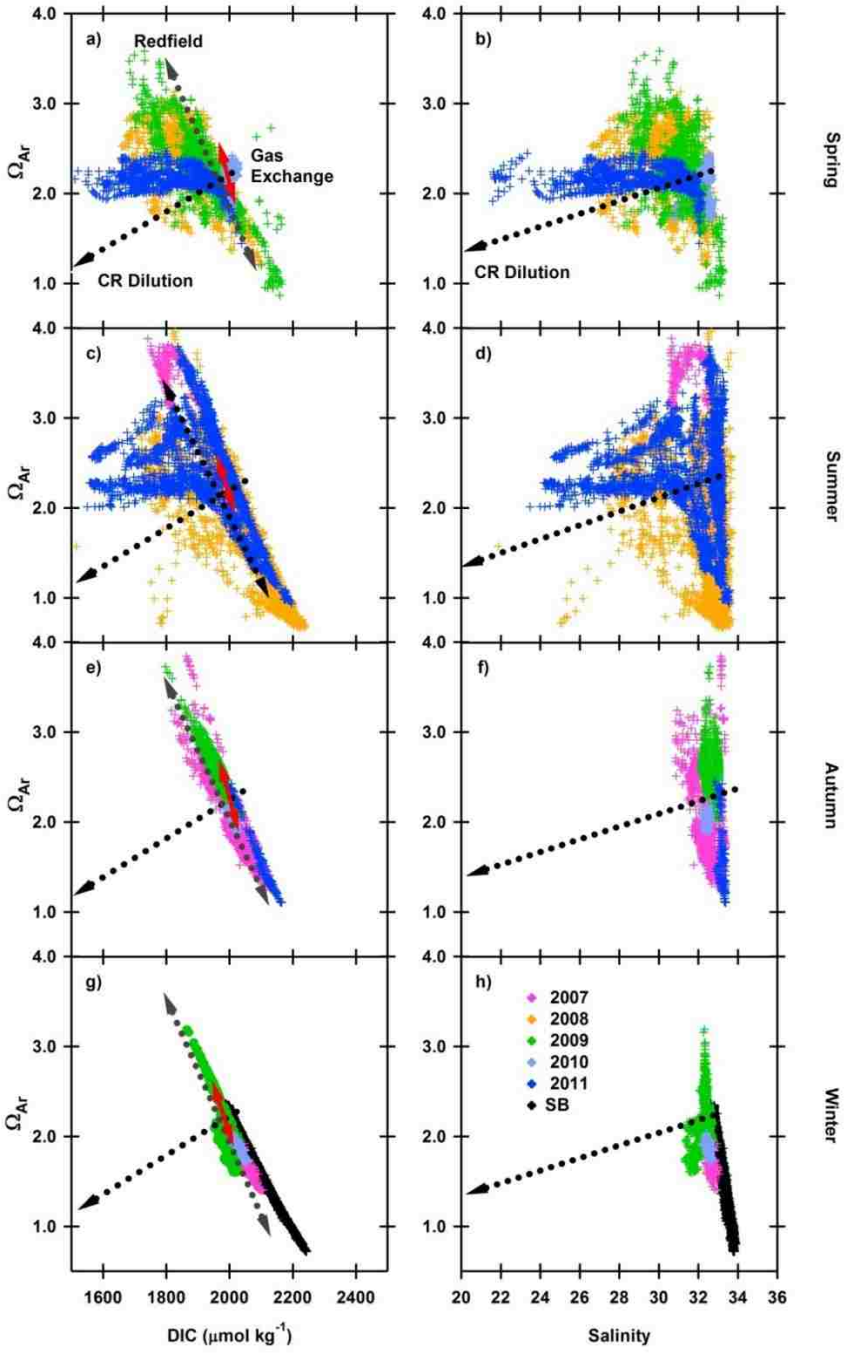

Figure 3.4.11. Property: property plots by season for NH-10 and shelf break (SB) Ω_{Ar}. Ω_{Ar} vs. DIC for spring (a), summer (c), autumn (e), and winter (g). The Redfield relationship (as an indicator of biological productivity, grey dashed line), CR dilution relationship (black dashed line), and gas exchange relationship (red line) are plotted over in situ values for 2007 (pink), 2008 (orange), 2009 (green), 2010 (light blue), and 2011 (dark blue). Ω_{Ar} vs. salinity for spring (b), summer (d), autumn (f), and winter (h) plotted with the CR dilution relationship (black dashed line). Colors represent the same years as in (a, c, e, g).

3.4.4.1. Spring Surface Ω_{Ar} Controlling Mechanisms

Spring (April-May, 2008-2010) variability generally followed NCP and gas exchange relationships (Figure 3.4.11a). Surface Ω_{Ar} values extended along the Redfield relationship from low Ω_{Ar} (0.8-1.3) and high DIC indicative of the shelf break end-member to high Ω_{Ar} (>3.0) and low DIC as nutrient-rich upwelled waters triggered biological DIC uptake and drove Ω_{Ar} up. Biological production uses up the excess preformed nutrients that accompany the upwelled water [*Hales et al.,* 2005a, 2005b, 2006] and surface water pCO_2 can be driven well below atmospheric saturation, thereby increasing Ω_{Ar} and extending the original Redfield signature of the upwelled shelf break water (Figure 3.4.11a, shelf break data in g).

Table 3.4.5. Mean Upwelling Index[a] (UI, $m^3\ s^{-1}\ 100\ m^{-1}$ coastline) and CR Discharge[b] ($m^3\ s^{-1}$)

	2007		2008		2009		2010		2011	
	UI	**River Discharge**	**UI**	**River Discharge**	**UI**	**River Discharge**	**UI**	**River Discharge**	**UI**	**River Discharge**
Spring	22.2	5100	25.3	6870	19.9	7220	-1.55	3400	2.14	9710
Summer	24.6	5910	34.8	6680	34.8	6460	43.4	5950	37.0	9340
Autumn	-1.95	2670	12.6	2710	-14.4	2490	-26.8	2750	NA	NA
Winter	-42.8	3920	-30.7	3990	-105	3450	-77.0	5180	NA	NA

[a] PFEL Upwelling Indices for 125°W, 45°N, http://www.pfeg.noaa.gov/

[b]Columbia River Fisheries, http://www.fpc.org/

Spring 2011 exhibited strong effects of CR dilution relative to the previous springs as Ω_{Ar} was depressed due to dilution of $[Ca^{2+}]$ and $[CO_3^{2-}]$ by the CR plume (Figure 3.4.11a-b) [*Salisbury et al.*, 2008; *Chierici and Fransson*, 2009]. The CR plume regularly extends southward from the river mouth during spring and summer although its width and distance from shore vary based on wind conditions and water discharge [*Hickey et al.*, 2005; *Burla et al.*, 2010]. Water gauge

records for the Columbia River (Table 3.4.5, Figure 3.4.12) indicate the spring 2011 river discharge was 130-140% greater than that during spring 2008 and 2009. The higher discharge and weaker upwelling (as measured by upwelling index, Table 3.4.5) during this period resulted in a stronger influence of the CR plume relative to other years. The 2011 data do not exactly follow the CR dilution trend and it is likely that NCP increased Ω_{Ar} (up to ~0.75) above the Ω_{Ar} predicted by the CR dilution trend (Figure 3.4.10a-b).

Fassbender et al. [2011] examined DIC dynamics on the U.S. West Coast using cruise data from two Northern California shelf transects during May 2007. They used a box model to estimate the effect of primary productivity on inorganic carbon dynamics and found that full utilization of available nitrate would result in a sea surface Ω_{Ar} of ~3. This value is comparable to the maximum spring sea surface Ω_{Ar} values observed at NH-10 (Figure 3.4.2; Figure 3.4.11a, 2008, 2009), supporting the importance of NCP in regulating Ω_{Ar} on the shelf.

3.4.4.2. Summer Surface Ω_{Ar} Controlling Mechanisms

Relationships between Ω_{Ar}, DIC, and S during summer (June-August, 2008 and 2011) (Figure 3.4.11c-d) are similar to those observed for the spring. In 2008 [*Evans et al.,* 2011] and 2011 the strong influence of the CR plume due to weaker upwelling and higher CR discharge (compared to 2010, Table 3.4.5) suppressed Ω_{Ar}.

3.4.4.3. Autumn and Winter Surface Ω_{Ar} Controlling Mechanisms

Trends in Ω_{Ar} in autumn (September-October) (Figure 3.4.11e-f) and early winter (Figure 3.4.11g-h) closely followed the predicted trends in biological productivity and gas exchange with little evidence of the dilution effects seen in spring and summer (Figure 3.4.11e and g).

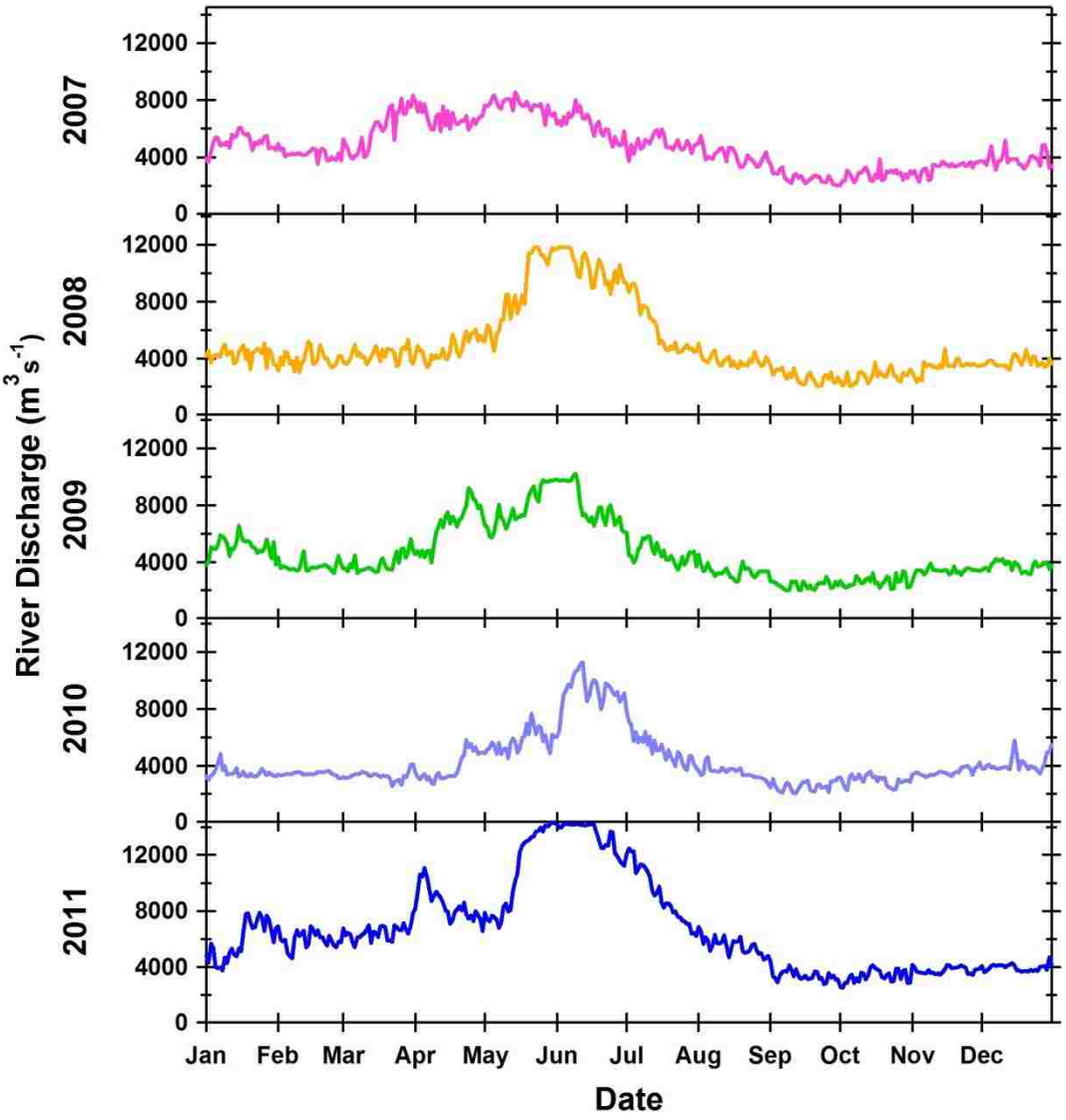

Figure 3.4.12. Columbia River discharge at Bonneville, Washington.

In autumn 2009 the Ω_{Ar} was high (>3.0, Figure 3.4.2e) but began to decline, likely due to convective mixing of the water column. In mid- to late November 2009, the MLD (Figure 3.4.4e) deepened from near 25 m to >70 m, mixing surface and subpycnocline water and lowering surface Ω_{Ar}. Winter shelf break and NH-10 Ω_{Ar} relationships overlapped as a result of the homogenized water column (Figure 3.4.9; Figure 3.4.11g-h). After this period surface Ω_{Ar}

varied little for the remainder of winter 2009, with an average of 2.2±0.4. Autumn 2010 Ω_{Ar} was significantly lower than in 2009 as a result of the prolonged and intense summer upwelling (Figure 3.4.2e).

3.4.4.4. Winter Shelf Break Ω_{Ar} Controlling Mechanisms

Winter shelf break Ω_{Ar} were mainly influenced by vertical mixing, downwelling and movement of upwelled water onto the shelf driven by remote wind forcing[*Hickey et al.*, 2006] (Figure 3.4.11g-i). There was little short-term variability in comparison to the surface data because these bottom waters were not influenced by gas exchange, heating or cooling, or the CR plume to any significant extent.

3.4.5. Implications

The range in inorganic carbonate data discussed above was used to back-calculate the natural (i.e. pre-industrial) Ω_{Ar} range on the shelf (see section 3.4.2.2). This analysis indicates that mean contemporary Ω_{Ar} is 0.52 less than mean pre-industrial levels (Figure 3.4.10). Pre-industrial Ω_{Ar} was rarely undersaturated whereas contemporary surface values occasionally drop as low as 0.66. At the shelf break, contemporary Ω_{Ar} is undersaturated ~30% of the time whereas pre-industrial undersaturation occurred only ~10% of the time. These changes in Ω_{Ar} from pre-industrial levels are consistent with the findings of the modeled simulations of *Hauri et al.* [2013] which also concluded that contemporary Ω_{Ar} observations in the California Current System have already shifted substantially from the pre-industrial range. It is unclear to what extent the shift to lower saturation in surface waters is affecting local organisms, all of which evolved in pre-industrial conditions. Reductions in $\Omega_{Ar,}$ even for waters that remain supersaturated, have been shown to harm many aragonite-forming organisms, resulting in shell

dissolution for pteropods [*Bednaršek et al.*, 2012; *Comeau et al.*, 2012], decreased larval and mid-stage growth rates in bivalves [*Gazeau et al.*, 2007; *Barton et al.*, 2012; *Green et al.*, 2012] and lower developmental rates in echinoderms [*Shirayama and Thornton*, 2005; *O'Donnell et al.*, 2010]. Researchers that conduct ocean acidification-related organismal studies should consider the range of variability in this study when developing experimental designs. In addition, this study suggests that Ω_{Ar} can be calculated with reasonable accuracy from previously collected pH or pCO_2 data if salinity was also measured and the relationship with alkalinity is known.

With atmospheric CO_2 concentrations continuing to rise and an increasing trend in upwelling wind strength and duration [*Bakun*, 1990; *Schwing and Mendelssohn*, 1997; *McGregor et al.*, 2007] it is likely that periods of undersaturation will increase in both frequency and intensity. Therefore, long-term monitoring of ocean saturation states will continue to be necessary.

3.5. Inorganic Carbon and Saturation State Dynamics during Upwelling Events in an Eastern Boundary Upwelling System

3.5.1. Introduction

There are four major Eastern Boundary Upwelling Systems (EBUS): the California Current System off the U.S. West Coast, the Humboldt Current System off the coasts of Peru and Chile, the Benguela Current System off the coast of West Africa, and the Iberia/Canary Current System off the coast of Spain [*Chavez and Messié*, 2009]. EBUS occur at the eastern edges of subtropical gyres where seasonal equatorward winds interact with the earth's rotation to transport coastal surface waters toward the open ocean. These coastal waters are replaced by upwelling of subsurface waters near the coast [see *Allen*, 1973; *Bakun,* 1996]. The upwelled subsurface water has significantly higher salinity and partial pressure of carbon dioxide (pCO_2) and lower temperature, pH, and calcium carbonate saturation states. Because of the transport of subsurface water to coastal surface waters, EBUS carbonate system parameters are highly variable during the upwelling season and thus have been a recent focus of study because of their contributions to the global carbon cycle [*Chavez et al.*, 2007].

Most previous studies on carbonate system dynamics during upwelling events have been based on cruise data [e.g. *van Geen et al.*, 2000; *Borges and Frankignoulle*, 2002; *Cao et al.*, 2011; *Fassbender et al.*, 2011] . Due to the temporal limitations of cruise data coverage, these datasets focused on single upwelling events. The main controlling mechanisms for the carbonate system were found to vary between studies. *van Geen et al.* [2000] found significant spatial differences during upwelling off of Cape Blanco in southern Oregon, with biological productivity the main controlling factor north of Cape Blanco and mixing with upwelled bottom waters the main

control to the south. In the coastal upwelling system off the coast of Spain, *Borges and Frankignoulle* [2002] determined that mixing of surface water with the upwelled water mass and the primary production resulting from upwelled nutrients were the main controls of total dissolved inorganic carbon (DIC). *Cao et al.* [2011] studied upwelling carbonate system dynamics over the river-influenced Northern South China Sea shelf and found that mixing of shelf water with the low-DIC and A_T water of the Pearl River plume was the major control of Ω_{Ar} variation. *Fassbender et al.* [2011] determined that the DIC change during an upwelling event in May 2007 along the coast of northern California was primarily controlled by production and respiration of organic matter. In a study of an upwelling event along the Oregon coast in 2001 *Hales et al.* [2005b] found that pCO_2 could be drawn down below atmospheric concentrations post-upwelling due to biological utilization of pre-formed nutrients in the upwelled water mass. The potential impacts of ocean acidification on the marine biota that inhabit coastal upwelling zones make these important regions to study. However, shipboard measurements of the carbonate system during multiple upwelling events are difficult due to the focus on spatial coverage in lieu of greater temporal coverage. Shipboard studies are generally limited to a single upwelling event, making generalization of global or even regional upwelling systems difficult.

Aragonite and calcite are biologically important to a number of marine organisms found in the coastal oceans of the CCS such as corals, bi-valves, clams, gastropods, and echinoderms. In experiments with elevated CO_2 conditions (based on predicted future atmospheric CO_2), the resulting lowered calcium carbonate saturation states negatively affected a variety of calcifying organisms [*Green et al.,* 2009; *Miller et al.,* 2009; *Thomsen et al.,* 2010; *Waldbusser et al.,* 2011]. Although some studies indicate that higher CO_2 oceans can have beneficial effects for

some calcifying species [see *Wood et al.,* 2008; *Byrne et al.,* 2009; *Dupont et al.,* 2010; *Pansch et al.,* 2012], there is evidence that these effects may not be sustainable over long periods [i.e. *Wood et al.,* 2008]. The detrimental effects of low Ω_{Ar} waters on Pacific Oyster (*Crassostrea gigas*) larval production have already been observed in a hatchery along the Oregon Coast [*Barton et al.,* 2012]. Adult oyster shells are predominantly calcite but oyster larvae shells are primarily made of aragonite and so are more susceptible to low pH conditions. Because low calcium carbonate saturation states have damaging effects on the larval stages of this economically-important species and on multiple other coastal calcifying organisms (e.g., sea urchins, calcifying plankton, coralline algae [*Kurihara and Shirayama*, 2004; *Morse et al.*, 2006; *Ries et al.*, 2009]), these organisms are particularly susceptible to ocean acidification. Thus it is important to characterize and study upwelling Ω_{Ar} dynamics in the ecosystems where these organisms live.

A unique high temporal resolution carbonate system dataset recorded over multiple years in the northern California Current System (CCS) allows a new opportunity to study upwelling in greater detail [*Evans et al.,* 2011; *Harris et al.,* 2013]. The upwelling season in the northern CCS starts when winds transition in the spring from predominantly poleward to predominantly equatorward. Throughout the summer periods of upwelling brought on by the strong equatorward winds alternate with relaxation periods during weaker winds or changes in wind direction [*Hickey et al.*, 2006]. The Oregon coastal carbonate system varies greatly as surface water mixes with upwelled bottom waters [*Hickey et al.,* 1979]. During periods of upwelling, pCO_2 increases from below atmospheric saturation (280 µatm) to values exceeding 1200 µatm in short periods of time [*Evans et al.*, 2011; *Harris et al.*, 2013]. DIC increases from near 1900 µmol kg^{-1} to near or above 2100 µmol kg^{-1} during the same time period. Saturation states of the

calcium carbonate minerals calcite and aragonite, Ω_{Ca} and Ω_{Ar}, decrease dramatically, with values for the more soluble aragonite saturation state decreasing from near 3.0 to values below 1.0 (undersaturation) over a period of a couple of days [*Harris et al.*, 2013]. Aragonite undersaturation (Ω<1.0) events can last from a few hours to a few days [*Harris et al.*, 2013]. During wind relaxation or intermittent downwelling-favorable conditions, the lower salinity (S), DIC, alkalinity (A_T) and Ω Columbia River (CR) plume advects from offshore into shelf coastal waters [*Hickey et al.*, 2010], altering the shelf carbonate system parameters.

In this study, we use the high temporal resolution carbonate system data reported by *Evans et al.* [2011] and *Harris et al.* [2013] to investigate the controls on the carbonate system following multiple strong upwelling events. *Evans* [2011] discussed the environmental controls on air-sea CO_2 flux during a strong upwelling event in July 2008. *Harris et al.* [2013] characterized the range of Ω_{Ar} dynamics during the multi-year dataset and analyzed the seasonal controlling factors on Ω_{Ar} changes. This study expands upon that work to encompass all upwelling seasons covered in the multi-year Oregon Coast dataset discussed by *Evans et al.* [2011] and *Harris et al.* [2013]. This includes upwelling events throughout the upwelling season and during different years spanning 2007-2011.

A simple box model was used to predict the relative influence of the three primary controlling mechanisms expected from previous studies: mixing with upwelled water or advection of CR plume freshwater, net community production, and air-sea CO_2 gas exchange. DIC and Ω_{Ar} variability was modeled during each upwelling "event" and contributions from each of the controlling mechanisms were calculated. Correlations between post-upwelling rates of DIC or Ω_{Ar} change and a number of physical and environmental parameters (i.e., pre- and post-event upwelling index, chlorophyll-a concentrations, salinity changes, upwelling duration, etc.) were

determined. Mixing/advection were the predominant control for both DIC and Ω_{Ar} during most events studied. Net community production (NCP) controlled a comparatively small proportion of DIC and Ω_{Ar} change mainly through the uptake of carbon; however, during one event net respiration contributed to the overall rate of change in DIC and Ω_{Ar} by somewhat suppressing the rate of change due to mixing/advection. Upwelling index had the strongest correlations with rates of DIC and Ω_{Ar} change, specifically with the changes due to mixing/advection. A larger upwelling index resulted in a larger rate of change due to mixing.

3.5.2. Materials and Methods

3.5.2.1. Field Site Data

The CCS is divided into three separate sections, each with their own characteristics [*Mackas*, 2006]. The Northern CCS is an area of intense seasonal upwelling which leads to large changes in the coastal marine inorganic carbon system [*van Geen et al.*, 2000; *Hales*, 2005b; *Hales et al.*, 2006; *Ramp and Bahr*, 2008; *Evans et al.*, 2011; *Fassbender et al.*, 2011; *Harris et al.*, 2013]. The upwelling of high pCO_2, low pH waters results initially in large CO_2 fluxes out of the water [*Hales*, 2005b; *Evans et al.*, 2011] and low aragonite saturation states, sometimes to $\Omega_{Ar}<1.0$ [*Feely et al.*, 2008; *Fassbender et al.*, 2011; *Harris et al.*, 2013]. The NH-10 mooring, run by Oregon State University as part of the Oregon Coastal Ocean Observing System (OrCOOS), is located on the Newport Hydrographic (NH) Line along 46.55°N near the southern edge of the Northern CCS. The mooring is located roughly at the mid-point of the continental shelf [*Huyer et al.*, 2007]. This location was chosen for this study because bathymetry along the NH Line is relatively simple, unmarred by major seafloor canyons or ridges [*Kundu and Allen*, 1976; *Kirincich and Barth*, 2009]. The large, upwelling-induced changes in the inorganic carbon

system and the relatively uncomplicated bathymetry make the NH-10 mooring well-situated for research into the forces controlling the natural inorganic carbon dynamics during the summer upwelling season.

Time-series carbonate system data were collected using Submersible Autonomous Moored Instruments for pH and pCO_2 (SAMI-pH and SAMI-CO_2), [*DeGrandpre et al.* 1995;1999; *Seidel et al.,* 2008] deployed at a depth of ~2m on the NH-10 mooring (124.304°W, 44.633°N) approximately 18 km west of Newport, Oregon. Both instruments use spectrophotometric methods of detection. Prior to deployment the SAMI-pH is tested for precision and accuracy using a tris buffer certified reference material [*Delvalls and Dickson*, 1998] and the SAMI-CO_2 is calibrated in a temperature-controlled water bath using standard CO_2 gas mixtures and the accuracy verified with concurrent measurements from an infrared CO_2 sensor (LI-COR, LI-840A). pCO_2 and pH field data verification (quality assurance and quality control) are explained in detail in the supplemental material of *Harris et al.* [2013]. SAMI-CO_2 accuracy during the five years of deployment averaged between 2-11 µatm and SAMI-pH accuracy averaged between 0.01-0.02 during the three years pH instruments were deployed.

The recorded pH and pCO_2 data were used along with a salinity-derived alkalinity (A_{Tsalin}) [see *Gray et al.,* 2011; *Harris et al.,* 2013] to calculate other carbonate system parameters in CO2SYS [*Pierrot et al.,* 2006], including DIC and Ω_{Ar}. Uncertainty in DIC and Ω_{Ar}, based on the comparison of the values calculated for DIC and Ω_{Ar} in CO2SYS from A_{Tsalin} and pCO_2 and A_{Tsalin} and pH was between 4±15 µmol kg^{-1} and 6±6 µmol kg^{-1} and -0.09±0.13 and 0.16±0.14, respectively. Additional data included temperature (T) sensors at 10 depths (Sea-Bird SBE39), salinity (S) at 4 depths (Sea-Bird Micro-Cat SBE37), and a solar radiation sensor at the surface ((LI-COR LI-200). Upwelling indices (UI) were retrieved for 125°W, 45°N from Pacific

Fisheries Environmental Laboratory (PFEL) (www.pfeg.noaa.org). Satellite chlorophyll-a (chl-a) was retrieved from the European Space Agency's GlobColour database (http://hermes.acri.fr). Level-3 products were averaged [*Antoine,* 2004; *Lee,* 2006] from MODIS, SeaWiFS, and MERIS chl-a products. The chl-a level-3 products used in this study were retrieved at a 1 km resolution for the 10 km x 10 km bin centered on NH-10 and averaged.

3.5.2.2. Selecting Upwelling Events

Each year's upwelling season (2007-2011) was calculated using cumulative upwelling index (CUI) to approximate the start and end dates [see method by *Schwing et al.*, 2006]. Plotting CUI (calculated using the PFEL-derived UI) yields an initially shallow curve followed by a steep increase before leveling off. The point at which the CUI initially becomes positive is the upwelling season start date and the inflection point when the curve begins to decrease is the end date of that upwelling season.

Since the ultimate focus of this study was changes in Ω_{Ar}, Ω_{Ar} time-series data were low-pass filtered (30-hr) and plotted. Periods where the Ω_{Ar} dropped significantly and rapidly ($\Delta\Omega_{Ar} \geq 1.0$, over a period of 3-4 days) and at least initial UI was high (>100 m^3 s^{-1} 100 m^{-1} coastline were selected to be analyzed. During spring and autumn upwelling events of ~4 days are interspersed with long (6-7 days) periods of wind relaxation or reversal [*Papastephanou et al.*, 2006]. During the summer, upwelling events are usually longer (8-10 days) and the alternating relaxation periods are shorter (2-3 days) [*Huyer*, 1983; *Hickey et al.*, 2006; *Kudela et al.*, 2006; *Papastephanou et al.*, 2006]. These shorter periods of relaxation still allow Ω_{Ar} to return to baseline values (Ω_{Ar} ~2.1, see *Harris et al.* [2013]). However, sometimes the relaxation periods between upwelling events can be much shorter (<2 days) and Ω_{Ar} does not have the time to

return to baseline values before more low Ω_{Ar} water upwells to the surface [*Papastephanou et al.*, 2006]. For this reason, upwelling events closely followed by another upwelling event were omitted Ten events were selected using the above criteria from the years 2007-2009 and 2011 (Table 3.5.1) and ordered based on event start date.

Table 3.5.1. Upwelling Event Dates and Duration.

*Start date refers to the beginning of the upwelling event.

Event #	Start Date*	End Date	Duration
Event 1	4/21/09	4/26/09	6
Event 2	6/12/08	6/22/08	11
Event 3	6/21/08	7/6/08	16
Event 4	7/1/11	7/14/11	14
Event 5	7/3/08	7/24/08	21
Event 6	7/26/11	8/9/11	15
Event 7	8/3/08	8/10/08	8
Event 8	8/19/11	8/29/11	11
Event 9	8/23/07	9/5/07	14
Event 10	9/5/07	9/15/07	10

3.5.2.3. Modeling Post-Upwelling Inorganic Carbon System Changes

Because the field data from which this study stems were recorded at a stationary point (i.e. the NH-10 mooring), we must take an Eulerian model approach to study water passing across the field site instead of following an individual water mass. Our simple box model focuses on the changes in the inorganic carbon system that occur after strong upwelling-favorable winds begin to relax – i.e. the point at which high upwelled DIC values begin to decline to average surface water values of ~1990 mol kg^{-1} and low upwelled Ω_{Ar} values increase to baseline values of ~2.1 (see *Harris et al.* [2013]) – and what specific environmental mechanisms drive those changes back to baseline values. The influence of three environmental controlling mechanisms was tested

through this simple box model: NCP, mixing of upwelled water with California Current (CC) surface water and advection of the freshwater CR plume across NH-10, and air-sea CO_2 exchange.

To determine the point at which the chemical properties of NH-10 surface water began to restore to baseline values, a 30-hr low-pass filter was applied to the DIC and Ω_{Ar} data during each of these upwelling events. The 30-hr low-pass filter reduced the many short-term changes (<1 day) within each upwelling event as different water occupied the NH-10 site so that the major transitions could be determined. The point when the low-pass filtered DIC switched from increasing to decreasing (DIC_i) was defined as the starting point for modelling each selected upwelling event.

The DIC change ($\frac{\Delta DIC}{dt}$) was assumed to be the result of a combination of three processes:

$$\frac{\Delta DIC}{dt} = \frac{\Delta DIC_{gasex}}{dt} + \frac{\Delta DIC_{mix}}{dt} + \frac{\Delta DIC_{bio}}{dt} \tag{3.10}$$

where the contributions to $\frac{\Delta DIC}{dt}$ from air-sea gas exchange, mixing with either upwelled California Undercurrent (CU) or fresh riverine water, and net community production (NCP) are $\frac{\Delta DIC_{gasex}}{dt}$, $\frac{\Delta DIC_{mix}}{dt}$, and $\frac{\Delta DIC_{NCP}}{dt}$, respectively. The contribution to the observed rate of DIC change from air-sea gas exchange was calculated from the equation

$$\frac{\Delta DIC_{gasex}}{dt} = \frac{\frac{F_{gasex} \cdot 1000}{MLD \cdot \rho}}{dt} \tag{3.11}$$

where MLD is the mixed layer depth in meters and ρ is the density of seawater as calculated by *Millero and Poisson* [1981]. F_{gasex} is the air-sea CO_2 flux,

$$F_{gasex} = k \cdot S \cdot \Delta pCO_2 \quad (3.12)$$

where k is the gas transfer velocity calculated from wind speed [*Ho et al.*, 2011], S is the solubility of CO_2, and ΔpCO_2 is the difference between in situ pCO_2 and the average atmospheric value during the period studied of 392 µatm [*Evans et al.*, 2011].

Because salinity is a conservative property and differs between surface CC water, upwelled bottom water, the Columbia River plume and other freshwater sources, it was used to determine the mixing of water from each end-member at NH-10. These values were relative to CU water, the assumed dominant water mass present at NH-10 during the point of maximum upwelling [*Thomson and Krassovski*, 2010]. DIC_{mixing} and the contribution to total alkalinity (A_T) due to mixing ($A_{Tmixing}$) were determined by proportionally changing DIC and A_T based on changes in salinity using the equations:

$$DIC_{mixing} = DIC_{CU} - (S_{CU}\text{-}S_{meas}) / (S_{CU}\text{-}S_{shelf}) * (DIC_{CU}\text{-}DIC_{shelf}) \quad (3.13)$$

and

$$A_{Tmixing} = A_{TCU} - (S_{CU}\text{-}S_{meas}) / (S_{CU}\text{-}S_{shelf}) * (A_{TCU}\text{-}A_{Tshelf}) \quad (3.14)$$

where S_{CU} is the salinity calculated for the California Undercurrent, S_{meas} is the in situ salinity, S_{shelf}, DIC_{shelf}, and A_{Tshelf} are the surface water (depth<30m) means for S, DIC, and A_T from 2007 NACP West Coast Cruise (cdiac.ornl.gov), and $DIC_{CU,}$ A_{TCU}, $DIC_{shelf,}$ and A_{Tshelf}, are the DIC and A_T for the California Undercurrent and NH-10, respectively. For the 2007 NACP West Coast Cruise surface mean T=11.0°C, S=32.2, DIC=1990 µmol kg^{-1}, and A_T=2175 µmol kg^{-1} (cdiac.ornl.gov). California Undercurrent water typically has T=6.9°C, S=33.9 [*MacFadyen et al.*, 2008] , DIC=2220 µmol kg^{-1} [*van Geen et al.*, 2000], and A_T=2275 µmol kg^{-1} [*Hales et al.*,

2006]. During periods when S in events decreased to <30.0, the non-shelf end member was assumed to be fresh CR plume water and the following equations were used instead to determine DIC_{mixing} and $A_{Tmixing}$:

$$DIC_{mixing} = DIC_R - (S_R\text{-}S_{meas}) / (S_R\text{-}S_{shelf})*(DIC_R\text{-}DIC_{shelf}) \quad (3.15)$$

and

$$A_{Tmixing} = A_{TR} - (S_R\text{-}S_{meas}) / (S_R\text{-}S_{shelf})*(A_{TR}\text{-}A_{Tshelf}) \quad (3.16)$$

where S_R, DIC_R, and A_{TR} are the average S, DIC, and A_T for the CR plume (S=15, DIC=1350 μmol kg^{-1} [*Dahm et al.*, 1981], and A_T=1200 μmol kg^{-1} [*Berner and Berner*, 1987]), the predominant freshwater source to the shelf during summer upwelling [*Burla et al.*, 2010]. When S<30.0 in any event, equations 3.15 and 3.16 were used for modelling mixing contributions. When S>30.0, equations 3.13 and 3.14 were used to model the mixing component.

ΔDIC_{mixing} and $\Delta A_{Tmixing}$ were calculated using the following equations:

$$\frac{\Delta DIC_{mixing}}{dt} = \frac{DIC_i - DIC_{mixing}}{dt} \quad (3.17)$$

and

$$\frac{\Delta A_{Tmixing}}{dt} = \frac{A_{Ti} - A_{Tmixing}}{dt} \quad (3.18)$$

where DIC_i and A_{Ti} are the initial DIC and A_T at the start of modeling.

The contribution of NCP was assumed to be equal to the change in DIC not accounted for via air-sea gas exchange or mixing:

$$\frac{\Delta DIC_{NCP}}{dt} = \frac{\Delta DIC}{dt} - \frac{\Delta DIC_{gasex}}{dt} - \frac{\Delta DIC_{mixing}}{dt} \quad (3.19)$$

DIC_{mix} and A_{Tmix} were used along with measured T and S values to calculate Ω_{Ar} change due to mixing in CO2SYS [*Pierrot et al.,* 2006]. DIC_{gasex} was used with constant A_T to model the Ω_{Ar} change due to gas exchange. The Ω_{Ar} change due to NCP was calculated as the residual between observed Ω_{Ar} and modeled Ω_{Ar} change from mixing and gas exchange. There is some uncertainty associated with the mixing component for Ω_{Ar} due to the fact that it is calculated using two modeled parameters, DIC_{mix} and A_{Tmix}. This resulted in under-representation of Ω_{Ar} rate due to mixing when compared with the changes in DIC rate due to mixing.

Residual NCP was compared to NCP calculated based on satellite chl-a data and NH-10 solar radiation (NCP_{cal}) for events when satellite chl-a was available for the NH-10 location (events 1, 3, 5, and 6). Primary productivity (PP) was calculated using the equation by *Platt et al.* [1980]:

$$P(z)=Chl(z)\cdot(P_sChl^{-1})\cdot(1-e^{-\alpha I/P_sChl^{-1}})\cdot e^{-\beta I/P_sChl^{-1}} \quad (3.20)$$

where P(z) is the primary production at depth z, Chl(z) is the chl-a concentration at depth z, P_sChl is the chl-specific maximum rate of photosynthesis in the absence of photoinhibition , I is photosynthetically active radiation (PAR), α is the Chl-specific rate of light limited photosynthesis, and β is the Chl-specific photoinhibition parameter. Values for α, β, and P_sChl for temperate waters were taken from [*Harrison et al.*, 1985]. I was calculated as 45% of the solar radiation [*Harrison et al.*, 1985] from the pyranometer located on NH-10. NCP_{cal} was calculated by subtracting respiration (R) from PP. R was estimated to be between 24 to 72 mmol m^{-2} d^{-1} by minimizing the differences in fit between the observed ΔDIC and ΔDIC due to NCP_{cal} for each event. NCP_{cal} (mmol C m^{-2} d^{-1}) is then converted to mmol C m^{-3} d^{-1} by multiplying by the average MLD (m) during that event and to ^{1}μmol C kg^{-1} hr^{-1} by converting mmol C to μmol C, d^{-1} to hr^{-1}, and m^{-3} to kg using the density of seawater [ρ, *Millero and Poisson*, 1981]. The rate

of ΔDIC due to NCP was then calculated from converted NCP_{cal} and observed DIC at the start of the model:

$$\frac{\Delta DIC_{NCPcal}}{dt} = DIC_{NCP\ n-1} - \frac{NCP_n}{MLD} \quad (3.21)$$

where MLD is the mixed layer depth in m, *n* is the time elapsed (in hours) since the model was initiated and at $DIC_{NCP\ 1}$ is equal to the observed DIC at the start of the model. The rate of change in DIC_{cal} was similar to the rate of change modeled using DIC_{NCP} (see Table 3.5.2). Residual NCP was ultimately used in place of NCP_{cal} for all events because of cloud-limited coverage of the chl-a satellite data used in the calculation of NCP_{cal}. Specifically, chl-a satellite data was not available during periods of cloud cover at the NH-10 site during events 3, 4, 5, 7, and 10. The rate of DIC_{NCPcal} change was within 80-100% of the rate of DIC_{NCP} change.

Table 3.5.2. Comparison of ΔDIC_{NCP} residual and ΔDCI_{NCPcal} for events when satellite chl-a data was available.

Event #	ΔDIC_{NCP} residual ($\mu mol\ kg^{-1}\ d^{-1}$)	ΔDCI_{NCPcal} ($\mu mol\ kg^{-1}\ d^{-1}$)
Event 1	-4.86	-4.49
Event 2	-7.21	-7.23
Event 6	-17.56	-14.13
Event 8	-8.82	-7.49
Event 9	-6.94	-6.17

3.5.3. Results

Throughout the upwelling season, the Oregon Coast carbonate system is highly variable. Frequent upwelling brings high pCO_2, high DIC, and low Ω_{Ar} CU waters to the surface. Figures 3.5.1-4 show the pCO_2, DIC, Ω_{Ar}, UI, T, and S for the four years when carbonate system data was recorded during the summer, a subset of the data discussed by *Harris et al.* [2013]. Events

are numbered as listed in Table 3.5.1. During the ten selected upwelling events, pCO_2 ranged from 158 to 1337 µatm, DIC from 1617 to 2250 µmol kg^{-1}, and Ω_{Ar} from 0.7 to 3.8. Physical parameters varied greatly too. Upwelling indices were large and positive near the start of the events (up to 189 m^3 s^{-1} 100 m^{-1} coastline) but decreased to weaker upwelling or even downwelling-favorable conditions (down to -53 m^3 s^{-1} m^{-1} coastline) as carbonate and physical parameters returned to baseline values. T ranged from 7.55 to 17.33°C and s ranged from 23.50 to 33.71. Although parameters were highly variable throughout the upwelling season, the magnitude of the variation changed by event. The 10 events are discussed in order from smallest to largest magnitude carbonate system parameter changes.

Event 1 from late spring (Figure 3.5.1) had the smallest overall changes to the carbonate system. This event had a relatively high UI (Figure 3.5.1d) but resulted in relatively small pCO_2 changes from below ~230 µatm to above ~470 µatm (Figure 3.5.1a). DIC and Ω_{Ar} changes were, accordingly, also small compared to upwelling events later in the year (see Table 3.5.3). The initial, pre-upwelling DIC was around 1900 µmol kg^{-1} increasing only to 2040 µmol kg^{-1} during strongest upwelling before gradually decreasing to 1980 µmol kg^{-1} (Figure 3.5.1b). Before upwelling-favorable conditions began Ω_{Ar} was near 2.8 but decreased to 1.6 before returning to a pre-upwelling value of ~2.4. T and S changes were also relatively small; T ranged within 2.12 °C and S varied less than 1.00.

Table 3.5.3. The change in DIC and Ω_{Ar} during each upwelling event.

Event #	ΔDIC (μmol kg^{-1})	$\Delta\Omega_{Ar}$
Event 1	137	1.27
Event 2	512	3.05
Event 3	373	2.07
Event 4	425	1.33
Event 5	179	0.95
Event 6	303	2.43
Event 7	278	2.08
Event 8	288	2.33
Event 9	211	3.351
Event 10	253	1.36

Late summer/early autumn upwelling events 8 and 10 had slightly larger dynamics than event 1 in late spring. pCO_2 ranged from ~280 μatm to up between 500 and 600 μatm (Figure 3.5.4a). In these events DIC changed by up to 250 μmol kg^{-1} (Figure 3.5.4b), but the oscillations between high and low DIC gradually dampened from late August into September, with baseline DIC values by the end of event 10 near 1880 μmol kg^{-1}, nearly 80 μmol kg^{-1} higher than baseline DIC at the beginning of event 8 (Figure 3.5.4b). DIC dynamics at the end of August, 2011 showed a similar trend of decreasing ΔDIC over the course of event 9, although the baseline was near 1920 μmol kg^{-1} by the end of the event (Figure 3.5.3b), a significantly higher DIC baseline than in events 8 or 10. The overall change in DIC (see Table 3.5.3) in event 9 (late August 2011) was also smaller than for events 8 and 10 (August/September 2007), suggesting inter-annual changes in the DIC baseline. Ω_{Ar} values decreased from near 3.7 in events 8 and 10 (Figure 3.5.4c) and 3.3 in event 9 (Figure 3.5.3c) to around 1.5 (Figures 3.5.4c and 3.5.3c). Maximum upwelling indices during events 8-10 were <140 m^3 s^{-1} 100 m^{-1} coastline (Figure 3.5.3d and Figure 3.5.4d),

smaller than those during mid-summer. T and S changes were also relatively small compared to changes earlier in the summer (Figure 3.5.3e and Figure 3.5.4e).

Early and mid-summer upwelling events 2-7 (Figures 3.5.2 and 3.5.3) had considerably greater changes than either late spring or late summer/early autumn upwelling events (Table 3.5.3). Maximum upwelling indices were higher (up to 189 $m^3\ s^{-1}\ m^{-1}$ coastline) with the exception of events 3 and 7 (see Figures 3.5.2d and 3.5.3d). pCO_2 in events 2, 3, 5, and 7 ranged from <250 µatm to near 1200 µatm (Figure 3.5.2a). Initial values of DIC around 1780 µmol kg^{-1} increased to over 2130 µmol kg^{-1} during upwelling-favorable conditions (Figure 3.5.2b). High upwelling indices (Figure 3.5.2d) resulted in exceptionally low Ω_{Ar} (Figure 2c) for events 2-5, with $\Omega_{Ar}<1.0$ for periods of hours to a couple of days. Ω_{Ar} undersaturation also occurred during events 6-7; however, maximum UI during these events was <105 $m^3\ s^{-1}\ m^{-1}$ coastline (Figure 3.5.2c,d and 3.5.3c,d). These low Ω_{Ar} values were not sustained for as long as those in events 2-4. Following upwelling, Ω_{Ar} increased to maxima above 3.0 but remained highly variable (Figure 3.5.2c and 3.5.3c). S varied greatly during summer events 2-4 and reached particularly low values - as low as 23.50 following the weakening of upwelling-favorable conditions (Figure 3.5.2e and 3.5.3e).

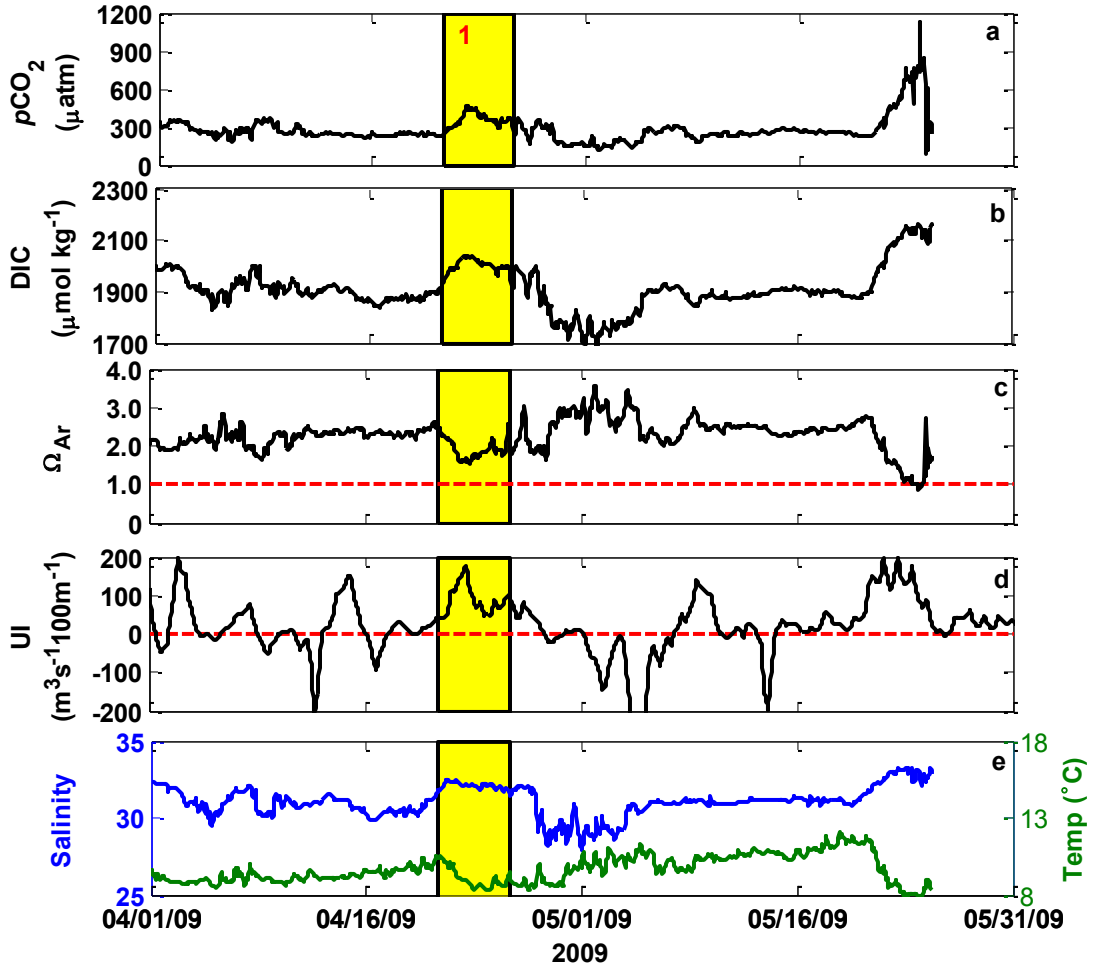

Figure 3.5.1. Spring 2009 with upwelling event 1 highlighted in yellow. (a) pCO_2. (b) DIC. (c) Ω_{Ar}. (d) Upwelling index, where positive values indicate upwelling-favorable conditions. (e) Salinity (blue) and temperature (green). The event number (red) corresponds to the events identified in Table 3.5.1. No data was collected for summer 2009.

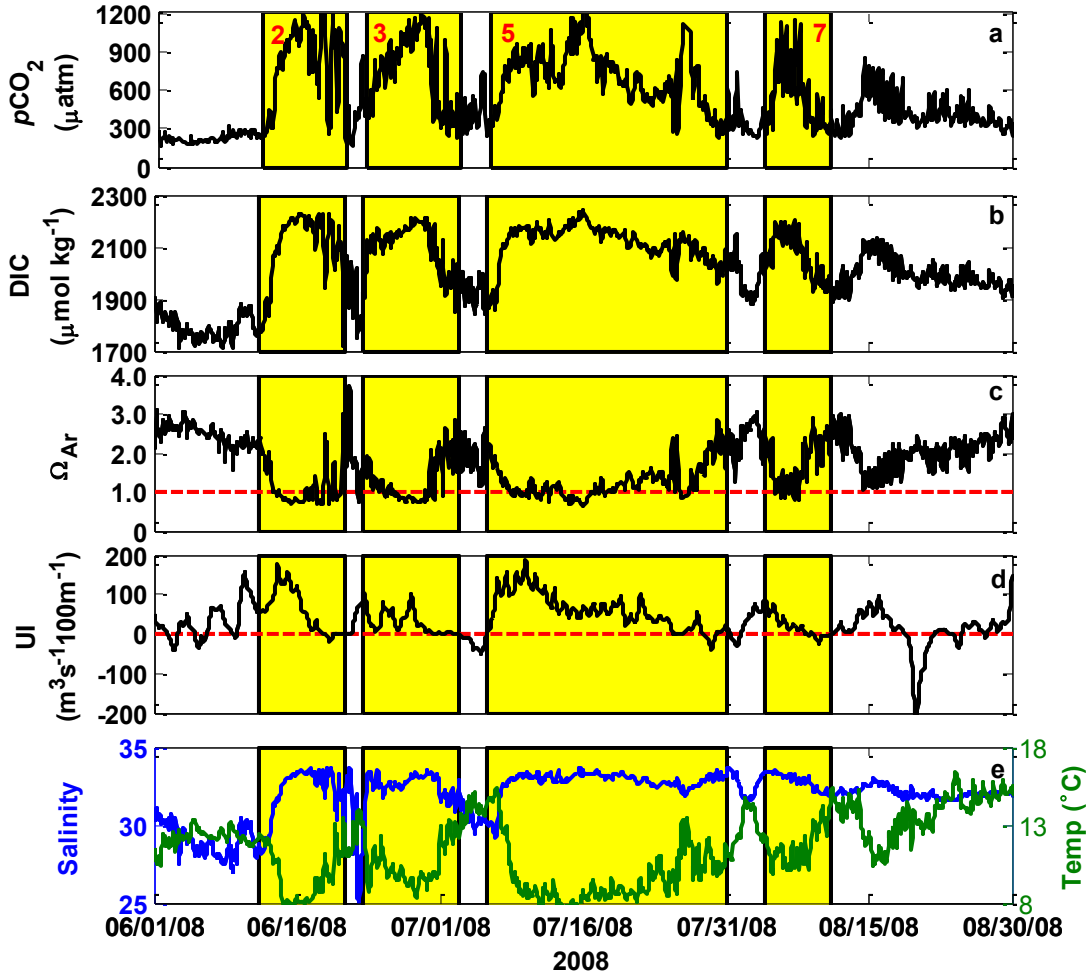

Figure 3.5.2. Summer 2008 with upwelling events 2,3,5, and 7 highlighted in yellow. (a) pCO_2. (b) DIC. (c) Ω_{Ar}. (d) Upwelling index, where positive values indicate upwelling-favorable conditions. (e) Salinity (blue) and temperature (green). The event numbers (red) correspond to the events identified in Table 3.5.1.

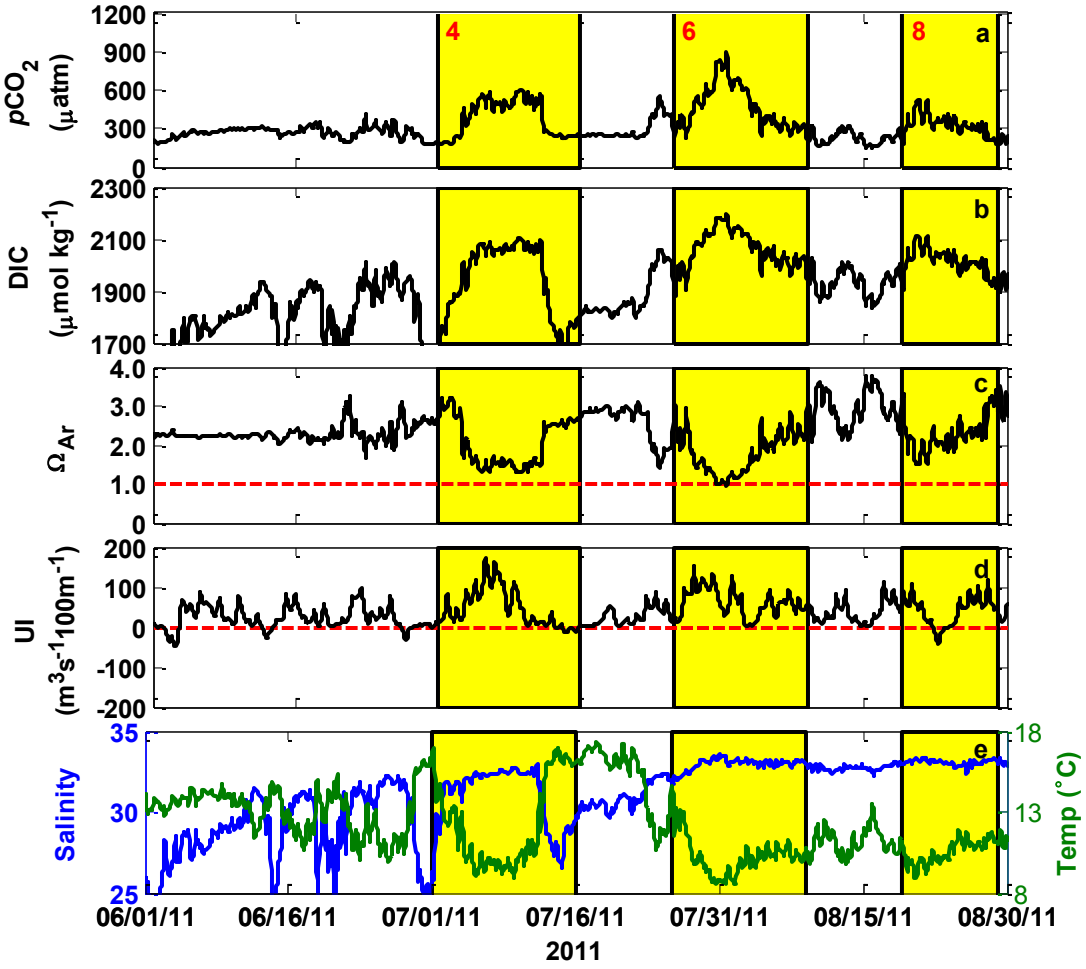

Figure 3.5.3. Summer 2011 with upwelling events 4,6, and 8 highlighted in yellow. (a) pCO_2. (b) DIC. (c) Ω_{Ar}. (d) Upwelling index, where positive values indicate upwelling-favorable conditions. (e) Salinity (blue) and temperature (green). The event numbers (red) correspond to the events identified in Table 3.5.1.

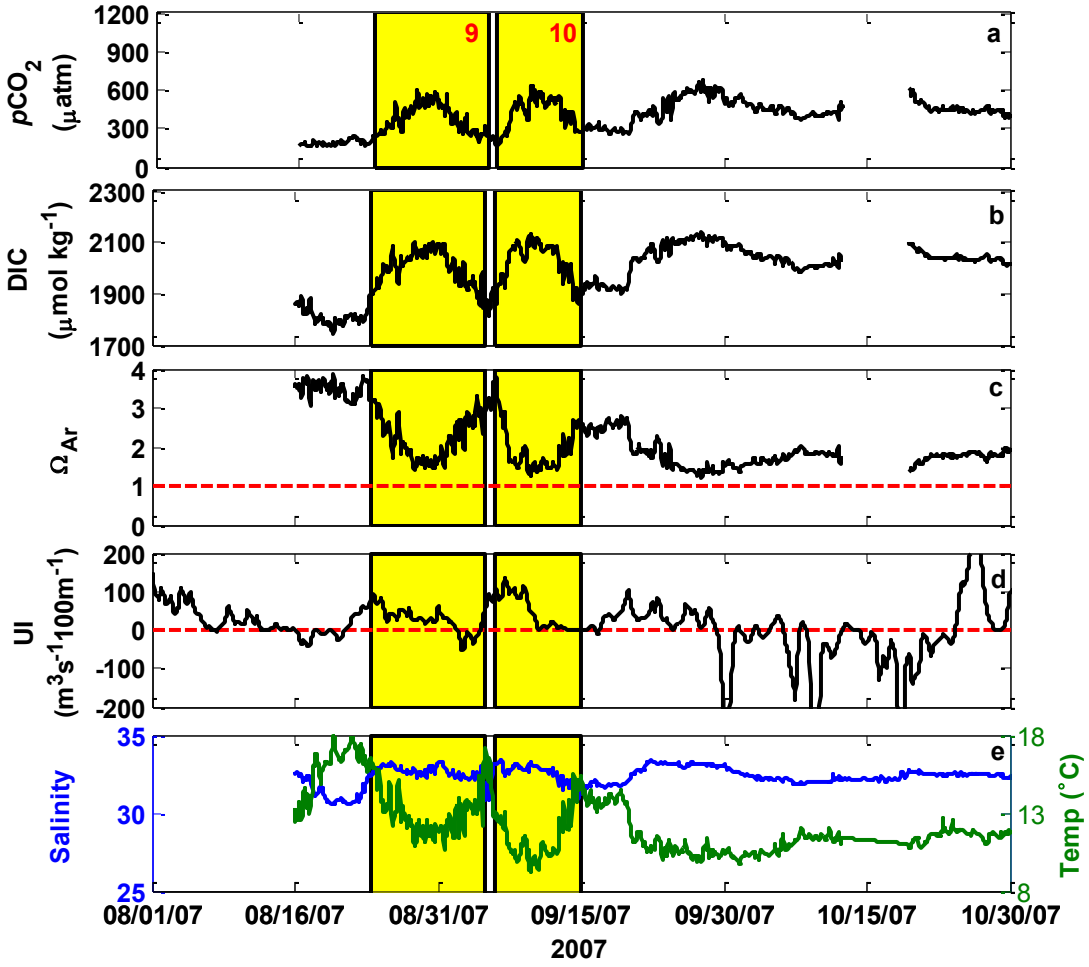

Figure 3.5.4. Late summer into early autumn of 2007 with upwelling events 9 and 10 highlighted in yellow. (a) pCO_2. (b) DIC. (c) Ω_{Ar}. (d) Upwelling index, where positive values indicate upwelling-favorable conditions. (e) Salinity (blue) and temperature (green). The event numbers (red) correspond to the events identified in Table 3.5.1.

To better understand the larger upwelling Ω_{Ar} dynamics, average Ω_{Ar} was calculated for the high initial values, lowest values, and high final values of each event (Figure 3.5.5). Several general trends are seen. During spring (Event 1) and late summer/early autumn (Events 8-10), average Ω_{Ar} prior to the start of upwelling was higher than Ω_{Ar} at the end of that event, whereas initial summer Ω_{Ar} was lower than or equal to the ending Ω_{Ar} (Events 2-7, Figure 3.5.5). The average minima Ω_{Ar} values were, in general, lower during the summer than they were during either spring or late summer/early autumn (Figure 3.5.5). In addition to seasonal change, some inter-

annual variation can be seen in Figure 3.5.5. Events 2, 3, 5, and 7 during 2008 have lower initial and end Ω_{Ar} means than Events 4, 6, and 8 during similar time periods in 2011.

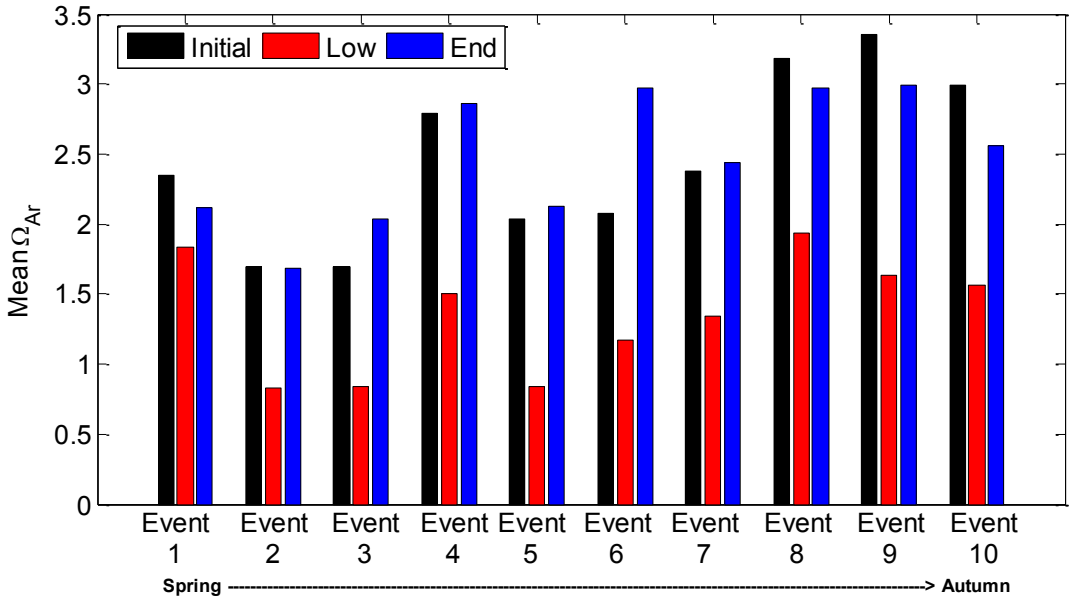

Figure 3.5.5. Average Ω_{Ar} calculated from four days surrounding the start of each upwelling event (black), the lowest Ω_{Ar} values during each upwelling event (red), and the high values at the end of each event (blue). Refer to Table 3.5.1 for event dates.

3.5.4. Discussion

3.5.4.1. Modeled DIC and Ω_{Ar}

To better understand which of the environmental controlling mechanisms had the strongest influence on the return from upwelling conditions to baseline DIC and Ω_{Ar} values, each DIC and Ω_{Ar} contribution were modeled starting from the relaxation of upwelling-favorable winds. Figures 3.5.6 and 3.5.7 show 30-hr low-pass filtered observed DIC and Ω_{Ar} compared to modeled components for mixing/advection, gas exchange, and residual NCP. DIC decrease and Ω_{Ar} increase during almost all of the events was primarily controlled by mixing/advection with

varying contributions from NCP. Event 6 (Figure 3.5.7a and f) was an exception; in this event nearly all of the changes in DIC and Ω_{Ar} were accounted for by the residual NCP from the modeled DIC and Ω_{Ar}. In all events air-sea CO_2 exchange had very little control over the changes in DIC or Ω_{Ar}.

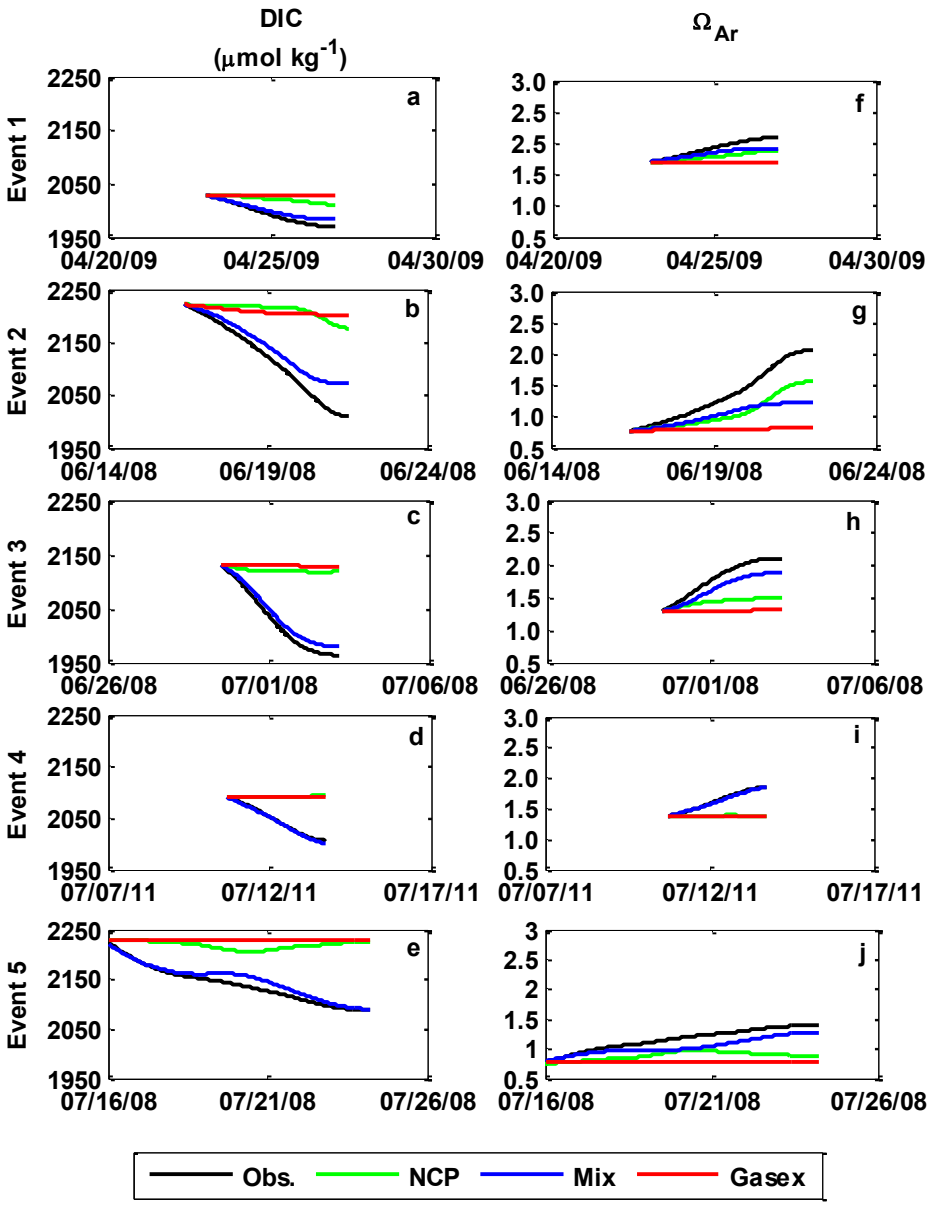

Figure 3.5.6. DIC (a-e) and Ω_{Ar} (f-j) observed values (black) and modeled contributions from mixing and/or advection (blue), air-sea CO_2 gas exchange (red), and residual NCP (green) for events 1-5.

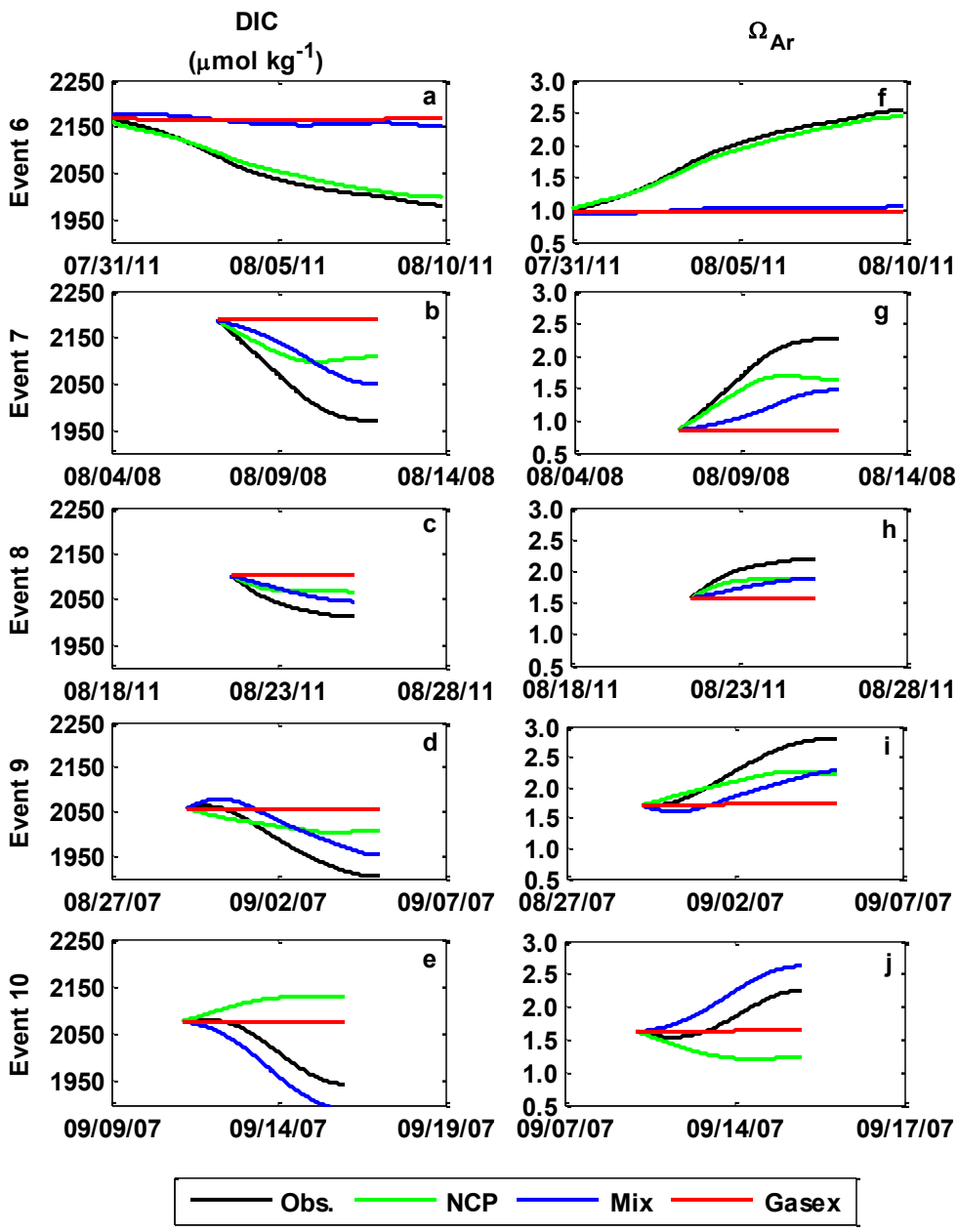

Figure 3.5.7. DIC (a-e) and Ω_{Ar} (f-j) observed values (black) and modeled contributions from mixing and/or advection (blue), air-sea CO_2 gas exchange (red), and residual NCP (green) for events 6-10.

The rates of DIC decrease and Ω_{Ar} increase following the relaxation of upwelling-favorable conditions were calculated from the 30-hr low-pass filtered observations in Figures 3.5.6 and 3.5.7. In addition, the rates for DIC and Ω_{Ar} change explained by each of the controlling

mechanisms were calculated. These results for DIC and Ω_{Ar} are shown in Figures 3.5.8 and 3.5.9, respectively. The highest rate of decrease (50 µmol kg^{-1} day^{-1}) was during event 2 and 7, while the lowest rates (between 15-20 µmol kg^{-1} day^{-1}) were during events 1, 5 and 6 (Figure 3.5.8). The other events had rates of DIC decrease between 23-45 µmol kg^{-1} day^{-1}.

The rates of Ω_{Ar} increase are shown in Figure 3.5.9. Qualitatively, the rates of observed Ω_{Ar} increase in each event are similar to the rates of observed DIC decrease. However, the relative contributions to the observed changes from mixing/advection and NCP vary between the DIC and Ω_{Ar} models (Figures 3.5.8 and 3.5.9). These differences are due to uncertainties in the model calculations for DIC_{mix} and A_{Tmix} that result in uncertainties in the Ω_{Ar} model calculations, as discussed in (section 3.5.2.3). Thus quantitative generalizations about each mechanism contributing to the observed Ω_{Ar} changes are discussed with caution.

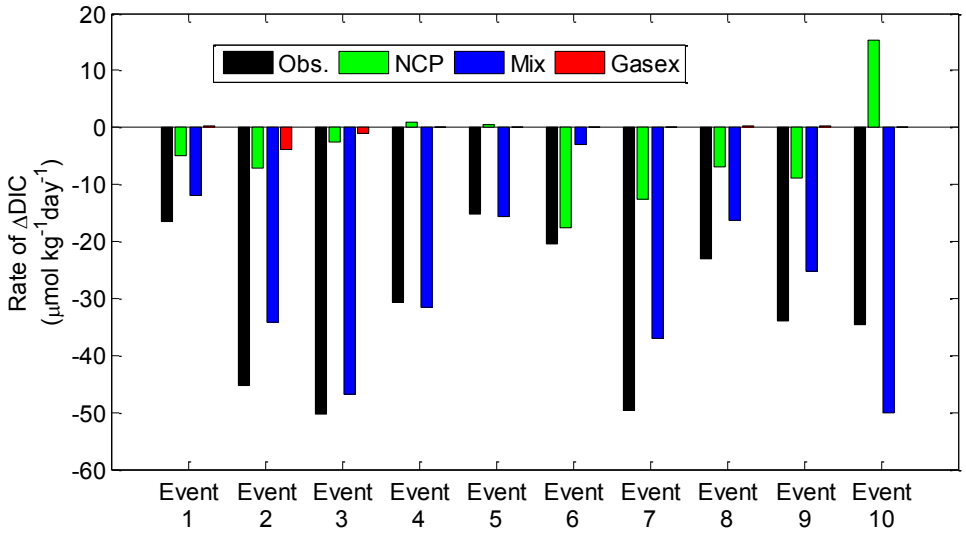

Figure 3.5.8. Rate of DIC change for each of the selected upwelling events. The observed rate of DIC decrease (black) and the rates of DIC change from residual NCP (green), modeled mixing/advection (blue), and modeled air-sea gas exchange (red).

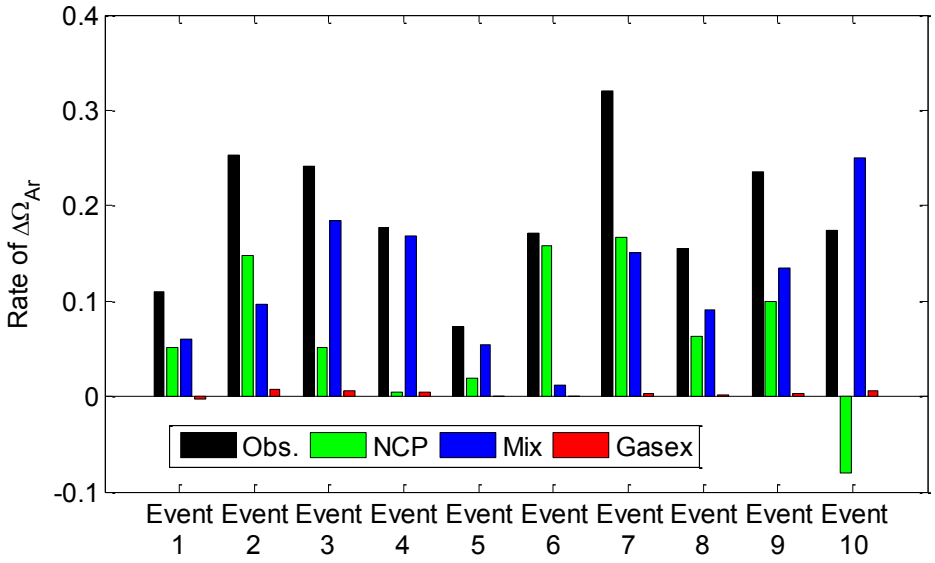

Figure 3.5.9. Rate of Ω_{Ar} change for each of the selected upwelling events. The observed rate of increase in Ω_{Ar} (black), changes from residual NCP (green), changes from the mixing/advection model (blue), and changes from air-sea gas exchange model (red).

3.5.4.2. Controls on Inorganic Carbon Changes

To better compare which controlling mechanisms had the greatest effect on observed DIC changes, the rates of DIC change due to NCP, mixing/advection, and gas exchange were calculated as a percentage of the observed rate of DIC change (Figure 3.5.10). The same technique was applied for the modeled rates of Ω_{Ar} change (Figure 3.5.11).

3.5.4.2.1. Mixing/advection

The primary controlling mechanism in almost all the events studied (with the exception of event 6) was mixing or advection. Most of the mixing occurred when recently-upwelled waters mix with CC surface water at the NH-10 site as upwelling-favorable conditions diminished. The mixing of upwelled CU water with CC surface water was characterized by small S changes corresponding to large DIC and Ω_{Ar} changes, such as those in events 1, 5, 6, and 8-10 (Figures

3.5.1- 3.5.4b,c,e). Larger Ω_{Ar} changes (Table 3.5.3) have a positive correlation (R^2=0.52, p<0.02) with greater mean UI prior to initiation of the model, as suggested by *Torres et al.* [2002] (Figure 3.5.12a). Stronger upwelling conditions brought the lowest Ω_{Ar} into shelf coastal waters and weaker UI brings shallower, higher Ω_{Ar} to the surface [*Torres et al.,* 2002]. The return to pre-upwelling baseline values was controlled by gradual mixing of the upwelled water with the lower DIC and S and higher Ω_{Ar} CC surface water.

Events 1, 5, 6, and 8-10 had smaller rates of DIC and Ω_{Ar} change due to mixing than events 2-4 and 7 (Figure 3.5.8 and 3.5.9), which had S near or <30.0, indicative of the low S CR plume (Figures 3.5.2e and 3.5.3e). The large rate of DIC and Ω_{Ar} change during these four events was a result of advection of the CR plume back and forth across the NH-10 site. Since in situ observations on the NH-10 mooring were fixed spatially, the rate of DIC decrease due to mixing of upwelled water with CC surface water was masked by the much larger rate of DIC decrease due to advection of the low DIC, low S CR plume across the NH-10 site. CR plume advection similarly affected the observed rate of Ω_{Ar} change, with the rate of Ω_{Ar} change due to mixing with higher Ω_{Ar} CC shelf water suppressed by advection of the lower Ω_{Ar} CR plume (Ω_{Ar}~1.8 compared to CC shelf water Ω_{Ar}~2.1) across the NH-10 mooring location. This also accounts for some of the discrepancy between the percent contribution of each controlling mechanism between DIC and Ω_{Ar} (Figures 3.5.10 and 3.5.11). Events 2-4 and 7 had the largest difference between the percent contribution of mixing/advection to observed rates in DIC and Ω_{Ar} change. The contribution of mixing to the observed Ω_{Ar} change was smaller than the mixing contributions to observed DIC changes in each of these events due to the low Ω_{Ar} CR plume suppressing the CC surface water contribution to Ω_{Ar} increase.

Hickey et al. [2005] found that downwelling conditions can push the CR plume into nearshore waters. During events 2-4 and 7 UI was initially high (~173, 103, 174 and 87 $m^3s^{-1}100\ m^{-1}$, respectively), but reached negative values during the post-upwelling period indicative of downwelling conditions (Figures 3.5.2e and 3.5.3e). These intermittent downwelling-favorable conditions during events 2-4 and 7 support the advection of the CR plume across the field site during these four events.

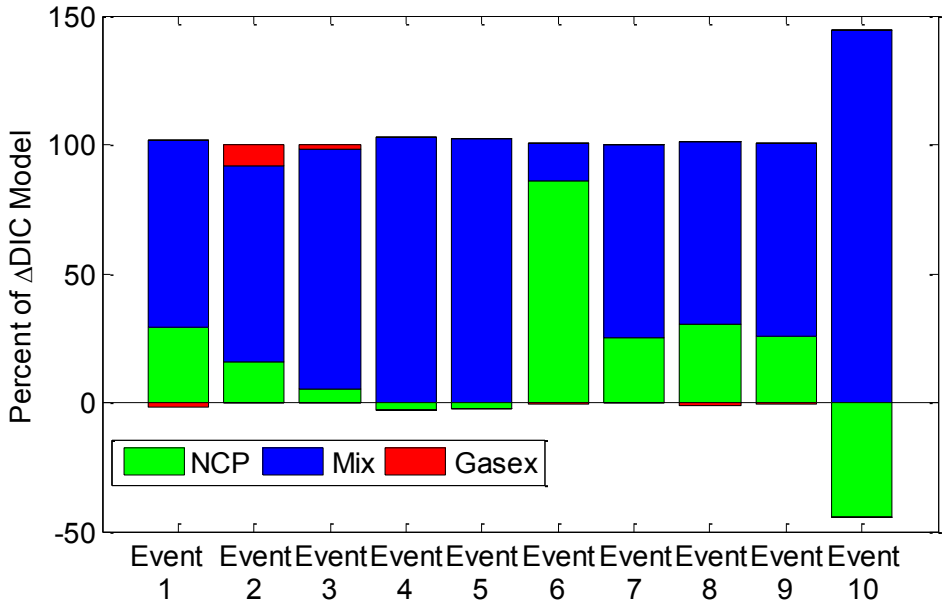

Figure 3.5.10. Percent contribution of NCP (green), mixing/advection (blue), and gas exchange (red) to the observed rate of DIC change.

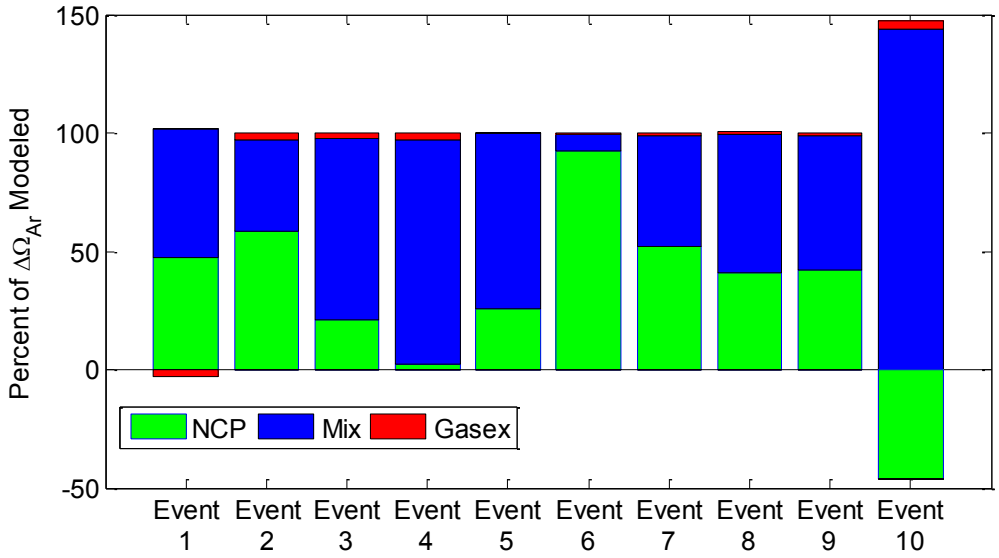

Figure 3.5.11. Percent contribution of NCP (green), mixing/advection (blue), and gas exchange (red) to the observed rate of DIC change.

3.5.4.2.2 Net Community Production

For the majority of the events, NCP contributed to the rate of DIC or Ω_{Ar} change by drawing down high DIC from upwelled waters, although in event 10, net respiration suppressed the overall decrease in DIC and increase in Ω_{Ar} caused by mixing (Figures 3.5.8- 3.5.11). With the exception of Event 6, NCP contributions DIC and Ω_{Ar} change were significantly smaller than mixing contributions (Figures 3.5.10 and 3.5.11).

During events 3-5, NCP contributed less than 5% to the observed change in DIC. *Dugdale et al.* [1990] found in a study of the relationships between nitrate and new production at upwelling centers that new production at Point Conception (California) did not fully realize its potential based on the concentrations of upwelled nitrate. In another study at Point Reyes (California) [*Dugdale et al.,* 2006], new production rates were again significantly lower than should result from utilization of initial upwelled nitrate. They suggest that this may be the result of high advective rates at the upwelling center, transporting biomass accumulation away from the study

site [*Dugdale et al.*, 1990] or due to inhibition by ammonium [*Dugdale et al.,* 2006]. For the Point Reyes study they additionally suggest infrequent wind relaxation at the study site may be the cause for low chl-a; i.e. without a relaxation in upwelling-favorable winds, there's no time for chl-a build-up at the study site [*Dugdale et al.,* 2006]. *Bianucci and Denman* [2012] suggest that a delay in the initiation of upwelling-favorable conditions at the beginning of the season can lead to reduced NCP in coastal Oregon waters. However, no correlation ($p>0.20$) was found in this study between CUI (indicative of the start and strength of upwelling conditions) and mean chl-a or the rate of Ω_{Ar} change due to NCP.

Another potential explanation for the low contributions of NCP to DIC and Ω_{Ar} changes comes from *Evans* [2011]. *Evans* [2011] combined the NH-10 pCO_2 data from event 5 in 2008 presented here with drifter and cruise pCO_2 data and satellite chl-a data found that low T, high S, and high pCO_2 indicative of upwelling persisted across the shelf and chl-a values remained low throughout the upwelling event. *Evans* [2011] hypothesized that because of persistent upwelling winds (see Figure 3.5.2d) during this period, upwelled water was advected off shelf and then quickly subducted before phytoplankton communities had time to respond to the nutrient-rich upwelled water. Thus the increase in Ω_{Ar} at the end of this persistent period of upwelling was likely more due to the relaxation of upwelling-favorable winds and a transition to downwelling-favorable winds that resulted in mixing with more productive offshore water than due to new production as a result of upwelled nutrients. It is likely that this advection-subduction process of nutrient-rich waters resulted in the negligible NCP contributions to DIC and Ω_{Ar} changes in events 3 and 4 as well.

3.5.4.2.3 Air-sea Gas Exchange

High pCO_2 at the surface during periods of upwelling leads to off-gassing which makes Oregon coastal waters a substantial CO_2 source during much of the upwelling season overall [*Evans et al.*, 2011]. However, due to the relatively slow rate of air-sea CO_2 exchange compared to the other factors contributing to DIC dynamics, the air-sea gas exchange had a small to negligible effect on post-upwelling DIC decrease and Ω_{Ar} increase, as expected [*Turi et al.,* 2013] (Figures 3.5.10 and 3.5.11). Pre-formed nutrients (the amount of nutrients in upwelled water mass the last time it was at the surface [*Friederich et al.*, 2008]) in the upwelled water allow pCO_2 to be drawn down below atmospheric values [*Hales*, 2005; *Fassbender et al.*, 2011]. This had the effect of greatly reducing the rates of air-sea gas exchange and results in the small contribution of gas exchange to changing DIC and Ω_{Ar} after upwelling.

3.5.4.3. Ω_{Ar} Undersaturation

Five of the selected upwelling events reached undersaturation: events 2, 3, 5, 6 and 7 (see Figures 3.5.2-3.5.4c). There were no significant correlations ($p>0.1$) between Ω_{Ar} undersaturation duration and mean NCP, change in salinity, mean Chl-a, start date, mean UI, or cumulative UI. This lack of correlation highlights the complexities of determining relationships between physical parameters and carbonate system controlling mechanisms.

A positive correlation ($R^2=0.58$, $p<0.02$) was found between the rate of Ω_{Ar} change from NCP and the UI mean prior the upwelling event, indicating that upwelled nutrients did have a small effect on NCP (Figure 3.5.12b). However, chl-a concentrations (for the upwelling events where satellite chl-a was available) had no correlation ($p>0.5$) with either UI prior or during each upwelling event. Ω_{Ar} change due to NCP was the smallest when winds prior to the event were weak. The rate of Ω_{Ar} change from mixing also correlated positively ($R^2=0.75$, $p<0.02$) with the

UI mean for the 8 days following initiation of the model (Figure 3.5.12c). The smallest rates of change from mixing occurred during relaxed conditions when the NCP contribution was larger, supporting the hypothesis by *Dugdale et al.* [2006] that chl-a has time to build up during relaxation. Longer duration events (those with longer periods of time between the relaxation of upwelling-favorable winds and the switch back to strong upwelling conditions) had a tenuous positive correlation (R^2=0.38, p<0.06) with chl-a means (Figure 3.5.12d). Satellite chl-a means were calculated for the 10km x 10km area surrounding the NH-10 mooring and so potentially captured chl-a blooms not specifically recorded in the DIC and Ω_{Ar} observations at NH-10. This may be the reason the rates in DIC and Ω_{Ar} change due to NCP do not have a significant correlation with chl-a mean.

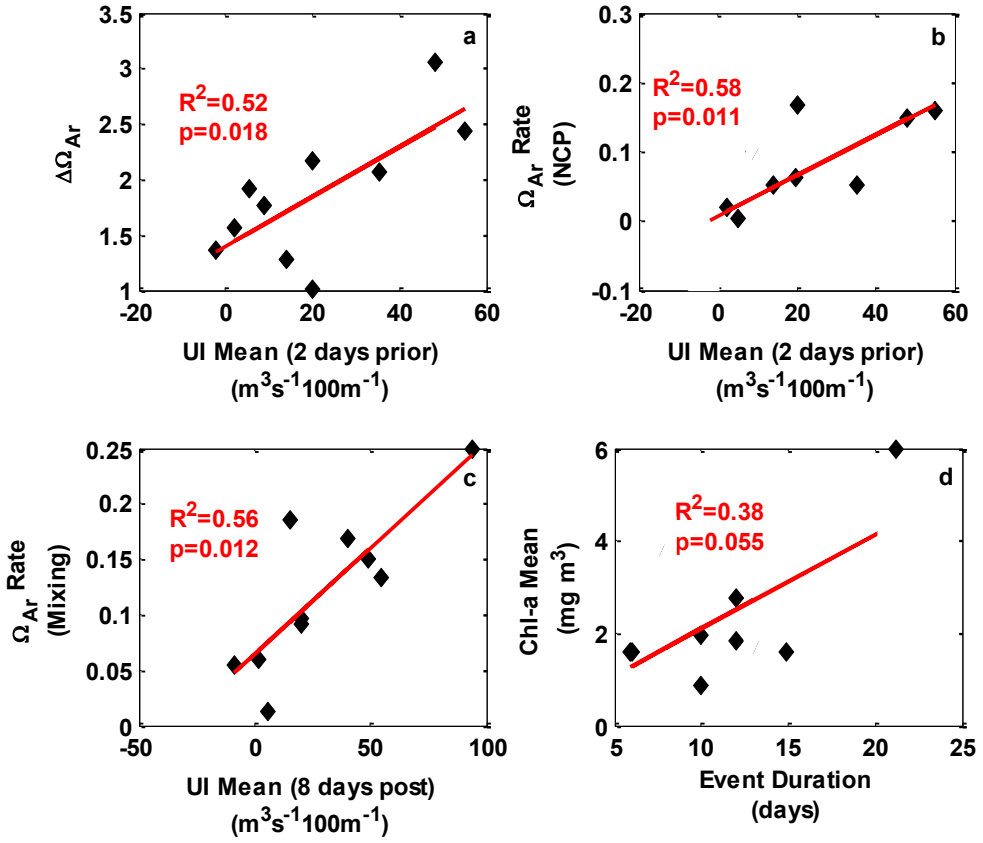

Figure 3.5.12. Correlations between the (a) overall change in Ω_{Ar} and the UI mean for the 2 days prior to the event, (b) Ω_{Ar} rate of change from NCP and the UI mean for the 2 days prior to the event, (c) Ω_{Ar} rate of change from mixing and UI mean for 8 days during the event, and (d) chl-a mean and the duration of the event.

3.5.4.4. Inter-annual Variation

There was some inter-annual variation between rates of DIC and Ω_{Ar} change**,** although this is hard to assess due to the majority of the events covered coming from two years only (2008 and 2011). However, events 2,3,5, and 7 in 2008 have higher observed rates for both DIC and Ω_{Ar} change than events 4, 6, 8, and 9 in 2011. Upwelling was stronger in 2008 [*Harris et al.,* 2013] than in 2011 and there is a very slight correlation (R^2=0.34, p<0.08 and R^2=0.38, p<0.06) between cumulative UI and the rate of DIC and Ω_{Ar} change due to mixing. Events during years

of stronger upwelling or later in the year had larger contributions from mixing. High C sinking rates as a result of advected phytoplankton blooms offshore earlier in the upwelling season results in remineralization of carbon in Oregon shelf bottom waters [*Turi et al.,* 2013]. Earlier initiation of the upwelling season and stronger upwelling (resulting in higher cumulative UI values) leads to larger reductions in Ω_{Ar} values in the bottom boundary layer [*Bianucci and Denman,* 2012]. This, in effect, primes the upwelling source water later in the upwelling season and leads to the large rates of change during these longer and stronger upwelling years.

3.5.5. Implications

The rate of both mixing/advection changes in Ω_{Ar} and NCP-driven changes in Ω_{Ar} are correlated with the strength of upwelling-favorable conditions. Strong upwelling results in the shelf surface waters being primed for biological production with nutrients, but continued intermittent high upwelling indices advect those waters away from NH-10 and baseline values are restored when upwelling conditions relax by mixing with CC surface water. Observed overall rates of DIC and Ω_{Ar} change did not correlate with wind conditions (either cumulative or during upwelling events), satellite chl-a, or S changes indicative of the CR plume. Neither did the duration of Ω_{Ar} undersaturation. The DIC and Ω_{Ar} changes in the majority of the events studied were primarily controlled by mixing/advection, but this is in part a limitation of the Eulerian nature of a mooring-based study. More spatially-diverse observations and further study are needed to capture carbonate system dynamics during additional upwelling events to more accurately link controlling mechanisms to physical parameters.

An understanding of these controlling mechanisms and their links to physical parameters is important as the changing global climate will impact these secondary controlling mechanisms

and likewise the carbonate system. Upwelling strength and duration is predicted to increase along the CCS [*Bakun*, 1990; *Schwing and Mendelssohn*, 1997]. More frequent and stronger upwelling events will bring more high DIC, low Ω_{Ar} water to the shelf, but shorter periods between upwelling events could decrease the potential for chl-a build-up and affect the rate at which carbonate system parameters return to pre-upwelling values. In addition, predicted increases in major precipitation events over the CR watershed [*Mass et al.*, 2011] and a predicted increase in annual CR water-basin runoff [*Elsner et al.*, 2010] could increase the influence of the CR plume on shelf carbonate system dynamics. Since an increase in the frequency and duration of low Ω_{Ar} periods may have detrimental effects on shelf biota [*Gazeau et al.*, 2007; *Barton et al.*, 2012; *Comeau et al.*, 2012], it is important to continue to study the factors contributing to carbonate system dynamics in these highly productive regions.

CHAPTER 4

Conclusions

Long-term, high-temporal resolution observations of the inorganic carbon system are essential for studying the natural range and controlling mechanisms of Ω_{Ar}. The California Current System coastal upwelling zone has already seen a change in Ω_{Ar} range since the industrial revolution due to anthropogenic ocean acidification. The range of Ω_{Ar} has decreased by approximately 0.52 since pre-industrial times and water with Ω_{Ar} as low as 0.66 reaches surface waters. Undersaturated water is present in shelf bottom waters 30% of the time as opposed

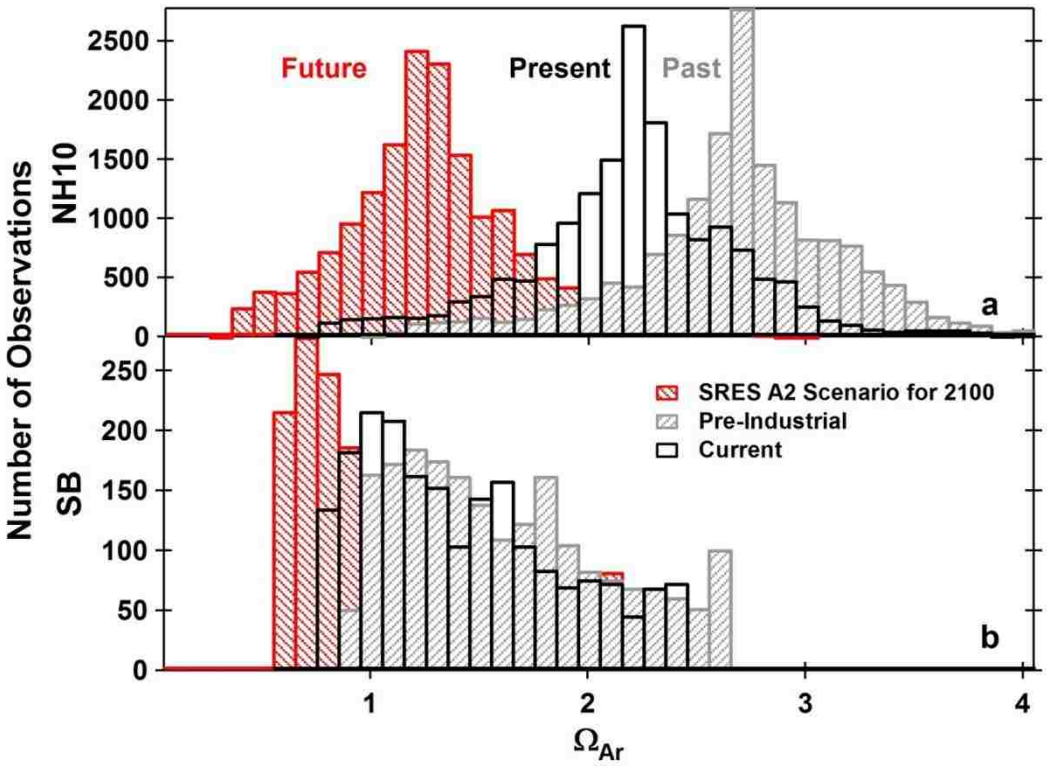

Figure 4.1. Predicted Ω_{Ar} for NH-10 (a) and the shelf break (b) for the year 2100 under the SRES A2 emissions scenario (Future) [*Nakicenovic et al.*, 2000] compared to previously-discussed estimates for the year 1850 (Past) and observations from between 2007-2011 (Present).

to 10% during the pre-industrial period. Using the same method for predicting NH-10 and shelf break Ω_{Ar} as described in section 3.4.2.2 but with atmospheric CO_2 predictions for the year 2100 (using the SRES A2 emissions scenario [*Nakicenovic et al.*, 2000]), the 2100 range of Ω_{Ar} for NH-10 surface and shelf break bottom waters was calculated (Figure 4.1, red bars). Mean surface Ω_{Ar} has decreased by ~1.0 and rarely reaches saturations states above 2.0. shelf break bottom waters are undersaturated 59% of the time (Figure 4.1) and mean surface Ω_{Ar} is 1.1, barely above saturation.

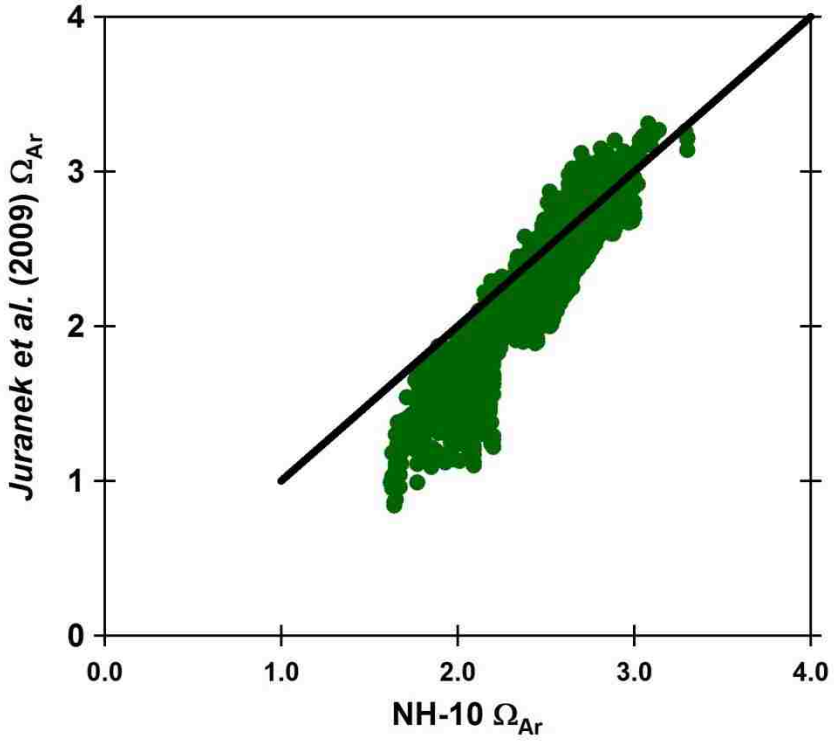

Figure 4.2. Comparison of field Ω_{Ar} observations to Ω_{Ar} calculated using the *Juranek et al.,* 2009 relationship (green). 1 to 1 line (black).

In situ Ω_{Ar} observations can be compared to methods of Ω_{Ar} calculation, such as those by *Juranek et al.,* [2009] (Figure 4.2) and *Alin et al.,* [2012]. The *Juranek et al.* [2009] relationship

uses an algorithm driven by O_2 and T measurements to calculate Ω_{Ar}. Although the algorithm was determined for water below 30 m, the predicted Ω_{Ar} above 2.2 matched the in situ observations pretty closely. Below Ω_{Ar}=2.2, the algorithm predicted significantly lower Ω_{Ar} than the in situ values (off by an average of 0.4). Different rates of gas-exchange between O_2 and pCO_2 accounted for the offset in the recently-upwelled, lower Ω_{Ar} water. However, the comparison between observed and predicted Ω_{Ar} suggest that the relationship works well for non-upwelled surface waters; i.e. waters that have been at the surface for long enough for gas-exchange rates for O_2 and pCO_2 to even out. In upwelling regions like the Oregon coastal upwelling zone, however, inorganic carbon parameter measurements still provide more accurate calculations of Ω_{Ar}.

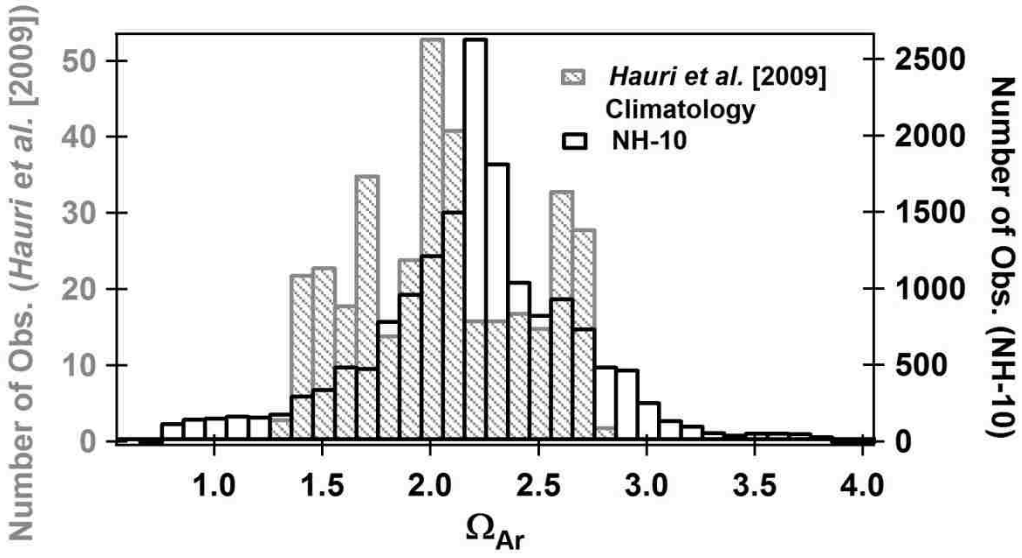

Figure 4.3. The range of observed NH-10 Ω_{Ar} compared to Ω_{Ar} modeled using the pH and pCO_2 climatologies from the ROMS model described in *Hauri et al.,* 2009.

Modeling systems like the eddy-resolving Regional Oceanic Modeling System (ROMS) used by *Hauri et al.* (2009) and *Gruber et al.* [2012] can provide detailed predictions of carbonate system changes across an entire current system. However, there is always room for improvement in

these models as our knowledge of the region increases. Figure 4.3 compares Ω_{Ar} observed at NH-10 to values calculated from ROMS-driven pH and pCO_2 climatologies (from *Hauri*, personal communication 2011). The model predicts slightly lower mean Ω_{Ar} (2.0) compared to the shelf (2.2), but the main difference is in the range of Ω_{Ar}. The model predicts a much smaller range in Ω_{Ar}, from 1.3 to 2.8 and does not predict the undersaturation observed at NH-10. The influence of inter-annual wind variation and Columbia River plume location are not incorporated in the model, but analysis of NH-10 Ω_{Ar} observations conclude that the plume location plays an important role in driving Ω_{Ar} variation during the spring and summer and inter-annual wind variability influences inter-annual changes in mean Ω_{Ar}. Adding seasonal changes in Ω_{Ar} controlling mechanisms could contribute to more accurate predictions of future Ω_{Ar} in these economically and ecologically important coastal upwelling zones.

References:

Alin, S.R., R.A. Feely, A.G. Dickson, J.M. Hernandez-Ayon, L.W. Juranek, M.D. Ohman, and R. Goericke (2012). Robust empirical relationships for estimating the carbonate system in the southern California Current System and application to CalCOFI hydrographic cruise data (2005-2011), *Journal of Geophysical Research-Oceans 117*, C05033. doi: 10.1029/2011JC007511.

Allen, J.S. (1973), Upwelling and coastal jets in a continuously stratified ocean, *Transactions-American Geophysical Union, 54*(4), 314.

Antoine, D.E. (2004), *International Ocean Colour Coordinating Group (IOCCG) Report 4.* [online] Available from http://www.ioccg.org

Bakun, A. (1990), Global climate change and intensification of coastal ocean upwelling, *Science, 247*(4939), 198-201, doi: 10.1126/science.247.4939.198.

Bandstra, L., B. Hales, and T. Takahashi (2006), High-frequency measurement of seawater total carbon dioxide, *Marine Chemistry, 100*, 24-38, doi:10.1016/j.marchem.2005.10.009.

Barton, A., B. Hales, G.G. Waldbusser, C. Langdon, and R.A. Feely (2012), The Pacific oyster *Crassostrea gigas*, shows negative correlation to naturally elevated carbon dioxide levels: Implications for near-term ocean acidification effects, *Limnology and Oceanography, 57*(3), 698-710, doi:10.4319/lo.2012.57.3.0698.

Bates, N.R., J.T. Mathis, and L.W. Cooper (2009), Ocean acidification and biologically induced seasonality of carbonate mineral saturation states in the western Arctic Ocean, *Journal of Geophysical Research, 114*(C11), 1-21, doi: 10.1029/2008JC004862.

Bates, N.R., M.H.P. Best, K. Neely, R. Garley, A.G. Dickson, and R.J. Johnson (2012), Detecting anthropogenic carbon dioxide uptake and ocean acidification in the North Atlantic Ocean, *Biogeosciences, 9*(7), 2059-2522, doi: 10.5194/bg-9-2509-2012.

Bednaršek, N. G.A. Tarling, D.C.E. Bakker, S. Fielding, E.M. Jones, H.J. Venables, P. Ward, A. Kuzirian, B. Lézé, R.A. Feely, and E.J. Murphy (2012), Extensive dissolution of live pteropods in the Southern Ocean, *Nature Geoscience, 5*(12), 881-885, doi: 10.1038/ngeo1635.

Berner, K.B., and R. A. Berner (1987), *The Global Water Cycle: Geochemistry and Environment*, Prentice-Hall, Upper Saddle River, New Jersey.

Bianucci, L., and K. Denman (2012), Carbon and oxygen cycles: Sensitivity to changes in environmental forcing in a coastal upwelling system, *Journal of Geophysical Research, 117*(G1), 1-13, doi: 10.1029/2011JG001849.

Borges, A.V., and M. Frankignoulle (2002), Aspects of dissolved inorganic carbon dynamics in the uwpelling system off the Galician coast, *Journal of Marine Systems, 32*(1-3), 181-198 doi: 10.1016/S0924-7963(02)00031-3.

Burla, M., A.M. Baptista, Y. Zhang, and S. Frolov (2010), Seasonal and interannual variability of the Columbia River plume: A perspective enabled by multiyear simulation databases, *Journal of Geophysical Research, 115*, C00B16, doi: 10.1029/2008JC004964.

Byrne, M., M. Ho, P. Selvakumaraswamy, H.D. Nguyen, S.A. Dworjanyn, and A.R. Davis (2009), Temperature, but not pH, compromises sea urchin fertilization and early development under near-future climate change scenarios, *Proceedings of the Royal Society B, 276*(1663), 1883-1888, doi: 10.1098/ rspb.2008.1935.

Caldeira, K. and M.E. Wickett (2003), Oceanography:anthropogenic carbon and ocean pH, *Nature, 425*(6956), 365, doi: 10.1038/425365a.

Canadell, J.G., C. Le Quéré, M. R. Raupach, C. B. Field, E. T. Buitenhuis, P. Ciais, T. J. Conway, N. P. Gillett, R. a Houghton, and G. Marland (2007), ontributions to accelerating atmospheric CO2 growth from economic activity, carbon intensity, and efficiency of natural sinks, *Proceedings of the National Academy of Sciences of the United States of America, 104*(47), 18866-18870, doi: 10.1073/pnas.0702737104.

Cao, Z., M. Dai, N. Zheng, D. Wang, Q. Li, W. Zhai, F. Meng, and J. Gan (2011), Dynamics of the carbonate system in a large continental shelf system under the influence of both a river plume and coastal upwelling, *Journal of Geophysical Research, 116*(G2), G02010, doi: 10.1029/2010JG001596.

Chavez, F., Takahashi, T. Coastal Oceans. *The First State of the Carbon Cycle Report*. 2007. (accessed 3/2010). http://cdiac.ornl.gov/SOCCR/pdf/aboutsoccr.pdf

Chavez, F. P., and M. Messié (2009), A comparison of Eastern Boundary Upwelling Ecosystems, *Progress In Oceanography*, *83*(1-4), 80–96, doi:10.1016/j.pocean.2009.07.032.

Chierici, M., and a. Fransson (2009), Calcium carbonate saturation in the surface water of the Arctic Ocean: undersaturation in freshwater influenced shelves, *Biogeosciences*, *6*(11), 2421–2431, doi:10.5194/bg-6-2421-2009.

Clayton, T. D., and R. H. Byrne (1993), Spectrophotometric seawater pH measurements: total hydrogen ion concentration scale calibration of m-cresol purple and at-sea results, *Deep-Sea Research. I, 40,* 2115–2129.

Conway, T. J., P.P. Tans, L.S. Waterman, K.W. Thoning, D.R. Kitzis, K.A. Masarie, and N. Zhang (1994) Evidence for inter-annual variability of the carbon cycle from the National Oceanic and Atmospheric Administration/Climate Monitoring and Diagnostics Laboratory

Global Air Sampling Network, *Journal of Geophysical Research, 99*, 22831–22855, doi:10.1029/94JD01951.

Doney, S., W. Balch, V. Fabry, and R. Feely (2009a), Ocean acidification: a critical emerging problem for the ocean sciences, *Oceanography*, *22*(4), 16–25, doi:10.5670/oceanog.2009.93.

Doney, S. C., V. J. Fabry, R. a. Feely, and J. a. Kleypas (2009b), Ocean acidification: the other CO_2 problem, *Annual Review of Marine Science*, *1*(1), 169–192, doi:10.1146/annurev.marine.010908.163834.

Dore, J.E., R. Lukas, D.W. Sadler, M.J. Church, and D.M. Karl (2009), Physical and biogeochemical modulation of ocean acidification in the central North Pacific., *Proceedings of the National Academy of Sciences of the United States of America*, *106*(30), 12235–40, doi:10.1073/pnas.0906044106.

Dugdale, R. C., E. P. Wilkerson, and A. Morel (1990), Realization of new production in coastal upwelling areas: a means to compare relative performance, *Limnoogy and Oceanography, 35*, 822–829.

Dugdale, R. C., F. P. Wilkerson, V. E. Hogue, and A. Marchi (2006), Nutrient controls on new production in the Bodega Bay, California, coastal upwelling plume, *Deep Sea Research, Part II, 53*, 3049–3062, doi:10.1016/j.dsr2.2006.07.009.

Dugdale, R.C., F.P. Wilkerson, and A. Morel (2013), Realization of new production in coastal upwelling areas: a means to compare relative performance, *Limnology and Oceanography, 35*(4), 822–829, doi:10.4319/ lo.1990.35.4.0822.

Dupont, S., B. Lundve, and M. Thorndyke (2010), Near future ocean acidification increases growth rate of the lecithotrophic larvae and juveniles of the sea star *Crassaster papposus*, *Journal of Experimental Zoology, Part B., 314B*(5), 382–389, doi:10.1002/jezmde.21342.

Egleston, E. S., C. L. Sabine, and F. M. M. Morel (2010), Revelle revisited: buffer factors that quantify the response of ocean chemistry to changes in DIC and alkalinity, *Global Biogeochemical Cycles*, *24*(1), n/a–n/a, doi:10.1029/2008GB00340.

Elsner, M. M., L. Cuo, N. Voisin, J. S. Deems, A. F. Hamlet, J. A. Vano, K. E. B. Mickelson, S.-Y. Lee, and D. P. Lettenmaier (2010), Implications of 21st century climate change for the hydrology of Washington State, *Climatic Change*, *102*(1-2), 225–260, doi:10.1007/s10584-010-9855-0.

Evans, W. (2010), *Sea-air carbon dioxide flux variability on the Northeast Pacific* (doctoral dissertation), Oregon State University, ProQuest, UMI Dissertations Publishing, 2011. 3464400.

Evans, W., B. Hales, and P. G. Strutton (2011), Seasonal cycle of surface ocean p CO 2 on the Oregon shelf, *Journal of Geophysical Research*, *116*(C5), C05012, doi:10.1029/2010JC006625.

Fabry, V. J., B. A. Seibel, R. A. Feely, and J. C. Orr (2008), Impacts of ocean acidification on marine fauna and ecosystem processes, *ICES Journal of Marine Science, 65*(3), 414–432, doi:10.1093/icesjms/fsn048.

Fassbender, A. J., C. L. Sabine, R. a. Feely, C. Langdon, and C. W. Mordy (2011), Inorganic carbon dynamics during northern California coastal upwelling, *Continental Shelf Research*, *31*(11), 1180–1192, doi:10.1016/j.csr.2011.04.006.

Feely, R. A. et al. (2002), In situ calcium carbonate dissolution in the Pacific Ocean, *Global Biogeochemical Cycles*, *16*(4), 1–12, doi:10.1029/2002GB001866.

Feely, R. A., C. L. Sabine, J. M. Hernandez-ayon, D. Ianson, and B. Hales (2008), Evidence for upwelling of corrosive "acidified" water onto the continental shelf, *Science*, *320*(5882), 1490–1492, doi:10.1126/ science.1155676.

Feely, R. A., S. C. Doney, and S. R. Cooley (2009), Ocean Acidification, *Oceanography*, *22*(4), 172–181, doi:10.5670/oceanog.2009.106.

Feely, R. A., S. R. Alin, J. Newton, C. L. Sabine, M. Warner, A. Devol, C. Krembs, and C. Maloy (2010), The combined effects of ocean acidification, mixing, and respiration on pH and carbonate saturation in an urbanized estuary, *Estuarine, Coastal and Shelf Science*, *88*(4), 442–449, doi:10.1016/j.ecss.2010.05.004.

Friederich, G. E., J. Ledesma, O. Ulloa, and F. P. Chavez (2008), Air–sea carbon dioxide fluxes in the coastal southeastern tropical Pacific, *Progress In Oceanography*, *79*(2-4), 156–166, doi:10.1016/j.pocean.2008.10.001.

Gazeau, F., C. Quiblier, J. M. Jansen, J.-P. Gattuso, J. J. Middelburg, and C. H. R. Heip (2007), Impact of elevated CO_2 on shellfish calcification, *Geophysical Research Letters*, *34*(7), L07603, doi:10.1029/2006GL028554.

van Geen, A., R. K. Takesue, J. Goddard, T. Takahashi, J. A. Barth, and R. L. Smith (2000), Carbon and nutrient dynamics during coastal upwelling off Cape Blanco, Oregon, *Deep Sea Research Part II: Topical Studies in Oceanography*, *47*(5-6), 975–1002, doi:10.1016/S0967-0645(99)00133-2.

Gray, S. E. C., M. D. DeGrandpre, T. S. Moore, T. R. Martz, G. E. Friederich, and K. S. Johnson (2011), Applications of in situ pH measurements for inorganic carbon calculations, *Marine Chemistry*, *125*(1-4), 82–90, doi:10.1016/j.marchem.2011.02.005.

Gray, S. E. C., M. D. DeGrandpre, C. Langdon, and J. E. Corredor (2012), Short-term and seasonal pH, pCO_2 and saturation state variability in a coral-reef ecosystem, *Global Biogeochemical Cycles*, *26*(3), n/a–n/a, doi:10.1029/2011GB004114.

Green, M.A., G.G. Waldbusser, S.L. Reilly, K. Emerson, and S. O'Donnell (2009), Death by dissolution: sediment saturation state as a mortality factor for juvenile bivalves, *Limnology and Oceanography, 54*(4), 1037-1047, doi: 10.4319/lo.2009.54.4.1037.

Green, M. A., G. G. Waldbusser, L. Hubazc, E. Cathcart, and J. Hall (2012), Carbonate mineral saturation state as the recruitment cue for settling bivalves in marine muds, *Estuaries and Coasts*, *36*(1), 18–27, doi:10.1007/s12237-012-9549-0.

Gruber, N., C. Hauri, Z. Lachkar, D. Loher, T. L. Frölicher, and G.-K. Plattner (2012), Rapid progression of ocean acidification in the California Current System., *Science (New York, N.Y.)*, *337*(6091), 220–3, doi:10.1126/science.1216773.

Hales, B., J. N. Moum, P. Covert, and A. Perlin (2005a), Irreversible nitrate fluxes due to turbulent mixing in a coastal upwelling system, *Journal of Geophysical Research*, *110*, C10S11, doi:10.1029/2004JC002685.

Hales, B., T. Takahashi, and L. Bandstra (2005b), Atmospheric CO2 uptake by a coastal upwelling system, *Global Biogeochemical Cycles, 19*, GB1009, doi:10.1029/2004GB002295.

Hales, B., L. Karp-Boss, A. Perlin, and P. A. Wheeler (2006), Oxygen production and carbon sequestration in an upwelling coastal margin, *Global Biogeochemical Cycles*, *20*(3), 1–15, doi:10.1029/2005GB002517.

Harris, K. E., M. D. DeGrandpre, and B. Hales (2013), Aragonite Saturation State Dynamics in a Coastal Upwelling Zone, *Geophysical Research Letters*, *40*(1-6), doi:10.1002/grl.50460.

Harrison, W. G., T. Platt, and M. R. Lewis (1985), The utility of light-saturation models for estimating marine primary productivity in the field: a comparison with conventional "simulated " in situ methods, *Canadian Journal of Fisheries and Aquatic Science*, *42*, 864-872.

Haugan, P. M., and H. Drange (1996), Effects of CO_2 on the ocean environment, *Energy Conversion and Management*, *37*(6-8), 1019–1022, doi:10.1016/0196-8904(95)00292-8.

Hauri, C., N. Gruber, G.-K. Plattner, S. Alin, R. Feely, B. Hales, and P. Wheeler (2009), Ocean Acidification in the California Current System, *Oceanography*, *22*(4), 60–71, doi:10.5670/oceanog.2009.97.

Hauri, C., N. Gruber, M. Vogt, S.C. Doney, R.A. Feely, Z. Lachkar, A. Leinweber, A.M.P. McDonnell, M. Munnich, and G-K. Plattner (2013), Spatiotemporal variability and long-

term trends of ocean acidification in the California Current System, *Biogeosciences, 10,* 193-216, doi:10.5194/bg-10-193-2013.

Hickey, B.M. (1979), The California Current—hypotheses and facts, *Progress in Oceanography, 8,* 191–279.

Hickey, B., S. Geier, N. Kachel, and A. MacFadyen (2005), A bi-directional river plume: The Columbia in summer, *Continental Shelf Research*, *25*(14), 1631–1656, doi:10.1016/j.csr.2005.04.010.

Hickey, B. A. MacFadyen, W. Cochlan, R. Kudela, K. Bruland, and C. Trick (2006). Evolution of chemical, biological, and physical water properties in the northern California Current in 2005: Remote or local wind forcing? *Geophysical Research Letters, 33*(22), 4-8, doi:10.1029/2006GL026782.

Hickey, B., and N. Banas (2008), Why is the Northern End of the California Current System So Productive?, *Oceanography*, *21*(4), 90–107, doi:10.5670/oceanog.2008.07.

Hickey, B. M. et al. (2010), River Influences on Shelf Ecosystems: Introduction and synthesis, *Journal of Geophysical Research*, *115*, 1–26, doi:10.1029/2009JC005452.

Ho, D. T., R. Wanninkhof, P. Schlosser, D. S. Ullman, D. Hebert, and K. F. Sullivan (2011), Toward a universal relationship between wind speed and gas exchange: Gas transfer velocities measured with $^3He/SF_6$ during the Southern Ocean Gas Exchange Experiment, *Journal of Geophysical Research*, *116*, C00F04, doi:10.1029/2010JC006854.

Huyer, A. (1983), Coastal upwelling in the California current system, *Progress in Oceanography*, *12*(3), 259–284, doi:10.1016/0079-6611(83)90010-1.

Huyer, A., P. A. Wheeler, P. T. Strub, R. L. Smith, R. Letelier, and P. M. Kosro (2007), The Newport line off Oregon – Studies in the North East Pacific, *Progress In Oceanography*, *75*(2), 126–160, doi:10.1016/j.pocean.2007.08.003.

IPCC, 2007: Climate Change 2007: The Physical Science Basis. Contribution of Working Group I to the Fourth Assessment Report of the Intergovernmental Panel on Climate Change [Solomon, S., D. Qin, M. Manning, Z. Chen, M. Marquis, K.B. Averyt, M.Tignor and H.L. Miller (eds.)]. Cambridge University Press, Cambridge, United Kingdom and New York, NY, USA.

Jiang, L. Q., W-J. Cai, R.A. Feely, Y. Wang, X. Guo, D.K. Gledhill, X. Hu, F. Arzayus, F. Chen, J. Hartmann, and L. Zhang (2010), Carbonate mineral saturation states along the US East Coast, *Limnology and Oceanography, 55*(6), 2424–2432, doi:10.4319/ lo.2010.55.6.2424.

Juranek, L. W., R.A. Feely,W. T. Peterson, S.R.Alin, B.Hales, C. L. Sabine, and J. Peterson (2009), A novel method for determination of aragonite saturation state on the continental

shelf of central Oregon using multi- parameter relationships with hydrographic data, *Geophysical Research Letters, 36*, L24601, doi:10.1029/2009GL040778.

Kara, A.B., P.A. Rochford, and H.E. Hurlburt (2000), An optimal definition for ocean mixed layer depth, *Journal of Geophysical Research, 105*(C7), 16803-16821, doi: 10.1029/2000JC900072.

Keeling, C. D. (1960), The concentration and isotopic abundances of carbon dioxide in the atmosphere, *Tellus*, *12*(2), 200–203, doi:10.1111/j.2153-3490.1960.tb01300.x.

Kirincich, A. R., and J. A. Barth (2009), Alongshelf Variability of Inner-Shelf Circulation along the Central Oregon Coast during Summer, *Journal of Physical Oceanography*, *39*(6), 1380–1398, doi:10.1175/2008JPO3760.1.

Kleypas, J. A., and K. K. Yates (2009), Coral Reefs and Ocean Acidification, *Oceanography*, *22*(4), 108–117.

Kroeker, K. J., R. L. Kordas, R. N. Crim, and G. G. Singh (2010), Meta-analysis reveals negative yet variable effects of ocean acidification on marine organisms., *Ecology letters*, *13*(11), 1419–34, doi:10.1111/j.1461-0248.2010.01518.x.

Kudela, R. M., N. Garfield, and K. W. Bruland (2006), Bio-optical signatures and biogeochemistry from intense upwelling and relaxation in coastal California, *Deep Sea Research Part II: Topical Studies in Oceanography*, *53*(25-26), 2999–3022, doi:10.1016/j.dsr2.2006.07.010.

Kundu, P. K., and J. S. Allen (1976), Some three-dimensional characteristics of low-frequency current fluctuations near the Oregon Coast, *Journal of Physical Oceanography*, *6*, 181–199, doi:10.1175/1520-0485(1976)006.

Kurihara, H., and Y. Shirayama (2004), Effects of increased atmospheric CO_2 on sea urchin early development, *Marine Ecology Progress Series*, *274*, 161–169, doi:10.3354/meps274161.

Lefevre, N., J.P. Ciabrini, G. Michard, B. Brient, M. DuChaffaut, and L. Merlivat (1993), A new optical sensor of pCO_2 measurements in seawater, *Marine Chemistry, 42*(3-4), 189-188, doi:10.1016/0304-4203(93)90011-C.

Lee, Z, E. (2006), *International Ocean Colour Coordinating Group (IOCCG) Report 5.*

Liu, X., M. C. Patsavas, and R. H. Byrne (2011), Purification and characterization of meta-cresol purple for spectrophotometric seawater pH measurements., *Environmental science & technology*, *45*(11), 4862–8, doi:10.1021/es200665d.

MacFadyen, a., B. M. Hickey, and W. P. Cochlan (2008), Influences of the Juan de Fuca Eddy on circulation, nutrients, and phytoplankton production in the northern California Current System, *Journal of Geophysical Research*, *113*(C8), C08008, doi:10.1029/2007JC004412.

Mackas, D.L., Peterson, W.T., Ohman, M.D., Lavaniegos, B.E., 2006. Zooplankton anomalies in the California Current system before and and during the warm ocean conditions of 2005. *Geophysical Research Letters, 33,* doi:10.1029/2006GL027930.

Mamayev, O. I. (1975), Temperature-salinity analysis of the world ocean waters, Elsevier Scientific: Amsterdam-Oxford-New York, 374 pp.

Martz, T. R., J. J. Carr, C. R. French, and M. D. DeGrandpre (2003), A submersible autonomous sensor for spectrophotometric pH measurements of natural waters., *Analytical chemistry*, *75*(8), 1844–50.

Martz, T. R., J. G. Connery, and K. S. Johnson (2010), Testing the Honeywell Durafet for seawater pH applications, *Limnology and Oceanography: Methods*, *8*, 172–184, doi:10.4319/lom.2010.8.172.

Mass, C., A. Skalenakis, and M. Warner (2011), Extreme precipitation over the West Coast of North America: is there atTrend?, *Journal of Hydrometeorology*, *12*(2), 310–318, doi:10.1175/2010JHM1341.1.

McGregor, H. V, M. Dima, H. W. Fischer, and S. Mulitza (2007), Rapid 20th-century increase in coastal upwelling off northwest Africa., *Science (New York, N.Y.)*, *315*(5812), 637–9, doi:10.1126/science.1134839.

Mehrbach, C., C. H. Culberson, J. E. Hawley, and R. M. Pytkowicz (1973), Measurement of the apparent dissociation constants of carbonic acid in seawater at atmospheric pressure, *Limnology and Oceanography 18*, 897-907.

Midorikawa, T., H. Y. Inoue, M. Ishii, D. Sasano, N. Kosugi, G. Hashida, S. Nakaoka, and T. Suzuki (2012), Decreasing pH trend estimated from 35-year time series of carbonate parameters in the Pacific sector of the Southern Ocean in summer, *Deep Sea Research Part I: Oceanographic Research Papers*, *61*, 131–139, doi:10.1016/j.dsr.2011.12.003.

Miller, A.W., A.C. Reynolds, C. Sobrino, and G.F. Riedel. 2009. Shellfish face uncertain future in high CO_2 world: Influence of acidification on oyster larvae calcification and growth in estuaries. *PLoS ON, 4*(5):e5661.

Millero, F.J. (1995), Thermodynamics of the carbon dioxide system in the oceans, *Geochimica et Cosmochimica Acta, 59*(4), 661-677.

Millero, F.J. (2007), The marine inorganic carbon cycle, *Chemical Reviews, 107*(2), 308-341, doi: 10.1021/cr0503557.

Millero, F. J., K. Lee, and M. Roche (1998), Distribution of alkalinity in the surface waters of the major oceans, *Marine Chemistry*, *60*(1-2), 111–130, doi:10.1016/S0304-4203(97)00084-4.

Morse, J. W., A. J. Andersson, and F. T. Mackenzie (2006), Initial responses of carbonate-rich shelf sediments to rising atmospheric pCO_2 and "ocean acidification": Role of high Mg-calcites, *Geochimica et Cosmochimica Acta*, *70*(23), 5814–5830, doi:10.1016/j.gca.2006.08.017.

Mucci, A. (1983) The solubility of calcite and aragonite in seawater at various salinities, temperatures, and one atmosphere total pressure, *American Journal of Science, 283*, 781-799.

Mosley, L.M., S.L.G. Husheer, and K.A. Hunter (2004), Spectrophotometric pH measurement in estuaries using thymol blue and m-cresol purple, *Marine Chemistry, 91*(1-4), 175-186, doi: 10.1016/j.marchem.2004.06.00.

Nakicenovic, N. et al. (2000), *Special Report on Emissions Scenarios: A Special Report of Working Group III of the Intergovernmental Panel on Climate Change*, Cambridge, United Kingdom.

O'Donnell, M., A. Todgham, M. Sewell, L. Hammond, K. Ruggiero, N. Fangue, M. Zippay, and G. Hofmann (2010), Ocean acidification alters skeletogenesis and gene expression in larval sea urchins, *Marine Ecology Progress Series*, *398*, 157–171, doi:10.3354/meps08346.

Oke, P. R., J. S. Allen, R. N. Miller, and G. D. Egbert (2002), A Modeling Study of the Three-Dimensional Continental Shelf Circulation off Oregon . Part II : Dynamical Analysis, *Journal of Physical Oceanography*, *32*, 1383–1403, doi:10.1175/1520-0485(2002)032.

Orr, J. C., et al. (2005), Anthropogenic ocean acidification over the twenty-first century and its impact on calcifying organisms., *Nature*, *437*(7059), 681–6, doi:10.1038/nature04095.

Pansch, C., A. Nasroiahi, Y. S. Appelhans, and M. Wahl (2012), Impacts of ocean warming and acidification on the larval development of the barnacle Amphibalanus improvisus, *Journal of Experimental Marine Biology and Ecology*, *420*, 48–55, doi:10.1016/jembe.2012.03.023.

Papastephanou, K. M., S. M. Bollens, and A. M. Slaughter (2006), Cross-shelf distribution of copepods and the role of event-scale winds in a northern California upwelling zone, *Deep Sea Research Part II: Topical Studies in Oceanography*, *53*(25-26), 3078–3098, doi:10.1016/j.dsr2.2006.07.014.

Park, P. K. (1969), Oceanic CO2 system: An evaluation of ten methods of investigation, *Limnology and Oceanography*, *14*(2), 179–186.

Pauly, D., and V. Christensen (1995), Primary production required to sustain global fisheries, *Nature*, *374*(6519), 255–257, doi:10.1038/374255a0.

Pierrot, D., E. Lewis, and D.R. Wallace (2006), MS Excel Program Developed for CO_2 System Calculations. ORNL/CDIAC-105a. Carbon Dioxide Information Analysis Center, Oak Ridge National Laboratory, U.S. Department of Energy, Oak Ridge, Tennessee. doi:10.3334/CDIAC/otg.CO2SYS_XLS_CDIAC105a.

Platt, T., C. L. Gallegos, and W. G. Harrison (1980), Photoinhibition of photosynthesis in natural assemblages of marine phytoplankton, *Journal of Marine Research*, *38*, 687-701.

Pytkowicz, R. M. (1973), Calcium carbonate retention in supersaturated seawater, *American Journal of Science*, *273*(6), 515–522, doi:10.2475/ajs.273.6.515.

Ramp, S. R., and F. L. Bahr (2008), Seasonal evolution of the upwelling process south of Cape Blanco, *Journal of Physical Oceanography*, *38*(1), 3–28, doi:10.1175/2007JPO3345.1.

Raven, J. A., and P. G. Falkowski (1999), Oceanic sinks for atmospheric CO_2 , *Plant, Cell and Environment*, *22*(6), 741–755, doi:10.1046/j.1365-3040.1999.00419.x.

Ries, J. B., a. L. Cohen, and D. C. McCorkle (2009), Marine calcifiers exhibit mixed responses to CO_2-induced ocean acidification, *Geology*, *37*(12), 1131–1134, doi:10.1130/G30210A.1.

Risien, C.M., P.L. Mazzini, and J.A. Barth, Observations of anomalous near-surface low-salinity pulses off the Central Oregon Coast. Presented at 2012 Ocean Sciences Meeting, Salt Lake City, Utah, February 21, 2012. 10465.

Sabine, C. L., R.A. Feely, N. Gruber, R.M. Key, K. Lee, J.L. Bullister, R. Wanninkhof, C.S. Wong, D.W.R. Wallace, B. Tilbrook, F.J. Millero, T.-H. Peng, A. Kozyr, T. Ono. and A.F. Rios (2004), The oceanic sink for anthropogenic CO_2, *Science*, *305*(5682), 367–71, doi:10.1126/science.1097403.

Salisbury, J. E., D. Vandemark, C. W. Hunt, J. W. Campbell, W. R. McGillis, and W. H. McDowell (2008), Seasonal observations of surface waters in two Gulf of Maine estuary-plume systems: Relationships between watershed attributes, optical measurements and surface pCO2, *Estuarine, Coastal and Shelf Science*, *77*(2), 245–252, doi:10.1016/j.ecss.2007.09.033.

Schar, D., M. Atkinson, T. Johengen, A. Pinchuk, H. Purcell, C. Robertson, and G. J. Smith (2009), *Performance Demonstration Statement PMEL MAPCO_2 / Battelle Seaology pCO_2.*

SciFinder, version 2013. Substance Identifier: Columbus, OH, 2013; CAS 76-61-9 (accessed August 23, 2013.

Schwing, F. B., and R. Mendelssohn (1997), Increased coastal upwelling in the California Current System, *Journal of Geophysical Research*, *102*(C2), 3421–3438, doi:10.1029/96JC03591.

Schwing, F. B., N. A. Bond, S. J. Bograd, T. Mitchell, M. A. Alexander, and N. Mantua (2006), Delayed coastal upwelling along the U.S. West Coast in 2005: A historical perspective, *Geophysical Research Letters*, *33*(22), L22S01, doi:10.1029/2006GL026911.

Seidel, M.P. (2006), *A sensor for in situ spectrophotometric measurements of seawater pH*, (Doctoral Dissertation), The University of Montana, Missoulat, MT.

Seidel, M. P., M. D. DeGrandpre, and A. G. Dickson (2008), A sensor for in situ indicator-based measurements of seawater pH, *Marine Chemistry*, *109*(1-2), 18–28, doi:10.1016/j.marchem.2007.11.013.

Sherwood, S. (2011), Science controversies past and present feature, *Physics Today*, *64*(10), 39–44, doi:10.1063/PT.3.1295.

Shirayama, Y., and H. Thornton (2005), Effect of increased atmospheric CO_2 on shallow water marine benthos, *Journal of Geophysical Research*, *110*(C9), C09S08, doi:10.1029/2004JC002618.

Takahashi, T., T. T. Takahashi, S. C. Sutherland, and R. G. Williams (1995), An assessment of the role of the North Atlantic as a CO2 Sink [and discussion], *Philosophic Transactions of the Royal Society B: Biological Sciences*, *348*(1324), 143–152.

Takahashi, T. et al. (2002), Global sea–air CO_2 flux based on climatological surface ocean pCO_2, and seasonal biological and temperature effects, *Deep Sea Research Part II: Topical Studies in Oceanography*, *49*(9-10), 1601–1622, doi:10.1016/S0967-0645(02)00003-6.

Takahashi, T. et al. (2009), Climatological mean and decadal change in surface ocean pCO2, and net sea–air CO2 flux over the global oceans, *Deep Sea Research Part II: Topical Studies in Oceanography*, *56*(8-10), 554–577, doi:10.1016/j.dsr2.2008.12.009.

Thomsen J., and F. Melzner (2010) Moderate seawater acidification does not elicit long-term metabolic depression in the blue mussel *Mytilus edulis, Marine Biology, 157,* 2667–2676.

Thomson, R. E., and M. V. Krassovski (2010), Poleward reach of the California Undercurrent extension, *Journal of Geophysical Research*, *115*(C9), 1–9, doi:10.1029/2010JC006280.

Torres, R., D. Turner, J. Ruttlant, M. Sobarzo, T. Antezana, and H.E. Gonzalez (2002), CO_2 outgassing off central Chile (31-30°S) and northern Chile (24-23°S) during austral summer 1997: the effect of wind intensity on the upwelling and ventilation of CO_2-rich waters, *Deap -Sea Research Part I, 49,* 1413-1429, doi: 10.1016/S0967-0637(02)00034-1.

Turi, G., Z. Lachkar, and N. Gruber (2013), Spatiotemporal variability and drivers of pCO_2 and air-sea CO_2 fluxes in the California Current System, an eddy-resolving modeling study, *Biogeosciences, 10*(8), 14043-14091, doi: 10.5194/bgd-10-14043-2013.

Venegas, R. M., P. T. Strub, E. Beier, R. Letelier, A. C. Thomas, T. Cowles, C. James, L. Soto-Mardones, and C. Cabrera (2008), Satellite-derived variability in chlorophyll, wind stress, sea surface height, and temperature in the northern California Current System, *Journal of Geophysical Research*, *113*(C3), 1–18, doi:10.1029/2007JC004481.

Volk, T., and M. I. Hoffert (1985), Ocean carbon pumps: Analysis of relative strengths and efficiencies in ocean-driven atmospheric CO2 changes, in *The Carbon Cycle and Atmospheric CO2: Natural Variations Archean to Present*, edited by E. T. Sundquist and W. S. Broecker, pp. 99–110, AGU, Washington, D.C.

Waldbusser, G.G., R.A. Steenson, and M.A. Green (2011), Oyster shell dissolution rates in estuarine waters: effects of pH and shell legacy, *Journal of Shellfish Research, 30*(3), 665-669, doi: 10.2983/035.030.0308.

Weart, S. R. (2008), *The Discovery of Global Warming: Revised and Expanded Edition*, 2nd ed., Harvard University Press, Boston, MA.

Wood, H.L., J.I. Spicer, and S. Widdicombe (2008), Ocean acidification may increase calcificatio rates, but at a cost, *Proceedings of the Royal Society: Biological sciences, 275*(1644), 1767-1773, doi: 10.1098/rspb.2008.0343.

Yao, W., X. Liu, and R.H. Byrne (2007), Impurities in indicators used for spectrophotometric seawater pH measurements: assesment and remedies, *Marine Chemistry, 107*(2), 167-172, doi: 10.1016/j.marchem.2007.06.012.

Zhang, H., and R. H. Byrne (1996), Spectrophotometric pH measurements of surface seawater at in-situ conditions : absorbance and protonation behavior of thymol blue, *Marine Chemistry, 52*(95), 17-25.

Zondervan, I., R. E. Zeebe, B. Rost, and U. Riebesell (2001), Decreasing marine biogenic calcification: A negative feedback on rising atmospheric pCO_2, *Global Biogeochemical Cycles*, *15*(2), 507–516.